ISSN 2312-4334

MINISTRY OF EDUCATION AND SCIENCE OF UKRAINE

East European Journal of Physics

No 3. 2019

2019

East European Journal of Physics

EEJP is an international peer-reviewed journal devoted to experimental and theoretical research on the nuclear physics, cosmic rays and particles, high-energy physics, solid state physics, plasma physics, physics of charged particle beams, plasma electronics, radiation materials science, physics of thin films, condensed matter physics, functional materials and coatings, medical physics and physical technologies in an interdisciplinary context.
Published quarterly in hard copy and online by V.N. Karazin Kharkiv National University Publishing.
ISSN 2312-4334 (Print), ISSN 2312-4539 (Online)

The editorial policy is to maintain the quality of published papers at the highest level by strict peer review.
Approved for publication by the Academic Council of the V.N. Karazin Kharkiv National University (September 30, 2019, Protocol No. 9).
EEJP registered by the order of Ministry of Education and Science of Ukraine № 747 of 13.07.2015, and included in the list of scientific specialized editions of Ukraine, which can be published results of dissertations for the Ph.D. and Dr.Sci. degree in physical and mathematical sciences.

Editorial office
Department of Physics and Technologies, V.N. Karazin Kharkiv National University
Kurchatov av., 31, office 402, Kharkiv, 61108, Ukraine
Tel: +38-057-335-18-33,
E-mail: eejp@karazin.ua,
Web-pages: http://periodicals.karazin.ua/eejp (Open Journal System)
Certificate of State registration No.20644-10464P, 21.02.2014

East European Journal of Physics

No 3 2019

ORIGINAL PAPERS

HISTORY OF SCIENCE

EAST EUROPEAN JOURNAL OF PHYSICS
East Eur. J. Phys. **3**. 4-9 (2019) DOI:10.26565/2312-4334-2019-3-01

PACS: 52.25.Os, 52.20.Dq, 52.55.Fa

LONG-LIVED BANANA ORBIT FORMATION OF SUPRATHERMAL ELECTRONS DURING MHD SPIKES IN RUNAWAY TOKAMAK DISCHARGES

Igor Pankratov[1,2], Volodymyr Bochko[1]
[1]*Department of Physics and Technology, V.N. Karazin Kharkiv National University*
Svobody Sq.4, 61022 Kharkiv, Ukraine
[2]*Institute of Plasma Physics, NSC "Kharkiv Institute of Physics and Technology"*
Akademichna Str.1, 61108 Kharkiv, Ukraine
E-mail: pankratov@kipt.kharkov.ua
Received May 29, 2019; revised August 7, 2019; accepted August 21, 2019

The secondary runaway electrons generation is the process in which already existing high energy runaway electrons knock out thermal plasma electrons directly into the runaway region by close Coulomb collisions. Such knocked-on electrons are immediately accelerated to ultrarelativistic velocities, since in the runaway region the toroidal electric field force overcomes the collisional friction force with thermal plasma particles. The avalanche of runaway electrons with mega-electron-volt energy emerges, hit of which with the construction elements of large-scale tokamaks and future international tokamak ITER can lead to catastrophic consequences. Due to its importance, this phenomenon is being actively studied both theoretically and experimentally in leading thermonuclear fusion centers. It is known that during secondary generation, the value of the transversal component of knocked-on electrons momentum with respect to the confining magnetic field may be significantly higher than the longitudinal one: $p_\perp >> p_\parallel$. Thus, conditions for knocked-on electron trapping in a non-uniform tokamak magnetic field occur (banana orbits). Such electrons can no longer be accelerated by the inducted toroidal electric field to high energies, avalanche formation is partially suppressed. The question is how long this population of knocked-on and trapped electrons exists. In the presented paper, it is shown the additional possibility of formation and existence of such long-lived banana orbits of suprathermal electrons under conditions of plasma MHD activity when MHD instability spikes induced the strong burst of the toroidal electric field that results in the abrupt growth in these knocked-on and trapped electrons. This phenomenon is considered for the recent low-density EAST (Institute of Plasma Physics, Chinese Academy of Sciences, Hefei, China) tokamak quasistationary runaway discharges. Long-lived trapped electrons ($p_\perp >> p_\parallel$) also have an influence on the intensity of ECE emission. The considered phenomenon is important for correct interpretation of the runaway experiments on present-day tokamaks.
KEYWORDS: tokamak, runaway electrons, suprathermal electrons, banana orbits, electron cyclotron emission (ECE)

The runaway electrons during major disruptions can cause serious damage to plasma-facing-component surfaces in large tokamaks like ITER [1, 2]. The strong electric fields induced during the tokamak disruptions can generate many runaways (REs). The energy of these REs can reach as high as tens of MeV. Due to close Coulomb collisions of these REs with the electrons of the background plasma, the effect of avalanche occurs (secondary runaway generation) [3].

The knocked-on secondary electrons may have significant transverse momentum, $p_\perp >> p_\parallel$ ($p_\parallel$ and $p_\perp$ are longitudinal and transversal components of momentum with respect to the confining magnetic field, correspondingly). In tokamaks, electrons trapped in a non-uniform tokamak magnetic field may appear in this case [4]. As the result of close collisions, the formation of long-lived trapped suprathermal electron population under conditions of working gas (deuterium) puffing during runaway tokamak discharges (DIII-D runaway experiments under quiescent conditions [5]) was investigated in [6, 7].

In the present paper, it is shown the additional possibility of long-lived banana orbit formation of suprathermal electrons during MHD spikes in runaway tokamak discharges (EAST experiments [8-10]). This is the objective of this investigation.

RUNAWAY EAST DISCHARGE WITH THE STEPWISE JUMP INCREASES OF THE NON-THERMAL ECE SIGNAL DURING MHD BURSTS

During EAST experiments with runaway electrons [8-10], peculiar events have been investigated: rapid changes in the synchrotron spot shape and its intensity that coincided with step-like jumps in the electron cyclotron emission (ECE) signal (cyclotron radiation of suprathermal electrons) and the MHD (m/n=2/1) Mirnov signal spikes (m and n are the poloidal and toroidal mode numbers, respectively). These phenomena were initially observed in TEXTOR (Tokamak Experiment for Technology Oriented Research), where these events only occurred in the current decay phase or in discharges with thin stable runaway beams at the q = 1 drift surface [11] (q is the safety factor).

The runaway ohmic discharge #28957 in EAST was performed in the limiter configuration with the toroidal magnetic field $B_0 = 2$ T, the plasma current $I_p = 250$ kA, the inductive equilibrium electric field $E_\parallel = V_{loop}/2\pi R_0 = E_0 \approx 0.1$ V/m, the central line-averaged density $<n_e> = 2.2\ 10^{19}$ m^{-3}, the plasma major radius $R_0 = 1.86$ m and the minor radius $a = 0.45$ m [8-10]. At the plasma center, the electron temperature $T_e \approx 0.55$ keV was obtained using a soft x-ray pulse height analysis (PHA) system during the plasma current flat-top phase (duration of impulse was 5 s). MHD modes m/n=1/1 (the soft x-ray signal) and m/n=2/1 (the Mirnov coil signals) existed in the plasma. Runaway electrons were created by the ohmic coil during the start-up phase of the discharge, the runaway

current was significant. The runaway electrons were located near the $q = 2$ rational magnetic surface at $r \approx$ (20-30) cm (ring-like runaway electron beam).

In shot #28957 three types of events were observed with the stepwise jump increases of the non-thermal ECE signal that are described and discussed in details in Refs. [8-10]. Here, we give only a short summary of these papers results:

1. The MHD (m/n=2/1) small amplitude spikes (type I events, small non-thermal ECE jumps) emerged approximately every 0.02 s and coincided with sawtooth m/n=1/1 peaks.

2. Huge MHD spikes (type II events) emerged approximately every 0.5 s.

3. Larger amplitude MHD (m/n=2/1) spikes (type III events) were observed approximately every 0.3 s after each huge MHD spike (type II events).

In cases II-III types events the MHD (m/n=2/1) spikes of the non-thermal ECE jumps were not small. In these cases, MHD spikes were not correlated with the m/n=1/1 sawtooth oscillations peaks.

These ECE jumps were visible in the ECE channels, which should receive the second harmonic X-mode emission of the thermal electrons from the tokamak low-field-side (lfs).

Due to the local runaway generation processes, local changes in the plasma current density profile should occur (around the $q = 2$ rational magnetic surface, where the runaway electrons are located). In [10] it has been shown that these local changes in the current density profile are a possible trigger for enhancement of magnetohydrodynamic (MHD) tearing mode activity and fast changes in runaway beam behavior. For these shots, the MHD m/n=2/1 bursts were resulted from tearing mode instability with induced bursts of the strong electric field during magnetic reconnections.

In low-density plasma ($n_e \sim 10^{19}$ m^{-3}), the occurrence of runaway electrons is connected to their continuous acceleration by the tokamak toroidal equilibrium electric field $E_\parallel = E_0 \approx 0.1$ V/m. The runaway energy $E_{run} \approx 30$ MeV was deduced from a joint analysis of the synchrotron radiation spectra and the synchrotron radiation spot shape in EAST discharge #28957 [9]. This means that in EAST discharge #28957, the secondary runaway generation process should take place (runaway avalanche).

2D MOMENTUM-SPACE ANALYSIS OF SUPRATHERMAL ELECTRON GENERATION

The generation of both high-energy runaway and suprathermal electrons should be enhanced abruptly during these MHD spikes. Because of the fast changes in the magnetic flux (squeezing and reconnection of the magnetic field lines) the bursts of induced electric fields, $E_\parallel(t)$, occurred [12]. The value of $E_\parallel(t)$ may reach values of an order of ten V/m. During these bursts of the induced electric field $E_\parallel(t)$, the avalanche process was enhanced with corresponding avalanching time [13]

$$t_{av} \approx \sqrt{12} m_e c L (2 + Z_{eff}) / 9 e E_\parallel(t) . \quad (1)$$

The electron runaway region increased very fast because of the value of parameter (this key parameter determines boundaries of runaway region)

$$p_{cr}^2(E_\parallel(t)) = e^3 m_e n_e L / 4\pi\varepsilon_0^2 E_\parallel(t) \quad (2)$$

dropped during the burst of $E_\parallel(t)$ (Fig. 1), e, m_e are the charge and rest mass of electron, respectively, L is the Coulomb logarithm.

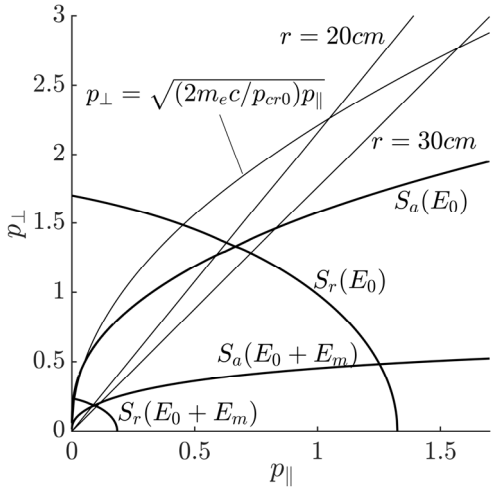

Fig. 1. The evolution of runaway region in 2D plane ($p_\parallel$, $p_\perp$) during MHD burst.

The abrupt growth in the suprathermal electron population occurred during these bursts of $E_\parallel$. In [10, 14] conclusion was made that the step-like non-thermal ECE jumps may be explained by the abrupt growth in the

suprathermal electron generation (number of runaways) during MHD m/n=2/1 spikes. In Fig. 1 the evolution of runaway region in 2D plane ($p_\parallel$, $p_\perp$) is shown. Normalized variables are used:

$$E_\parallel(t) \to E_\parallel(t)/E_0,\ \ p_{\parallel,\perp} \to p_{\parallel,\perp}/p_{cr}(E_0),\ t \to t/\tau_{br}\,. \tag{3}$$

Here $S_r(E_0, E_0+E_m)$ and $S_a(E_0, E_0+E_m)$ are separatrixes (compare with [13, 15]) for plasma parameters at E_0 and E_0+E_m, where E_m is the maximum amplitude of the toroidal electric field during MHD spike, $\tau_{br} \sim 1$ms is the time during which the value of electric field changes from E_0 to E_0+E_m.This analysis is based on the equations (compare with [13, 15]):

$$\frac{dp_\parallel}{dt} = \tau_{br}\frac{eE_\parallel(0)}{p_{cr0}}\left(E_\parallel(t) - (Z_{eff}+2)\frac{p_\parallel}{\left(p_\parallel^2+p_\perp^2\right)^{3/2}}\right), \tag{4}$$

$$\frac{dp_\perp^2}{dt} = 2\tau_{br}\frac{eE_\parallel(0)}{p_{cr0}}\frac{1}{\sqrt{p_\parallel^2+p_\perp^2}}\left((Z_{eff}+2)\frac{p_\parallel^2}{p_\parallel^2+p_\perp^2} - 1\right). \tag{5}$$

The first term in expression (4) describes the test electron's acceleration by $E_\parallel(t)$, and the second one describes the frictional force due to collisions of this electron with thermal particles. The total momentum (kinetic energy) of the test electron also changes due to ***eEv*** term and collisions that leads to change of transversal component of momentum: expression (5). The runaway region lies just above the separatrix S_r. Electrons situated above S_r lie on trajectories aiming asymptotically outward along S_a and therefore run away. In Fig. 1 $E_0 = 0.1$ V/m, as example the value $E_m = 5$ V/m is used. Note, the value $E_m = 12$ V/m of the induced electric field was found during a series of minor disruptions in the T-10 tokamak [16].

Note that in accordance with the conservation laws of energy and momentum, the knocked-on electrons of secondary generation are arranged on elongated ellipses, the major axes of which are equal to the momentum of the incident mega-electron-volt electrons. Secondary runaway region in the phase space ($p_\parallel, p_\perp$) is filled by these ellipses. In case of EAST shot #28957 the ring-like runaway beam contained high energy electrons with energy more than 20 MeV and $p_\perp/p_\parallel \sim 0.15$ ($p_\parallel >> p_\perp$) [8, 9]. The bulk electrons knocked out in runaway region by these very high energy electrons are born near the parabola [4]:

$$p_\perp = \sqrt{(2m_e c/p_{cr0})p_\parallel}\,. \tag{6}$$

This curve (6) is shown in Fig. 1, the locus of the knocked-on electrons lies below this curve. The suprathermal electron population with $p_\perp > p_\parallel$ occurs. These electrons may be trapped in a non-uniform tokamak magnetic field ($\varepsilon = r/R_0$)

$$B(r,\theta) = \frac{B_0}{1-\varepsilon\cos\theta}, \tag{7}$$

if the inequality

$$p_\perp/p_\parallel > 1/\sqrt{2\varepsilon} \tag{8}$$

holds at poloidal angle $\theta = \pi$. In Fig. 1, straight lines

$$p_\perp/p_\parallel = 1/\sqrt{2\varepsilon} \tag{9}$$

are shown for the values of r = 20cm and r = 30cm. The entire range of locus of the knocked-on electrons in 2D plane ($p_\parallel$, $p_\perp$) lies above straight lines of Eq. (9). It is necessary to distinguish situation on the outer (lfs) and inner sides of the tokamak discharge. The trapped suprathermal electrons may appear in the lfs region, only.

In Fig. 2 narrow banana orbits of the trapped suprathermal electrons are shown for the radii r = 20cm and r = 30cm. Recall, the ring-like runaway electron beam were located near the q = 2 value at these r = (20-30) cm [8, 9].

The calculations were carried out on the base of the well-known equations of motion of a charged particle in nonuniform tokamak magnetic field (see, e.g. [17], $\omega_B = eB_0/m_e$):

$$\frac{dr}{dt} = \frac{v_\parallel^2 + 0.5v_\perp^2}{|\omega_B|R_0}\sin\theta\,, \tag{10}$$

$$r\frac{d\theta}{dt} = v_\parallel\frac{r}{qR_0(1-\varepsilon\cos\theta)} + \frac{v_\parallel^2+0.5v_\perp^2}{|\omega_B|R_0}\cos\theta\,. \tag{11}$$

More strong losses of these trapped electrons may occur from the plasma region where these electrons are located (outer part of discharge). It is even possible formation of supertrapped electrons (on the ripples of a toroidal magnetic field) which immediately escape from the plasma owing to toroidal drift.

For considered energy of suprathermal electrons, the time-scale for pitch-angle equilibration (isotropization process) is much shorter than the momentum evolution time-scale [18]. The time-scale during which banana orbits may exist is much shorter in comparison with the isotropization time τ_{coll}.
The pitch angle that corresponds to banana orbits existence, Eq. (8), was taken into account in the estimation of the value of $\tau_{effcoll}$

$$\tau_{effcoll} = \tau_{coll}\, 2\varepsilon / (1+2\varepsilon) \tag{12}$$

and well-known expression for τ_{coll} is used:

$$\tau_{coll}^{-1} = e^4 n_e m_e L / 4\pi\varepsilon_0^2 (p_\perp^2 + p_\parallel^2)^{3/2}\,. \tag{13}$$

Note that the value of ion effective charge Z_{eff} was not high in shot #28957.

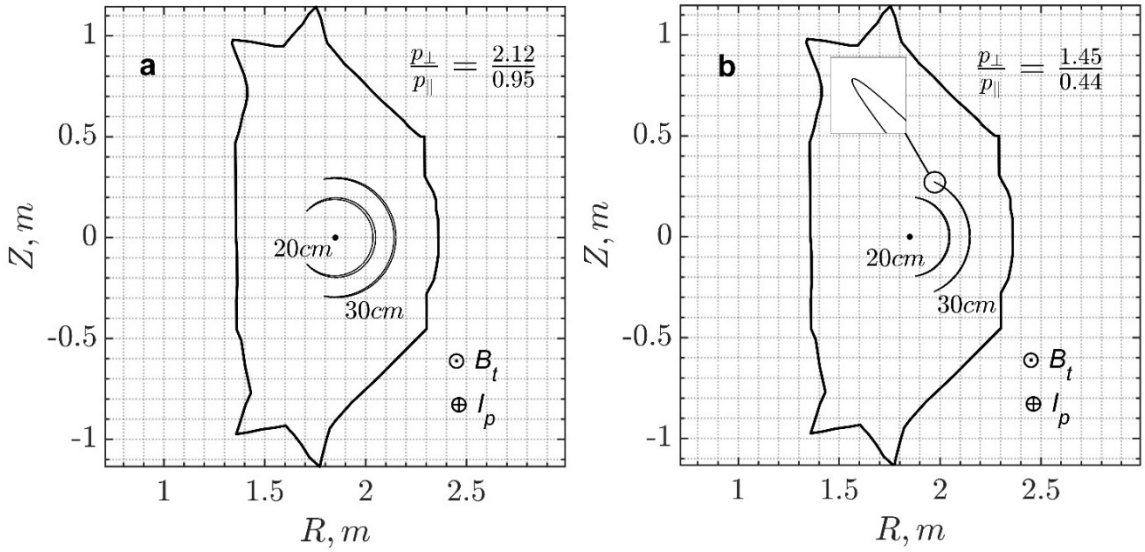

Fig. 2. Narrow banana orbits of suprathermal electrons
a) banana width (1.0-1.4) cm, energy ~ 230 keV; b) banana width (0.5-0.7) cm, energy ~ 100 keV. The values of $p_\perp$ and $p_\parallel$ corresponds to point at $\theta = \pi$. Directions of the toroidal magnetic field and plasma current are shown.

In Fig. 3, comparison of the bounce period of trapped suprathermal electrons ($T_b < 1\mu s$) with the effective collision time shows that $T_b << \tau_{effcoll}$. The long-lived banana orbits of suprathermal electrons have arisen. Ratio $\tau_{effcoll} / T_b$ can reach about five orders of magnitude. However, for $p_\parallel \lesssim 0.1$ the value of $\tau_{effcoll}$ decreases fast and $\tau_{effcoll} \rightarrow T_b$. In this region, the possibility of long-lived banana orbit formation is lower. The energy of suprathermal electrons corresponding to $p_\parallel = 0.1$ is about 20 keV. For calculation of τ_{coll} the values of $p_\perp$ were chosen close (but below) to the parabola of Eq. (6).

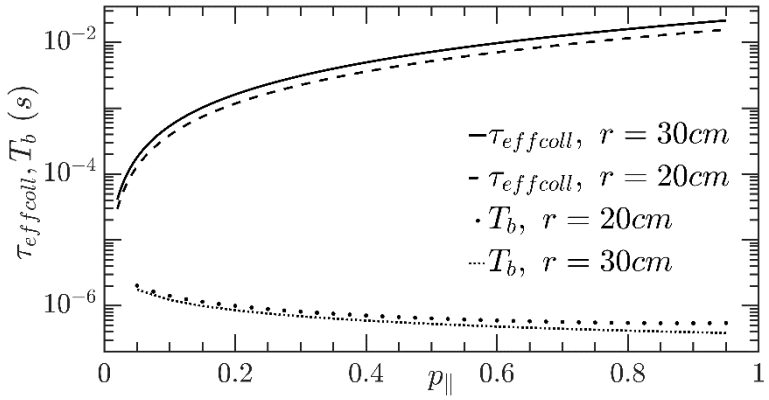

Fig. 3. The bounce period, T_b, of trapped suprathermal electrons and the effective collision time, $\tau_{effcoll}$.

In the EAST case, trapped knock-on secondary electrons were created far enough from the magnetic axis. These trapped electrons drift radially inwards due to the Ware pinch effect [19]

$$\frac{dr}{dt} = -\frac{E_\parallel(t)}{B_\theta}, \tag{14}$$

here B_θ is the poloidal magnetic field. They may be detrapped and run away (compare with [20]). Because of a very short time of the MHD spikes, the linear time dependence of changes of the bursting electric field $E_\parallel(t)$ was taken for integration of Eq. (14).

For analysis of the time Δt_W, required for a trapped electron to become passing (during the MHD burst), we obtain the next equation:

$$\left(\frac{\Delta t_W}{\tau_{br}}\right)^2 + 2\left(\frac{E_0}{E_m} + \frac{t_0}{\tau_{br}}\right)\left(\frac{\Delta t_W}{\tau_{br}}\right) - 2\frac{\Delta r_W}{\tau_{br} E_m / B_\theta} = 0\,, \tag{15}$$

where $\Delta r_W \sim (5 - 10)$ cm is the required radial displacement for detrapping process, $\tau_{br} \sim 1$ms, $t_0 = t_{br0} - t_{b0}$, here t_{br0} corresponds to the start of the burst, t_{b0} is the time when the banana was born, $B_\theta \approx 0.1$T. Even for the value of $E_m = 10$ V/m from Eq. (9) we get $\Delta t_W \sim 1$ms, that means $\Delta t_W >> T_b$.

CONCLUSIONS

The formation of long-lived knocked-on and trapped suprathermal electrons (long-lived banana orbits) in non-uniform magnetic field during MHD spikes in tokamak runaway discharges is shown, because of the effective collision frequency of these trapped electrons with background plasma particles is much smaller in comparison with the oscillation frequency of the bounce motion of trapped suprathermal electrons. The MHD spikes acted as a trigger for the enhancement of additional suprathermal electron generation (because of bursts of the toroidal electric field) during magnetic reconnections.

Such electrons can no longer be accelerated by the inducted toroidal electric field to high energies. The avalanching (secondary runaway generation) process may be suppressed in part.

The observed stepwise increases in the non-thermal electron cyclotron emission (ECE) signal coincided with the spikes of the MHD activity confirm abrupt growth of suprathermal electrons, and stepwise form of this signal may be explained by the existence of these long-lived knocked-on and trapped electrons population. The intensity of ECE signal must be strongly enhanced due to the existence of the long-lived suprathermal electron population with a high value of transversal momentum ($p_\perp > p_\parallel$).

The energy domain of these suprathermal electrons is shifted to more high values; in considered case, it is higher than 20 keV. The RE distribution function changes in this region of energies may be expected.

The considered phenomenon is important for correct interpretation of the runaway experiments.

ACKNOWLEDGEMENTS

We thank Dr. R.J. Zhou for detail discussions of EAST runaway experiments presented in the paper.

ORCID IDs

Igor Pankratov https://orcid.org/0000-0001-5876-4618, **Volodymyr Bochko** https://orcid.org/0000-0003-2109-968X

REFERENCES

[1] ITER Physics Basis, Chapter 3: MHD stability, operational limits and disruptions, Nucl. Fusion **39**, 2175 (1999), DOI: 10.1088/0029-5515/39/12/303.
[2] Progress in the ITER Physics Basis, Nucl. Fusion **47**, S128 (2007), DOI: 10.1088/0029-5515/47/6/S03.
[3] Yu. A. Sokolov, JETP Letters, **29**, 218 (1979).
[4] N.T. Besedin and I.M. Pankratov, Nucl. Fusion, **26**, 807 (1986), DOI 10.1088/0029-5515/26/6/009.
[5] C. Paz-Soldan, N.W. Eidietis, R. Granetz, E.M. Hollman, R.A. Moyer, J.C. Wesley, J. Zhang, M.E. Austin, N.A. Crocker, A. Wingen, and Y. Zhu, Phys. Plasmas, **21**, 022514 (2014), DOI: 10.1063/1.4866912.
[6] I.M. Pankratov and V.Y. Bochko, in: *Proceedings of the 45th EPS Conf. on Plasma Phys.* (Prague, 2018), P2.1057.
[7] I.M. Pankratov and V.Y. Bochko, Problems of Atomic Science and Technology, Series: Plasma Physics, **6**(118), 8-11 (2018), in: https://vant.kipt.kharkov.ua.
[8] R.J. Zhou, L.Q. Hu, E.Z. Li, M. Xu, G.Q. Zhong, L.Q. Xu, S.Y. Lin, J.Z. Zhang and the EAST Team, Plasma Phys. Control. Fusion, **55**, 055006 (2013), DOI: 10.1088/0741-3335/55/5/055006.
[9] R.J. Zhou, I.M. Pankratov, L.Q. Hu, M. Xu and J.H. Yang, Phys. Plasmas, **21**, 063302 (2014), DOI: 10.1063/1.4881469.
[10] I.M. Pankratov, R.J. Zhou and L Q. Hu, Phys. Plasmas, **22**, 072115 (2015), DOI: 10.1063/1.4927578.
[11] R. Jaspers, *Relativistic Runaway Electrons in Tokamak Plasmas, Ph.D. thesis* (Eindhoven University of Technology, The Netherlands, 1995), in: http://repository.tue.nl/431410.
[12] D. Biskamp, *Magnetic Reconnection in Plasmas* (Cambridge: Cambridge University Press, 2000).
[13] I.M. Pankratov, R. Jaspers, K.H. Finken and I. Entrop, in: *Proceedings of the 26th EPS Conf. on Contr. Fusion and Plasma Physics,* (Maastricht, 1999), p. 597.
[14] Yu. M. Marchuk and I.M. Pankratov, Problems of Atomic Science and Technology, Series: Plasma Physics, **1**(107) 6 (2017), in: https://vant.kipt.kharkov.ua.
[15] V. Fuchs, R.A. Cairns, C.N. Lashmore-Davies and M.M. Shoucri, Phys. Fluids, **29**, 2931 (1986), DOI: 10.1063/1.865493.
[16] P.V. Savrukhin and E.A. Shestakov, Nucl. Fusion, **55**, 043016 (2015), DOI: 10.1088/0029-5515/55/4/043016.
[17] Б.Б. Кадомцев, О.П. Погуце, *Турбулентные процессы в тороидальных системах*, в сб.: Вопросы теории плазмы, вып. 5, под ред. М.А. Леонтовича (М.: Атомиздат, 1967); B.B. Kadomtsev and O.P. Pogutse, *Turbulence in Toroidal Systems*, in: Reviews of Plasma Physics, **5**, edited by M.A. Leontovich (Boston: Springer, 1970).

[18] В.В. Параил, О.П. Погуце, *Ускоренные электроны в токамаке*, в сб.: Вопросы теории плазмы, вып. 11, под общ. ред. М. А. Леонтовича и Б.Б. Кадомцева (М.: Энергоиздат, 1982); V.V. Parail and O.P. Pogutse, *Runaway electrons in a tokamak*, in: Reviews of Plasma Physics, **11**, edited by M. A. Leontovich and B. B. Kadomtsev (New York: Consultant Bureau, 1986).
[19] A.A. Ware, Phys. Rev. Lett. **25**, 916 (1970), DOI: 10.1103/PhysRevLett.25.916.
[20] E. Nilsson, J. Decker, N.J. Fisch and Y. Peysson, J. Plasma Physics, **81**, 475810403 (2015), DOI: 10.1017/S0022377815000446.

ОБРАЗОВАНИЕ ДОЛГОЖИВУЩИХ БАНАНОВЫХ ОРБИТ НАДТЕПЛОВЫХ ЭЛЕКТРОНОВ ВО ВРЕМЯ ВСПЫШЕК МГД АКТИВНОСТИ В РАЗРЯДАХ ТОКАМАКА С УБЕГАЮЩИМИ ЭЛЕКТРОНАМИ

И.М. Панкратов[1,2], В.Ю. Бочко[1]
[1]Физико- технический факультет, Харьковский национальный университет имени В.Н. Каразина
пл. Свободы 4, 61022 Харьков, Украина
[2]Институт физики плазмы, ННЦ "Харьковский физико- технический институт"
ул. Академическая 1, 61108 Харьков, Украина

Вторичная генерация убегающих электронов – это процесс, при котором уже существующие высокоэнергетические убегающие электроны выбивают тепловые электроны плазмы непосредственно в область убегания в результате близких кулоновских столкновений. Такие выбитые электроны мгновенно ускоряются до ультрарелятивистских скоростей поскольку, в области убегания сила со стороны тороидального электрического поля значительно превосходит силу трения обусловленную кулоновскими столкновениями с тепловыми частицами плазмы. Возникает лавина мегаэлектронвольтных убегающих электронов, попадание которых на элементы конструкции современных больших токамаков и строящегося международного токамака-реактора ИТЭР может привести к катастрофическим последствиям. В силу своей актуальности, в настоящее время это явление широко изучается как теоретически, так и экспериментально в ведущих термоядерных центрах. Известно, что при вторичной генерации у выбитых электронов величина перпендикулярного импульса по отношению к магнитному полю токамака может существенно превышать продольную компоненту: $p_\perp >> p_\parallel$. Таким образом возникают условия захвата выбитых электронов неоднородным магнитным полем токамака (банановые орбиты). Захваченные электроны уже не могут ускорятся индукционным тороидальным электрическим полем до высоких энергий, лавинообразование убегающих электронов частично подавляется. Возникает вопрос, как долго такая популяция выбитых и захваченных надтепловых электронов существует. В данной работе показана дополнительная возможность для формирования и существования долгоживущих банановых орбит надтепловых электронов в условия МГД активности плазмы, когда во время вспышек МГД неустойчивости индуцируется сильное тороидальное электрическое поле что и приводит к резкому росту таких выбитых и захваченных электронов. Это явление рассмотрено для недавних экспериментов с убегающими электронами на токамаке EAST (Институт физики плазмы, Хефей, Академия наук Китая) в квазистационарных разрядах с низкой плотностью. Долгоживущие захваченные электроны ($p_\perp >> p_\parallel$) также оказывают влияние на интенсивность ECE излучения. Рассмотренное явление важно для правильной интерпретации экспериментов с убегающими электронами на современных токамаках.

КЛЮЧЕВЫЕ СЛОВА: токамак, убегающие электроны, надтепловые электроны, банановые орбиты, электронное циклотронное излучение (ECE)

ФОРМУВАННЯ ДОВГОЖИВУЧИХ БАНАНОВИХ ОРБІТ НАДТЕПЛОВИХ ЕЛЕКТРОНІВ ПІД ЧАС СПАЛАХІВ МГД АКТИВНОСТІ В РОЗРЯДАХ ТОКАМАКА З ЕЛЕКТРОНАМИ-ВТІКАЧАМИ

І.М. Панкратов[1,2], В.Ю. Бочко[1]
[1]Фізико- технічний факультет, Харківський національний університет імені В.Н. Каразіна
м. Свободи 4, 61022 Харків, Україна
[2]Інститут фізики плазми, ННЦ "Харківський фізико-технічний інститут"
вул. Академічна 1, 61108 Харків, Україна

Вторинна генерація електронів-втікачів – це процес, під час якого існуючі високоенергетичні втікаючі електрони вибивають теплові електрони плазми безпосередньо в область втікання в результаті близьких кулонівських зіткнень. Такі вибиті електрони миттєво прискорюються до ультрарелятивістських швидкостей, тому що в області втікання сила прискорення тороїдальним електричним полем значно перевищує силу тертя внаслідок кулонівських зіткнень з тепловими частинками плазми. Виникає лавина мегаелектронвольтних електронів-втікачів, потрапляння яких на конструкційні елементи сучасних великомасштабних токамаків і міжнародного споруджуваного токамака-реактора ITER може призвести до катастрофічних наслідків. Внаслідок своєї актуальності, у теперішній час дане явище активно досліджується як теоретично, так і експериментально у провідних термоядерних центрах. Відомо, що при вторинній генерації у вибитих електронів величина перпендикулярної компоненти імпульсу по відношенню до магнітного поля токамака може значно перевищувати повздовжню компоненту: $p_\perp >> p_\parallel$. Таким чином, виникають умови захоплення вибитих електронів неоднорідним магнітним полем токамака (бананові орбіти). Захоплені електрони більше не можуть прискорюватися індукованим електричним полем до високих енергій, лавиноподібне утворення електронів-втікачів частково пригнічується. Виникає питання, як довго популяція вибитих і захоплених надтеплових електронів існує. У даній роботі показана додаткова можливість для формування та існування довгоживучих банановых орбіт надтеплових електронів в умовах МГД активності плазми, коли під час спалахів МГД нестійкості індукується сильне тороїдальне електричне поле, що призводить до різкого зростання кількості таких вибитих і захоплених електронів. Дане явище розглянуто для нещодавніх експериментів з електронами-втікачами на токамаці EAST (Інститут фізики плазми, Хефей, Академія наук Китаю) в квазістаціонарних розрядах з низькою щільністю плазми. Довгоживучі захоплені електрони ($p_\perp >> p_\parallel$) також впливають на інтенсивність ECE випромінювання. Розглянуте явище важливе для правильної інтерпретації експериментів з електронами-втікачами на сучасних токамаках.

КЛЮЧОВІ СЛОВА: токамак, електрони-втікачі, надтеплові електрони, бананові орбіти, електронне циклотронне випромінювання (ECE)

EAST EUROPEAN JOURNAL OF PHYSICS
East Eur. J. Phys. **3**. 10-20 (2019) DOI:10.26565/2312-4334-2019-3-02

PACS: 12.38.Bx | 13.85.Qk

ANALYSIS OF ISOLATED PHOTONS IN PHOTOPRODUCTION IN PYTHIA

Andrii Iudin[1]*, Sergey Voronov[2]**
[1]*European Molecular Biology Laboratory, European Bioinformatics Institute*
Hingston, Cambridge, United Kingdom
[2]*National Technical University of Ukraine "Kyiv Polytechnic Institute named after Igor Sikorsky"*
St. Polytechnic, 6, Kiev, Ukraine
**E-mail: andyyudin@gmail.com, **E-mail: s.voronov@kpi.ua*
Received May 15, 2019; revised August 27, 2019; accepted September 26, 2019

Collision of particles at high energies at accelerators is the main source of data used to obtain deeper understanding of the fundamental interactions and the structure of the matter. Processes of isolated photon production have provided many tests of theoretical descriptions of the universe on scales smaller than the proton. This work is dedicated to the analysis of the large amount of collision data that has been accumulated at ZEUS in 2004-2007 period and new methods of processing isolated photons that have been proposed. The authors develop software algorithms that allow obtaining the signal of isolated photons from the data collected on the ZEUS detector at electron-proton collider HERA, calculating the differential cross sections, and comparing the measured data with PYTHIA Monte Carlo predictions. Taking into account the features of the ZEUS detector, the photon signal is separated from the background events and the number of isolated photons is calculated. Computational mathematical and numerical methods have been used to simulate the interaction of particles in the detector. Monte Carlo predictions for differential cross sections as functions of the pseudorapidity and transverse energy of the photon η^{γ}, E_T^{γ} and the jet η^{jet}, E_T^{jet}, and the fraction of the photon momentum x_{γ}^{meas} carried by the interacting parton have been calculated and compared with the experimental data. The results of the study are compared with the previous studies and show for the first time that all isolated photon HERA measurements are consistent with each other. New results show improved uncertainties. The formation of isolated inclusive photons and photons with the accompanying jet was measured in photoproduction with ZEUS detector at HERA collider using the integrated luminosity of 374 ± 7 pb^{-1}. For the first time, more complex Monte-Carlo simulation models of isolated photons for ZEUS detector were generated and applied, and the description of the photon signal was improved. It has been found that PYTHIA describes the shape of the cross section as a function of η^{γ} well enough, but does not fully reproduce the shape of E_T^{γ}, E_T^{jet}, and the middle region of x_{γ}^{meas}, while η^{jet} is described not very well. The reason for this discrepancy can be the lack of corrections of higher orders in the predictions for cross sections of direct photons. Scaling of the cross sections obtained with PYTHIA improves the description of E_T^{γ} and η^{γ}. The unsatisfactory description of η^{jet} indicates that further studies are required.
KEYWORDS: isolated photons, photoproduction, jet, Monte Carlo, PYTHIA, the electron-proton collision

Recently, high-energy particle collisions at accelerators have been the main source of experimental data used to gain a deeper understanding of the properties of fundamental interactions and to reveal the structure of matter. There are many different facilities for conducting such studies. Among them are ring and linear accelerators. Some experiments study the frontal collision of particles (colliders), but there are some that consider the collision of particles with a fixed target. In particular, HERA electron-proton ring collider (Hadron-Elektron-Ringanlage) is a great place to test many aspects of quantum chromodynamics (QCD), a fairly successful field theory describing interactions between fundamental components. Protons were accelerated to an energy of 920 GeV and electrons (positrons) to 27.5 GeV, corresponding to the centre of mass energy of 318 GeV. This paper is devoted to the study of data collected during the ZEUS experiment at the HERA collider.

The results of the fundamental interaction between subatomic particles that occur over a very short period of time in a well-localized region of space (so-called events) can be classified by measuring the particles that appear in the final state. One such event category is isolated photon events [1]. Some of Feynman diagrams for the formation of isolated photons are shown in Fig. 1. Circles indicate that the target has a structure, for example, a quark from a proton interacts, while the remnant of the proton is shown at a broad arrow. Similarly, for the photon.

In the kinematic region at HERA, the direct non-fragmentation process for the formation of isolated photons is mainly the QCD Compton process [2] (Fig. 1 (a)) $\gamma q^p \to \gamma q$, where q^p denotes the quark structure of the proton. The input photon interacts with the quark in the proton. In the final state observed, there is a photon with a large transverse momentum and a jet with a large transverse momentum. The contribution of this process to the cross section is of an order of $O(\alpha_{em}^2)$, where α_{em}^2 is the electromagnetic coupling constant.

Resolved non-fragmentation process has three processes (Fig. 1 (b)):

$$q^{\gamma} g^p \to \gamma q, \qquad q^{\gamma} \bar{q}^p \to \gamma g, \qquad g^{\gamma} q^p \to \gamma q,$$

where q^{γ} denotes the quark composition of the photon.

In principle, resolved isolated photon processes are able to show the distribution of not only quarks, but also gluons in the photon. However, the kinematic coverage available in this analysis has less sensitivity to the distribution of gluons in the photon. The magnitude of the hard scatter is of the order $O(\alpha_{em}^2 \alpha_s)$, where α_s is the constant of the strong coupling.

But after taking into account the factor $O(\alpha_{em}/\alpha_s)$ for the structure of the photon, the cross section is of the order of $O(\alpha_{em}^2)$, similarly as for the direct process.

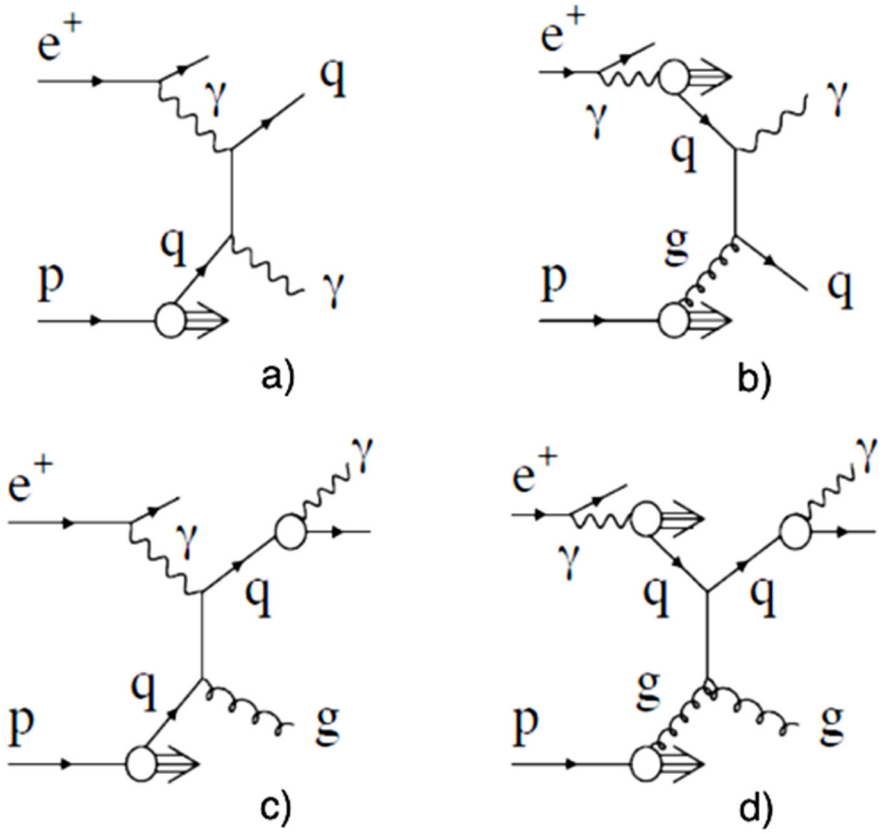

Fig. 1. Basic leading order QCD diagrams for isolated photons:
a) direct non-fragmentation; b) resolved non-fragmentation; c) direct fragmentation; d) resolved fragmentation

An isolated photon may also emerge from jet fragmentation. Thus, the diagrams that are contributing to the cross section are the same as for the two-jet process. Direct and resolved fragmentation processes: $\gamma q^p \to qg$, $q^\gamma g^p \to qg$ are shown in Fig. 1 (c, d). The next factor for photon fragmentation is given as $O(\alpha_{em}/\alpha_s)$. After taking into account the fragmentation factor and the photonic structure, the cross section is $O(\alpha_{em}^2)$ for direct and resolved fragmentation processes. Since cross section of fragmentation processes depends on fragmentation functions, its contribution decreases sensitivity to the measured distribution of partons in the photon. If such a photon takes almost all of the energy of the initial quark, then the event may be experimentally similar to that of the non-fragmentation process. After taking into account the isolation criterion, events of this nature will be referred to as isolated photon fragmentation events. The requirement of isolation reduces their contribution to the measured cross-section [3].

Despite the relatively low frequency of isolated photon events, background events that give distortion in the measured spectra can also occur. The main background is provided by neutral mesons with high transverse momentum, such as π^0, η mesons, which can decay into two photons formed in the process of jet fragmentation. In order to reduce the proportion of such background events, the isolation cone around the isolated photon in the coordinates (η, φ) is used in the experimental data. But even after using isolation, there is still a fraction of background events in the data. Due to the large cross section of jet formation, the fraction of background from neutral mesons is approximately equal to the fraction of signal – true isolated photons. This part of the background events is subtracted by statistical methods.

The research of photons has one significant advantage compared to many other studies of high-energy particles that are born in collisions, the photons are stable and so are measured in the detector unchanged since they were emitted from the colliding particles. Thus, the photon carries information directly from the collision, regardless of other processes. Other elemental particles that can be released by collisions may not exist in isolation. Instead, they undergo a fragmentation process in which other particles are formed, which also fragment until the resulting particles are able to form stable bound states. These stable particles are then observed in the detector. The existence and properties of the original particle are derived from these particle decays. This can increase uncertainties.

The study of isolated photon events is useful for testing theoretical understanding of the structure of matter on a scale smaller than a proton in experiments with a fixed target and colliding beams at HERA and others. Experiment ZEUS published results of first observations of isolated photons with accompanying jets at high transverse momenta

conducted at luminosity of 6.4 pb^{-1} [1]. ZEUS collaboration also published work on measuring the production of isolated photons in deep inelastic *ep* scattering [4]. Isolated photons in deep inelastic *ep* scattering were measured using the ZEUS detector at HERA using an integrated luminosity of 320 pb^{-1}. Measurements were made in ranges of the transverse energy and the pseudo-rapidity of the isolated photon $-4 < E_T^{\gamma} < 15$ GeV and $-0{,}7 < \eta^{\gamma} < 0.9$ for the virtuality of the exchanged photons, Q^2, in the range $10 < Q^2 < 350$ GeV^2 and invariant masses of the hadron system $W_X > 5$ GeV. Parton showers that were simulated with Monte Carlo methods, gave quite a good description of the data on most of the kinematic range. Predictions of Gehrmann-De Ridder et al. [5-7] of order α^3 reproduced the shapes of the experimental results as functions of the transverse energy and the pseudorapidity, but lay lower than the measurements at low Q^2 and low x. The predictions of Martin et al. [8] are mainly below the cross sections that are measured, but close in kinematic regions where lepton radiation is expected to be dominant. Improved data description can be obtained by combining the two corresponding predictions, which raised questions about the need for further calculations fully using the potential measurements. Work of H1 collaboration investigated prompt photons without and with a requirement of an accompanying jets in photoproduction at HERA [9]. The processes of *ep* collisions with the energy of the centre of mass 319 GeV on the detector H1 at HERA with the corresponding integrated luminosity of 340 pb^{-1} were studied. Cross sections were measured for photon and jet transverse energies greater than 6 GeV and less than 15 GeV and a pseudorapidity between -1.0 and 2.4. The differential cross sections were reconstructed as functions of the transverse energy, the pseudorapidity, x_{γ} and x_p. The correlation between the jet and the photon was also investigated. The results are compared with the predictions of theory, based on the collinear approach and the k_T-factorization approach. The predicted cross sections are usually underestimating the data by 20%. Both predictions underestimate measurements at low E_T^{γ}. Form of the cross section as a function of pseudorapidity of photons is best described with the k_T-factorization approach and as functions of other studied variables are fairly well described within the error. However, theorists still had the task of improving the description. Recently it was established that k_T-factorization model and leading order QCD describe well isolated photons in deep inelastic scattering [10, 11]. The comparison of the experimental data with theoretical models was also conducted without trying to correct the predictions generated in PYTHIA to results at the level of partons [12].

FORMULATION OF THE PROBLEM

The purpose of this work is to develop algorithms for obtaining with a high precision the signal of isolated photons from the sample of data collected by the ZEUS detector at the electron-proton collider HERA during 2004-2007 period [13, 14], calculate the differential cross sections using this signal and compare them with predictions of Monte Carlo simulations (MC).

EXPERIMENT AND KINEMATIC SPACE

Investigated data were collected with the ZEUS detector [15] and correspond to the integrated luminosity of 374 pb^{-1} [13, 14]. The high-precision uranium calorimeter of the ZEUS detector made it possible to perform measurements within the pseudorapidity between -0.74 and 1.01. The smallest unit that can independently read in the calorimeter is called a cell. The cells are organized into layers and towers. The cells of the inner layer of each section are called cells of the electromagnetic calorimeter. They have the fine detail required to separate electromagnetic charges and extract prompt photon signal.

Differential cross sections as a function of several variables were measured in the kinematic region determined in the laboratory system of reference as: virtuality of the exchange photon $Q^2 < 1$ GeV^2, inelasticity of the interaction $0.2 < y_{JB} < 0.7$, pseudorapidity of the photon $-0.7 < \eta^{\gamma} < 0.9$, transverse energy of the photon $6 < E_T^{\gamma} < 15$ GeV, and, when a jet was required, transverse energy of the jet $4 < E_T^{jet} < 15$ GeV and pseudorapidity of the jet $-1.5 < \eta^{jet} < 1.8$.

MONTE CARLO EVENT GENERATION

The generation of MC events for the case of *ep* scattering for models and methods used in this paper divides into a set of sequential steps:

• **Hard scattering.** The interaction between particles is described by matrix elements calculated in accordance with Feynman rules. This perturbative step defines the main characteristics of the event. The proton parton is selected according to the parton distribution function (PDF), which describes the probability of finding the parton in the proton by the values of Q^2 and the variable Bjorken x. Photon PDF is used to select the parton of the photon in the case of a resolved event.

• **Radiation of the initial and final states.** The presence of charged or colored objects before or after hard interaction can lead to large corrections related to photonic or gluon radiation. The electromagnetic radiation is modelled according to the theory of quantum electrodynamics. The quantum chromodynamics corrections can be modelled with the so-called model of parton showers (PS) [16] that describes the parton cascade by splitting one parton into two. Possible transitions $q \to qg$, $g \to q\bar{q}$, $g \to gg$. The PS model can be used for the the initial and final state radiation and, therefore, the particle that takes part in the hard interaction may already be derived from the separation of the partons.

An alternative to the PS model is the color dipole model [17], where each pair of colored objects is treated as gluons emitting colored dipoles. The radiation leads to additional radiating dipole gluons as a result of the parton cascade. In the case of *ep*-scattering, the cascade is initiated by a dipole built up by the quark that is struck and the proton residue.

• **Fragmentation.** After the radiation step, as the distances between partons increase, the QCD becomes strongly interacting – and the perturbation theory is broken. Colored partons are combined into colorless hadrons in the fragmentation process. Since the fragmentation region is not perturbative, some phenomenological models are used.

In the Lund string model [18, 19] two color-charged objects are linked together to form a string. As the two particles move away from each other, the potential energy of the string increases until enough energy is accumulated to produce a quark-antiquark pair due to the rupture of the string. The newly created quarks are connected to the free ends of the outgoing string and the process continues until there are stable hadrons.

Alternative to the Lund string models is provided by the model of fragmentation of cluster decay [20]. With this approach, all the gluons in the parton shower break into quark-antiquark pairs. Colorless $q\bar{q}$ pairs form clusters that then break up into hadrons in the final state.

• **Detector simulation.** In the last step, the particles in the final state are passed through the detector simulation to allow the simulation of the detector response. Detector modelling for ZEUS is performed in MOZART (MC for ZEUS analysis, reconstruction and triggers) [21], based on the GEANT program [22] developed by CERN. The properties of the event can be investigated with the help of partons, hadrons or objects of the detector, i.e., particles can be viewed at three levels: parton, hadron and detector.

The parton (generator) level takes into account all particles after the fragmentation step. The hadron level uses all stable particles in the final state formed in the fragmentation step, as well as stable particles that do not undergo hadronisation. In this work, we used a model with the generation of a jet that fragmented into a photon and a jet, and with the generation of particles such as π^0 and η mesons that are forming photons. Finally, the experimentally measured detector level uses all objects obtained after the reconstruction stage, such as tracks and clusters. A direct comparison between data and theory is only possible at one, as a rule, hadron level. As the MC should be represented at all three levels, it can be in used for comparison of calculations on different levels [13,14].

MONTE CARLO SAMPLES

Ten MC samples were obtained for the specified particular purposes in this analysis. For the generation of MC samples, the generator PYTHIA [23, 24] (version 6.221 and 6.416) was used. The formation of events is based on the elements of the scattering matrix for the processes listed in Tables 1 and 2. The choice of these processes is based on the fact that they correspond to the photoproduction of isolated photons studied in this work. PYTHIA calculates parton showers and uses JETSET [25] to simulate the fragmentation of Lund strings. Multiparton interaction is realized by adding interaction between parton-observers in the same event. Generated sample consisted of 951.03 pb^{-1} direct events and 3525.06 pb^{-1} resolved. When choosing PDF in this work it was necessary to take into account the particularities of ZEUS detector and the existing software for the simulation of events measuring with this detector (MOZART, CZAR - Complete ZGANA Analysis Routine, ZEPHYR - ZEUS physics analysis, EAZE - Easy Analysis of ZEUS Events) [21, 26]. Therefore, in both cases, the proton PDF is CTEQ4M [27] and the photon is GRVHO [28, 29].

To get the signal from the measured data most of MC events were generated in PYTHIA that worked in the channel of prompt photon with codes of direct and resolved subprocesses (ISUB) as shown in the Table 1. In addition, the radiated photons, both in the direct and resolved mode, are selected from the two-jet MC sample obtained with the subprocesses shown in Table 2 with hard photon emission in the final state. Namely, these are the processes of photon-lepton - Compton scattering, prompt photons, point photons in the photoproduction and QCD jet. Here f_i means a fundamental fermion of flavor i, q_i – quark, g – gluon and γ – photon. In hadron colliders, the ISUB = 14 and 29 processes provide the main source for the formation of single photons. According to Fig. 1 (a) for ISUB = 34 we have a reaction between the quark (f_i) from the proton and the photon (γ) from the positron that creates quark (f_i) and photon (γ). In the same way we have, for example, in Fig. 1 (b) ISUB = 29 where gluon and quark form a photon and quark. Similarly, Table. 2 lists the processes depicted in Fig. 1 (c, d).

Table 1

The processes included in the generation of non-fragmentation signal PYTHIA MC

Direct ISUB process		Resolved ISUB process	
34	$f_i\gamma \to f_i\gamma$	14	$f_i\bar{f}_i \to g\gamma$
		18	$f_i\bar{f}_i \to \gamma\gamma$
		29	$q_i g \to q_i\gamma$

EAZE [30] is the basis for code analysis and provides a standard format that simplifies the process of writing code. There are two important parts to the design from a user perspective. The first one is the control card file. This file can make various preliminary calls to select the data to be processed by making changes to the standard control charts. This

allows general code guidance. The second part of the user code is called in three stages. Initially, the code is customized, and all the necessary statements are made. Then begins the second part, which runs on each of the data selections.

Table 2

The processes included in the generation of fragmentation signal and background PYTHIA MC

Direct ISUB process	Resolved ISUB process
33 $f_i\gamma \to f_i g$	11 $f_i f_j \to f_i f_j$
54 $g\gamma \to f_k \overline{f}_k$	12 $f_i \overline{f}_i \to f_k \overline{f}_k$
	13 $f_i \overline{f}_i \to gg$
	28 $f_i g \to f_i g$
	53 $gg \to f_k \overline{f}_k$
	68 $gg \to gg$

Most cuts and the preliminary analysis are performed at this point. In the end some final requirements are applied. ORANGE – ROOT [31] for analysis [30] is a program that works within EAZE. ORANGE does, however, have a more detailed set of control charts that use standard code and code that is centrally supported to get started analysing the information. This significantly reduces the amount of time it takes to generate the analysis code, and because the code is centrally maintained, it increases the reliability of the code used.

In this analysis, ORANGE was used to perform pre-selection events and reject deliberately bad events.

SIGNAL EXTRACTION

After the pre-selection provided by ZEUS, there are still some non-*ep* and other background events that are removed by the following conditions:

- -40 cm < Z_{vertex} < 40 cm – the vertex of interaction along the 0Z axis (i.e., along the proton direction) should be in a well-understood region.
- Barrel calorimeter (BCAL) [15] timing less than 10 ns rejects events of sparks of photo-electron multipliers (PEM).
- The transverse momentum P_T must be at least 10 GeV.

BCAL timing is a useful tool for deleting spark and cosmic events. If the time registered in BCAL is very far from the time of the event, then it can be assumed that the energy deposit is not associated with *ep* collision. A timing of 10 ns was chosen after modelling the PYTHIA Monte Carlo program in the previous ZEUS analysis.

Cosmic events, for example, often have a large amount of missing P_T, so that they do not occur from the colliding beams and they are found mainly in the up-down direction (i.e., the axis 0Y).

Events, generated by PEM sparks or charged flux events, where neutrino takes the place of the scattered electron, are also rejected with a cut on the missing P_T. False positive events, which are generated by PEM sparks and background beam gas are also reduced by the BCAL timing cut.

The following cuts were used to obtain a clean sample of photoproduction events:

- If an event has a candidate for deep inelastic scattering (DIS) electron in SINISTRA [32, 33] with a probability of more than 90% and $y_{el} < 0.7$, then such event is removed from the final stack of candidate events for photon.
- $0.2 < y_{JB} < 0.7$

A method that has been well established in other ZEUS publications [34-36] has been used here as well. The lower boundary y_{JB} discards any proton gas residues and other background events, such as cosmic events. The upper limit removes DIS events as well as events that include a lepton that was mistakenly identified as a prompt photon.

For photon finding the use of the so-called free procedure of clustering is recommended, such as k_T clustering algorithm [3, 37] to identify isolated photons. Past ZEUS collaboration articles on isolated photons [4] have applied a k_T clustering algorithm to ZUFO (ZEUS Unidentified Flying Object) [38] to reconstruct candidates for isolated photons as a k_T jet. Therefore, in this analysis the selection of photon signal is carried out by means of reconstruction of candidate for photon by k_T clustering isolation of ZUFO. The ZUFO method defined the photon as the only ZUFO. Isolation was performed according to the requirements so that ZUFO candidate for the photon had at least 90% energy of k_T jet in which he was clustered.

- Pseudorapidity of the candidate is requires such that it was in the acceptance of ZEUS BCAL, where shower shapes are well understood: $0.7 < \eta^{\gamma} < 0.9$.
- The upper bound on $E_T{}^{\gamma}$ is motivated by the level of understanding of the shower shapes and the decrease of the signal at high transverse energies. The lower limit is set due to poor energy resolution at low energies: $6 < E_T{}^{\gamma} < 15$ GeV.
- By requiring that at least 90% of the energy of a candidate for the photon is stored in electromagnetic calorimeter layer, we reduce the hadron background: $F_{EMC} = E_{EMC} / E_{tot} > 0.9$, where E_{EMC} – the energy in the electromagnetic calorimeter layer, E_{tot} – the total measured energy.

Isolation is performed using the variable Z_{KT}, which is defined as:

$$Z_{KT} = E_\gamma / E_{jet},$$

where E_γ is the ZUFO energy of the photon candidate and E_{jet} is the energy of the k_T jet in which the candidate was clustered. A study of the Frixione isolation [39] and its subsection – conical isolation was also carried out.

Cone isolations is determined by using a variable Z_{cone}, that is the candidate energy E divided by E_{cone} - the total energy in the η - φ cone with a radius of 1.0 around the candidate (including the energy of the candidate itself), i.e.,

$$Z_{cone} = E_\gamma / E_{cone}$$

- For the study of different isolations, the following cut was used: $Z_{cone} > 0.9$.

Stephano Frixione proposed a form of isolation that, as he claims, would remove fragmentation events. The idea is to use not only one cone, but concentric series of cones with radius $\rho \leq \rho_0$ such that inside such cone, total E_T is less than function $\chi(\rho) = E_\gamma\ \epsilon_\gamma((1-\cos(\rho))/(1-\cos(\rho_0)))^n$. The simple cone algorithm considers one cone $\rho_0 = 1$ and $\epsilon_\gamma = 0.1$. A satisfactory discrepancy within the error range between the results of using different isolations was found. Due to the fact, that in this analysis Frixione method and simple cone isolation does not provide a significant benefits we use the following cut: $Z_{KT} > 0.9$.

- Also, the requirement that there was no track in 0.2 units in $\eta - \varphi$ was used: $\Delta Rtrack > 0.2$,

where $\Delta Rtrack = \sqrt{(\eta_\gamma - \eta_{track})^2 + (\varphi_\gamma - \varphi_{track})^2}$

- The tracks had to have a transverse momentum $p > 250$ MeV. This reduction also discards electrons and other charged background.

The jets are clustered with the k_T algorithm [3]. Preliminary analysis of the prompt photons in ZEUS uses cone algorithm grounded on the definition of jets in which the jet made up of all the particles, which are inside the cone in $\eta - \varphi$. However, this algorithm is not infrared safe (i.e., the observables depend on the physics of low-energy/large distances), and therefore, in case if the particles in the jets emit a large amount of soft (i.e., with low E_T) particles, the number of found jets and their properties will be different.

Prompt photon events can be viewed in an inclusive form and with an accompanying jet requirement. In the latter case, the jets must undergo a selection of cuts of $4 < E_T^{jet} < 35$ GeV and $-1.5 < \eta^{jet} < 1.8$.

To further separate the photon signal from the background of neutral mesons π^0 and η a variable $<\delta Z>$ is used, which is defined as:

$$< \delta Z > = \sum_i |Z_i - Z_{cluster}| / (w_{cell} \sum_i E_i),$$

where Z_i is the Z position of the center of cell i, $Z_{cluster}$ - the cluster center, w_{cell} - the width of the cell in Z direction, E_i energy recorded in the cell and the sum is done by all cells in the cluster. The distributions $<\delta Z>$ for MC photons and background π^0 and η mesons, as defined in the selection procedure, are shown in Fig. 2. Here, the solid line denotes the photon signal and the dotted line is the background of the neutral mesons π^0 and η.

There is a noticeable peak in photon distribution at about ~ 0.1, which corresponds mainly to the showers contained in a single cell. Then there is a "shoulder" up to ~ 0.6, where the photon falls close to the center of the cell and splits its energy into two cells, or the photon undergoes early pair formation (preshower). Next, note the small peak at ~ 0.5, where the photon hits the boundaries of the cells and spreads its energy evenly to two adjacent in Z cells or where e^+e^- from the conversion of the photon hit adjacent in Z cells.

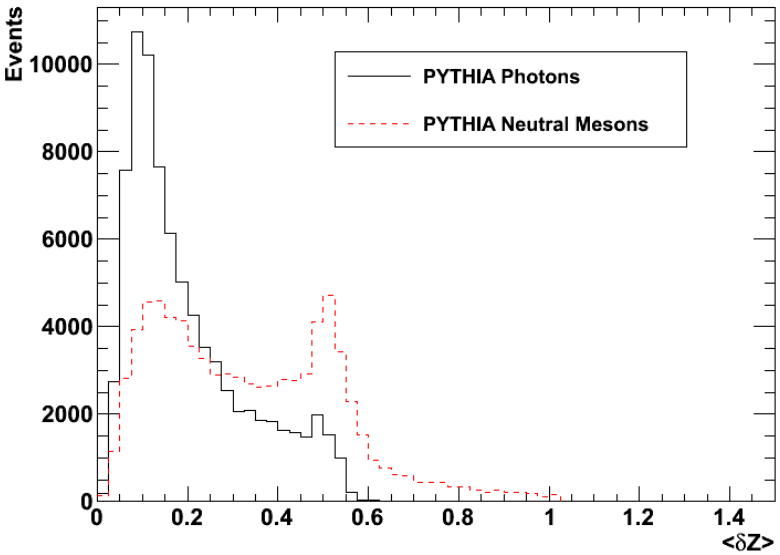

Fig. 2. Comparison of the $<\delta Z>$ distribution in MC for signal of photoproduction of resolved and direct photon with background from neutral mesons π^0 and η

The background curve has a small peak in the region $0.1 < \langle \delta Z \rangle < 0.2$ with a further noticeable peak centered at $\langle \delta Z \rangle = 0.5$. The first peak is the result of π^0 decay with an angle close to the minimum that will hit the calorimeter with similar values of Z, thus giving a narrow width in Z. The peak at 0.5 is a geometric effect in which two photons from π^0 decay strike cells adjacent to Z, distributing their energies equally between the two cells, giving a width of 0.5. At large $\langle \delta Z \rangle$ the tail disappears shortly after 0.5 (by analogy with the distribution of photons), because if the decay photons fall on non-adjacent cells, they will be reconstructed as two separate objects.

Thus, applying the least squares method to the distribution of $\langle \delta Z \rangle$ by statistical subtraction of the background we can derive from the data N_{SIG} – the number of signal events.

CALCULATION OF CROSS SECTIONS

The full cross section is calculated by the equation:

$$\sigma = 1/L * N_{SIG}/A,$$

where σ is the cross section, L is the integrated luminosity, and N_{SIG} is the number of signal events observed at the detector level, which is modified to account for the detector loss using the MC-based evaluation of the acceptance factor, which gives the total number of signal events.

Cross sections are presented differentiated in bins (i.e., subintervals) of transverse energy and pseudorapidity of the photon $E_T{}^{\gamma}$ and η^{γ} and the jet $E_T{}^{jet}$, η^{jet}, and the fraction of the momentum of the photon x_{γ}^{meas} which is being carried by the interacting parton

$$x_{\gamma}^{meas} = \frac{E^{\gamma}+E^{jet}-p_Z^{\gamma}-p_Z^{jet}}{E^{all}-p_Z^{all}},$$

where E^{γ}, E^{jet} – photon and jet energies, p_Z – the corresponding longitudinal momentum, "all" denotes all particles measured in the event in the final state.

For any bin ΔY variable Y (it could be E_T^{γ} and η^{γ}, E_T^{jet}, η^{jet} or x_{γ}^{meas}) the differential cross section with respect to the Y, $d\sigma / dY$, is given as

$$d\sigma/dY = 1/\Delta Y * 1/L * N_{SIG} * C,$$

where N_{SIG} and L are calculated for events in the range ΔY, and C is the factor of acceptance correction:

$$C = 1/A.$$

COMPARISONS WITH PREVIOUS MEASUREMENTS

The differential cross sections as a function of η^{γ}, measured in a defined phase space, are shown in Fig. 3. The ZEUS data of this work are shown in black squares, the previous ZEUS results [40] are blue and H1 results [9] are red. The measured phase spaces are not identical to the ZEUS HERA-I measurements and the H1 HERA-II publication; the current ZEUS measurement has a cut of $-0.7 < \eta^{\gamma} < 0.9$, while the H1 measurement has a cutoff of $-1.0 < \eta^{\gamma} < 2.4$. Previous ZEUS measurements use cone-based isolation and have a lower cut-off at $E_T{}^{\gamma} > 4$ GeV, whereas H1 and current ZEUS measurements are 6 GeV. For all given points, the internal error lines are statistical uncertainties, and the outer error lines represent statistical and systematic squared errors. ZEUS points are offset for clarity of comparison of form dependency.

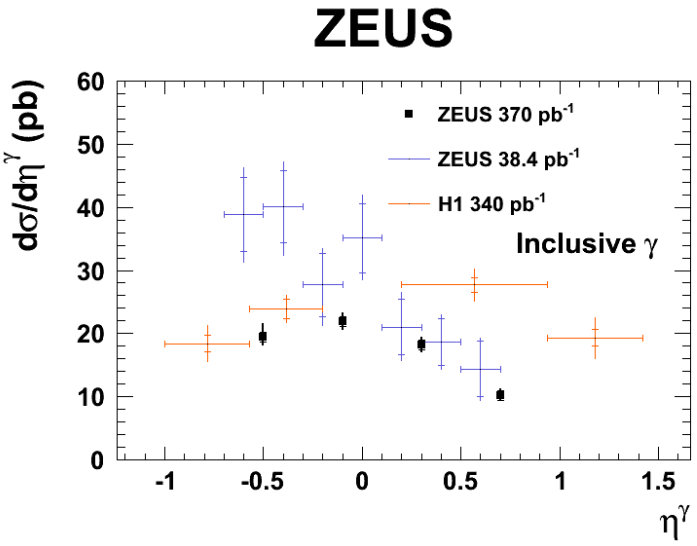

Fig. 3. Differential inclusive cross section of isolated photons as a function of η^{γ} within a defined kinematic region in comparison with previous HERA measurements.

It is clear that all HERA measurements show a decrease in cross section with increasing pseudorapidity, and all measurements agree with one another within errors and taking into account different binning and slightly different kinematic regions. The new ZEUS results presented here demonstrate significantly improved uncertainties. Both statistical and systematic errors were smaller than in the previous ZEUS results compared to the H1 uncertainties, especially given the broader H1 bins.

COMPARISONS WITH THE MONTE CARLO MODEL

Differential cross sections using full phase space are shown for inclusive photons for η^{γ} and $E_T{}^{\gamma}$ in Fig. 4 and for photons with the requirement of an accompanying jet for η^{γ}, $E_T{}^{\gamma}$, η^{jet}, $E_T{}^{jet}$ and x_{γ}^{meas} in Fig. 5. As before, the measured ZEUS cross sections are shown in black squares and the internal error lines show statistical uncertainty and the outer error lines are statistical and systematic errors squared. In addition, MC model predictions are shown. Uncertainty of results of the modelling originating from dependence of cross sections of events, which are calculated in the generator PYTHIA, on scales of renormalisation and factorization have been found sufficiently small to be neglected. PDFs were not varied due to the specifications of the modelling of the ZEUS system in MOZART, CZAR and others. That is, this study follows the established practice regarding the uncertainties of MC [41, 42].

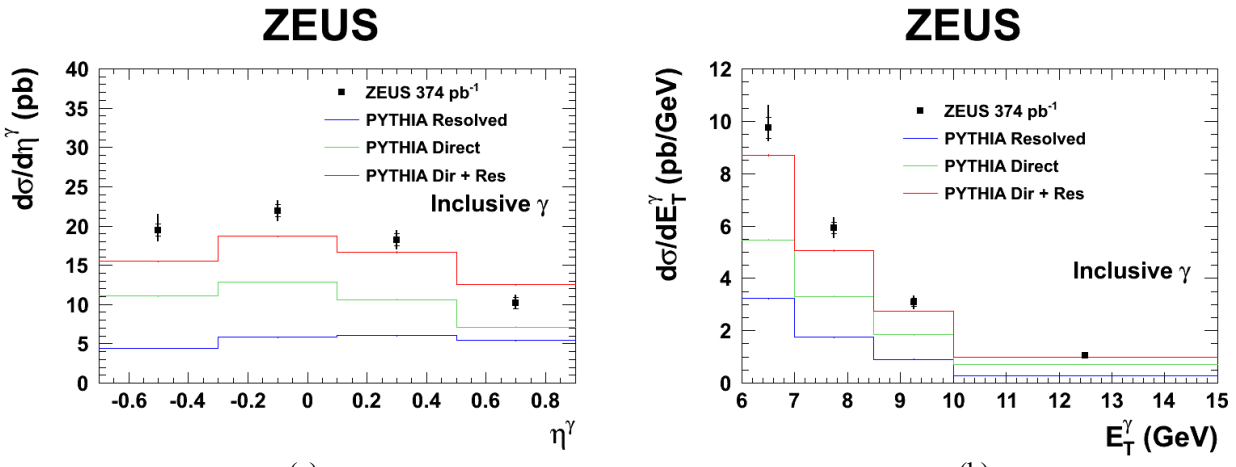

(a) (b)

Fig. 4. Differential inclusive cross sections of isolated photons as a functions of η^{γ} (a) and $E_T{}^{\gamma}$ (b), compared with MC predictions (for the legend see the text)

The prediction for cross sections of production of resolved photons, which is obtained from PYTHIA 6.416, is shown as blue histogram. Contribution of a direct photon (green histogram) is also estimated with PYTHIA 6.416. As can be seen from previous results [43], the simple sum of PYTHIA predictions for direct photons with the MC prediction for resolved photons is significantly underestimating the measured data. Thus, the PYTHIA predictions are normalized to the overall normalization of the MC in a way to fit the data. This overall MC prediction (resolved plus direct) is shown as a solid red line.

Fig. 4 depicts distributions for an inclusive isolated photon. In Fig. 4 (a) a slowly falling cross section with increasing pseudorapidity of the photon is shown, which is described reasonably good by the combined MC prediction. For ZEUS data, the differential cross section shown in Fig. 4 (b) depends on the transverse energy approximately as:

$$d\sigma/dE_T^{\gamma} = 3797.48 * (E_T^{\gamma})^{-3.18}$$

This is well modelled by MC, although the prediction of MC a bit underestimates E_T^{γ}.

Fig. 5 depicts distributions for an isolated photon with the requirement of an accompanying jet. In Fig. 5 (a) we see again a slowly declining cross section with an increase in the pseudorapidity of a photon, which is well described by the combined prediction of MC. The differential cross section as a function of $E_T{}^{\gamma}$ is shown in Fig. 5 (b). It shows a dependence of form similar to that in Fig. 4 (b). Both the $E_T{}^{\gamma}$ and η^{γ} distributions in the case of an accompanying jet are described by the MC better than in the case of an inclusive photon. In Fig. 5 (c) shows the cross section as a function of the pseudorapidity of the jet, which is not well described by the combined prediction of MC for small and large η^{jet}. The differential cross section as a function of the energy of the jet $E_T{}^{jet}$ for ZEUS is shown in Fig. 5 (d) and is described by the MC as well as in the case of $E_T{}^{\gamma}$. In Fig. 5 (e) a steeply rising cross section with increasing x_{γ}^{meas} is shown, which is very well described by a combined prediction. The theoretical calculations are influenced by the parton processes that contain contributions of perturbation theory of QCD beyond the leading order. Discussion of these uncertainties, as well as the contributions of processes higher than the leading order in the perturbation theory of QCD in the study of the phase space specified in this work was carried out earlier [13, 14].

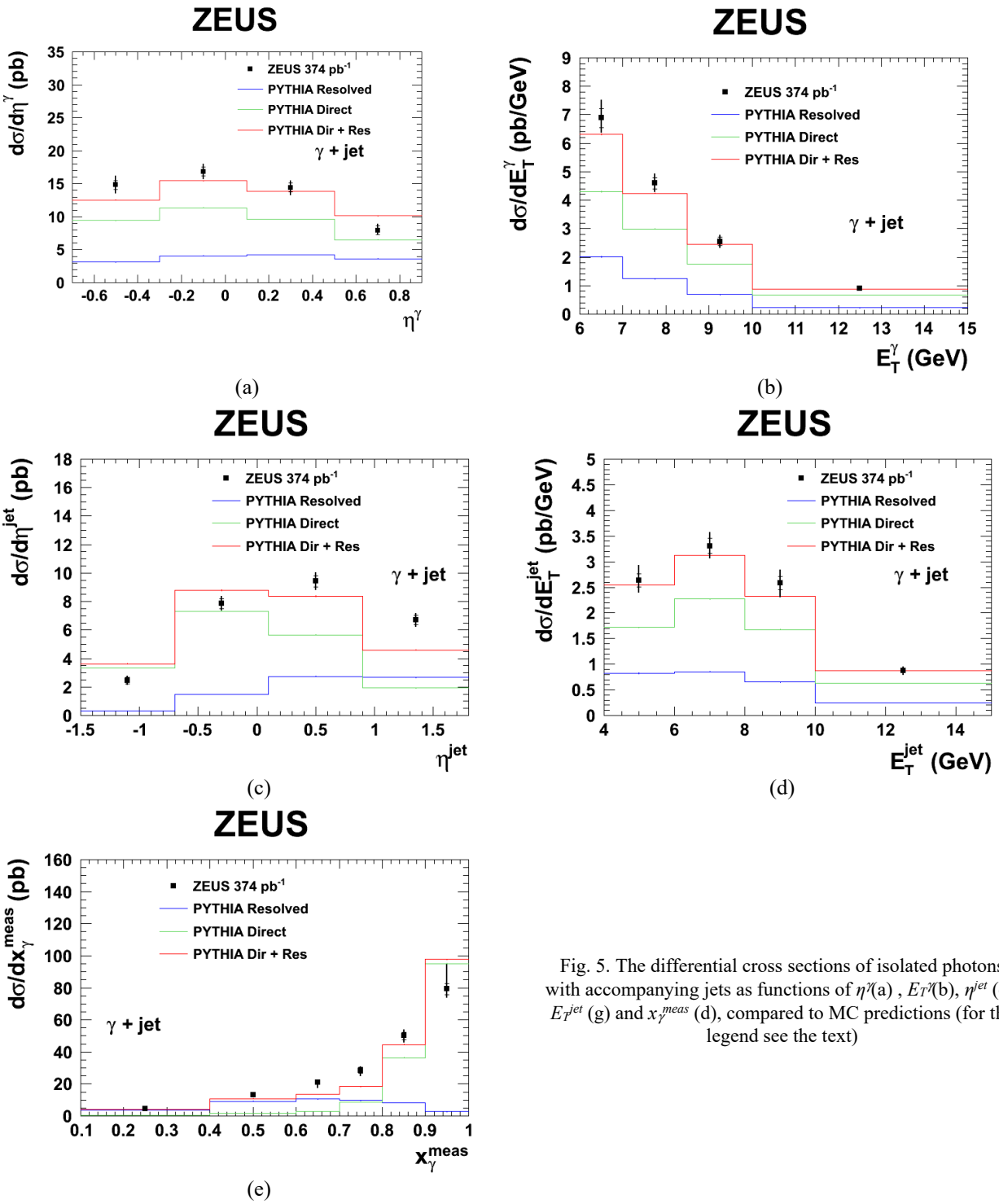

Fig. 5. The differential cross sections of isolated photons with accompanying jets as functions of η^{γ}(a) , E_T^{γ}(b), η^{jet} (c), E_T^{jet} (g) and x_{γ}^{meas} (d), compared to MC predictions (for the legend see the text)

CONCLUSIONS

The inclusive isolated photons and photons with an accompanying jet were measured in photoproduction with the ZEUS detector at HERA accelerator using the integrated luminosity of 374 ± 7 pb^{-1}. These results improved past ZEUS results that were made with lower integrated luminosity. Past publication by ZEUS group dedicated to prompt photons in photoproduction used the data measured with the ZEUS detector at HERA accelerator during 1999-2000. These data corresponded to the integrated luminosity of 77 pb^{-1} [44].

More sophisticated MC simulation samples were generated and applied, unlike in previous studies, where samples were generated for only one particle. The description of the photon signal has been improved. MC predictions underestimate the measured cross sections by a significant amount. One of the reasons for this discrepancy may be the absence in the calculation of contributions of higher orders in perturbation theory of QCD. Uncertainties of results of

modelling that originate from dependency of cross sections, which are calculated in the PYTHIA events generator, on scales of renormalisation and factorization and variations of PDFs are not considered.

Scaling the prediction from the PYTHIA MC generator by a factor of 1.8 is required to normalize the MC to the measured cross sections. After such scaling, the shapes of differential cross sections for variables of the scattered photons, E_T^{γ} and η^{γ}, are well described. Also, within the error the shapes of the differential cross sections as functions of variables for events with a jet E_T^{jet}, η^{jet} and x_{γ}^{meas} are described by MC program, except for large values of η^{jet}, which indicates that further investigation is required.

In the field of isolated photons in *ep*-scattering many possibilities for further studies remain, both in theory and in experiment. These results will be useful for conducting and preparing experiments at future accelerators. The next step may be to improve the existing software system ZEUS (MOZART , ZEPHYR , EAZE etc.) with the latest PDFs such as CT14 [45].

ORCID IDs

Andrii Iudin https://orcid.org/0000-0002-1118-2853, **Sergey Voronov** https://orcid.org/0000-0002-0053-0381

REFERENCES

[1]. J. Breitweg, et al., Physics Letters B **413** (1), 201-216 (1997).
[2]. P. Newman and M. Wing, Rev.Mod.Phys. **86** (3), 1037 (2014).
[3]. S. Catani, et al., Nuclear Physics B, **406** (1), 187-224 (1993).
[4]. H. Abramowicz, et al., Physics Letters B, **715** (1), 88-97 (2012).
[5]. A. Gehrmann-De Ridder, G. Kramer, and H. Spiesberger, Nuclear Physics B, **578**(1), 326-350 (2000).
[6]. A. Gehrmann-De Ridder, T. Gehrmann, and E. Poulsen, Physical Review Letters, **96**(13), 132002 (2006).
[7]. A. Gehrmann-De Ridder, T. Gehrmann, and E. Poulsen, The European Physical Journal C - Particles and Fields, **47**(2), 395-411 (2006).
[8]. S.P. Baranov, A.V. Lipatov and N.P. Zotov, Phys.Rev. **D81**, 094034 (2010).
[9]. F.D. Aaron, et al., The European Physical Journal C, **66**(1), 17-33 (2010).
[10]. O. Hlushchenko, PoS, **DIS2017**, 177 (2018).
[11]. H. Abramowicz, et al., Journal of High Energy Physics, **2018**(1), 32 (2018).
[12]. PJ Bussey, CERN Proceedings, **1**, 175 (2018).
[13]. H. Abramowicz, et al., Phys.Lett. **B730**, 293-301 (2014).
[14]. H. Abramowicz, et al., Journal of High Energy Physics, **2014**(8), 23 (2014).
[15]. A.S. Yudin, O.T. Bogorosh and S.O. Voronov, Наукові вісті НТУУ «КПІ» [Scientific News of NTUU "KPI"], **2(94)**, 110–116 (2014).
[16]. M. Bengtsson and T. Sjöstrand, Zeitschrift für Physik C Particles and Fields, **37** (3), 465-476 (1988).
[17]. G. Gustafson, Physics Letters B, **175**(4), 453-456 (1986).
[18]. B. Andersson, et al., Phys.Rept. **97**, 31-145 (1983).
[19]. B. Andersson, G. Gustafson, and B. Söderberg, Zeitschrift für Physik C Particles and Fields, **20**(4), 317-329 (1983).
[20]. GC Fox and S. Wolfram, Nuclear Physics B, **168**(2), 285-295 (1980).
[21]. T. Haas, and *ZEUS-Note 92-021* (1992).
[22]. J. Allison, et al., Nuclear Instruments and Methods in Physics Research Section A: Accelerators, Spectrometers, Detectors and Associated Equipment, **835**, 186-225 (2016).
[23]. T. Sjöstrand, et al., Computer Physics Communications, **135**(2), 238-259 (2001).
[24]. T. Sjöstrand, S. Mrenna, and P. Skands, Journal of High Energy Physics, **2006**(05), 026 (2006).
[25]. T. Sjöstrand, Computer Physics Communications, **82**(1), 74-89 (1994).
[26]. R. Gläser, and *ZEUS-Note 90-114* (1990).
[27]. HL Lai, et al., Physical Review, D **55**(3), 1280-1296 (1997).
[28]. M. Glück, E. Reya, and A. Vogt, Physical Review, D **46**(5), 1973-1979 (1992).
[29]. M. Gluck, E. Reya, and A. Vogt, Z.Phys. **C48**, 471-482 (1990).
[30]. ZEUS Collaboration, (2013), Vol. 2013. Retreived from: http://www-zeus.desy.de.
[31]. I. Antcheva, et al., Computer Physics Communications, **180**(12), 2499-2512 (2009).
[32]. H. Abramowicz, A. Caldwell and R. Sinkus, Nuclear Instruments and Methods in Physics Research Section A: Accelerators, Spectrometers, Detectors and Associated Equipment, **365**(2), 508-517 (1995).
[33]. R. Sinkus and T. Voss, Nuclear Instruments and Methods in Physics Research Section A: Accelerators, Spectrometers, Detectors and Associated Equipment, **391**(2), 360-368 (1997).
[34]. H. Abramowicz, et al., Journal of High Energy Physics, **2013**(5), 97 (2013).
[35]. H. Abramowicz, et al., Journal of High Energy Physics, **2013**(5), 23 (2013).
[36]. H. Abramowicz, et al., Journal of High Energy Physics, **2013**(9), 58 (2013).
[37]. SD Ellis and DE Soper, Phys.Rev. **D48**, 3160-3166 (1993).
[38]. N. Tuning, and *Internal ZEUS Note* (2001), pp. 1-18.
[39]. S. Frixione, Physics Letters B, **429**(3), 369-374 (1998).
[40]. J. Breitweg, et al., Physics Letters B, **472**, 175-188 (2000).
[41]. M. Aaboud, et al., The European Physical Journal C, **79**(3), 205 (2019).
[42]. T. Yang, EPJ Web Conf. **60**, 14005 (2013).
[43]. FD Aaron, et al., The European Physical Journal C, **54**(3), 371-387 (2008).
[44]. S. Chekanov, et al., The European Physical Journal C, **49**(2), 511-522 (2007).
[45]. S. Dulat, et al., Phys.Rev. **D93** (3), 033006 (2016).

АНАЛІЗ ІЗОЛЬОВАНИХ ФОТОНІВ У ФОТОНАРОДЖЕННІ В PYTHIA

А.С. Юдін[1], С.О. Воронов[2]
[1]European Molecular Biology Laboratory, European Bioinformatics Institute
Хінкстон, Кембридж, Велика Британія
[2] Національний технічний університет України «Київський політехнічний інститут імені Ігоря Сікорського»
вул. Політехнічна, м. Київ, Україна

Зіткнення частинок при високих енергіях на прискорювачах є основним джерелом даних, що використовуються для отримання більш глибокого розуміння фундаментальних взаємодій і структури речовини. Дана робота присвячена аналізу великої кількості даних зіткнень, накопичених на ZEUS у 2004-2007 роках, та запропонованим новим методам розрахунку ізольованих фотонів. Автори розробили програмні алгоритми, що дозволяють отримувати сигнал ізольованих фотонів з даних, зібраних на детекторі ZEUS на електронно-протонному коллайдері HERA, обчислити диференціальні перерізи та порівняти виміряні дані з Монте Карло передбаченнями PYTHIA. Враховуючи особливості детектора ZEUS, фотонний сигнал відокремлюється від фонових подій і обчислюється кількість ізольованих фотонів. Для моделювання взаємодії частинок у детекторі використовувалися обчислювальні математичні та чисельні методи. Розраховано та порівняно з експериментальними даними передбачення Монте Карло моделі диференціальних перерізів як функції псевдобистроти та поперечної енергії фотону η^{γ}, E_T^{γ} та струменя η^{jet}, E_T^{jet} та частки імпульсу фотона x_{γ}^{meas} яку несе партон, що взаємодіє. Результати дослідження порівнюються з попередніми дослідженнями і вперше показують, що всі HERA вимірювання узгоджуються одне з одним. Нові результати показують покращену невизначеність. Утворення ізольованих інклюзивних фотонів і фотонів із супроводжуючим струменем було виміряне в фотонародженні детектором ZEUS на прискорювачі HERA з використанням інтегральної світності 374±7 пб$^{-1}$. Вперше було згенеровано та застосовано більш складні зразки Монте Карло симуляції ізольованих фотонів для детектора ZEUS та покращено опис сигналу фотонів. Встановлено, що PYTHIA досить добре описує форму перерізу як функцію η^{γ}, але не повністю відтворює форму E_T^{γ}, E_T^{jet} і та середній проміжок x_{γ}^{meas}, тоді як η^{jet} описується не дуже добре. Причиною такої розбіжності може бути відсутність виправлень вищих порядків у передбаченнях перерізів прямих фотонів. Масштабування перерізів, отриманих за допомогою PYTHIA, покращує опис E_T^{γ} і η^{γ}. Незадовільний опис η^{jet} свідчить про необхідність подальших досліджень.

КЛЮЧОВІ СЛОВА: ізольовані фотони, фотонародження, струмінь, Монте Карло, PYTHIA, електрон-протонне зіткнення

АНАЛИЗ ИЗОЛИРОВАННЫХ ФОТОНОВ В ФОТОРОЖДЕНИИ В PYTHIA

А.С. Юдин[1], С.А. Воронов[2]
[1]European Molecular Biology Laboratory, European Bioinformatics Institute
Хинкстон, Кембридж, Великобритания
[2]Национальный технический университет Украины «Киевский политехнический институт имени Игоря Сикорского»
ул. Политехническая, 6 г. Киев, Украина

Столкновения частиц при высоких энергиях на ускорителях являются основным источником данных, используемых для более глубокого понимания фундаментальных взаимодействий и структуры вещества. Процессы рождения изолированных фотонов обеспечили множество тестов теоретического описания вселенной на масштабах меньших, чем протон. Эта работа посвящена анализу большого количества данных столкновений, накопленных на ZEUS в период 2004-2007 гг. и новым предложенным методам расчётов изолированных фотонов. Авторы разработали программные алгоритмы, которые позволяют получать сигнал изолированных фотонов из данных, собранных на детекторе ZEUS на электрон-протонном коллайдере HERA, вычислять дифференциальные сечения и сравнивать измеренные данные с Монте Карло предсказаниями PYTHIA. Принимая во внимание особенности детектора ZEUS, фотонный сигнал отделяется от фоновых событий и рассчитывается количество изолированных фотонов. Для моделирования взаимодействия частиц в детекторе были использованы вычислительные математические и численные методы. Рассчитано и сравнительно с экспериментальными данными предсказания Монте Карло модели дифференциальных сечений как функции псевдобыстроты и поперечной энергии фотона η^{γ}, E_T^{γ} и струи η^{jet}, E_T^{jet}, и доли импульса фотона x_{γ}^{meas}, которую несет взаимодействующий партон. Результаты исследования сравниваются с предыдущими исследованиями и впервые показывают, что все измерения HERA изолированных фотонов согласуются друг с другом. Новые результаты показывают улучшение неопределенности. Образование изолированных инклюзивных фотонов и фотонов с сопутствующей струей было измерено в фоторождении с помощью детектора ZEUS на коллайдере HERA с использованием интегральной светимости 374 ± 7 пб$^{-1}$. Впервые были созданы и применены более сложные образцы Монтен Карло симуляций изолированных фотонов для детектора ZEUS, а также улучшено описание фотонного сигнала. Было установлено, что PYTHIA достаточно хорошо описывает форму поперечного сечения как функцию от η^{γ}, но не полностью воспроизводит форму E_T^{γ}, E_T^{jet} и среднюю область x_{γ}^{meas}, тогда как η^{jet} описывается не очень хорошо. Причиной такого несоответствия может быть отсутствие поправок более высоких порядков в предсказаниях для сечений прямых фотонов. Масштабирование сечений, полученных с помощью PYTHIA, улучшает описание E_T^{γ} и η^{γ}. Неудовлетворительное описание η^{jet} указывает на необходимость дальнейших исследований.

КЛЮЧЕВЫЕ СЛОВА: изолированные фотоны, фоторождение, струя, Монте Карло, PYTHIA, электрон-протонное столкновение

East Eur. J. Phys. **3**. 21-28 (2019) DOI:10.26565/2312-4334-2019-3-03

PACS: 98.62.Sb

FIXED POINTS FEATURES IN N-POINT GRAVITATIONAL LENSES

Volodymyr Shablenko
V.N. Karazin Kharkiv National University
4, Svobody sq., 61022, Kharkiv, Ukraine
E-mail: Shablenkov@gmail.com
Received 15 July 2019; revised August 5, 2019; accepted August 30, 2019

A set of fixed points in N-point gravitational lenses is studied in the paper. We use complex form of lens mapping to study fixed points. There are some merits of using a complex form over coordinate. In coordinate form gravitational lens is described by a system of two equations and in complex form is described by one equation. We transform complex equation of N-point gravitational lens into polynomial equation. It is convenient to study polynomial equation. Lens mapping presented as a linear combination of two mappings: complex analytical and identity. Analytical mapping is specified by deflection function. Fixed points are roots of deflection function. We show, that all fixed points of lens mapping appertain to the minimal convex polygon. Vertices of the polygon are points into which dimensionless point masses are. Method of construction of fixed points in N-point gravitational lens is shown. There are no fixed points in 1-point gravitational lens. We study properties of fixed points and their relation to the center of mass of the system. We obtained dependence of distribution of fixed points on center of mass. We analyzed different possibilities of distribution in N-point gravitational lens. Some cases, when fixed points merge with the center of mass are shown. We show a linear dependence of fixed point on center of mass in 2-point gravitational lens and we have built a model of this dependence. We obtained dependence of fixed point to center of mass in 3-point lens in case when masses form a triangle or line. In case of triangle, there are examples when fixed points merges. We study conditions, when there are no one-valued dependence of distribution of fixed points in case of 3-points gravitational lens and more complicated lens.
KEY WORDS: gravitational lensing, fixed points, deflection function, lens mapping

Effect of gravitational lensing has evolved from a method of verification of general relativity to separate field over the years. Using gravitational lenses, stars, stars system and even planets can be found.

Often numerical methods were used to analyze gravitational lenses and analytically were described only special symmetrical systems [1,2]. But these days, gravitational lenses are studied using analytical methods, particularly using methods of algebraic geometry [3-6]. With algebraic geometry methods we were able to study an Einstein ring – an important object in gravitational lensing – and prove that it is the only extended image in N-point gravitational lenses [4].

Circle source in N-point gravitational lens of any configurations was built using methods of algebraic geometry [7].

It is important to study fixed points in the theory of gravitational lenses [8]. Fixed points were researched before [9]. In paper [9] were shown examples of fixed points.

This paper proposes methods to study the distribution of fixed points. We show the distribution of fixed points and study its properties in N-point gravitational lenses.

The goal of this work is studying of a set of fixed points in N-point gravitational lenses using analytical methods, finding features of fixed points.

FORMULATION OF THE PROBLEM

N-point gravitational lens can be described by following equation

$$\vec{y} = \vec{x} - \sum_n m_n \frac{\vec{x} - \vec{l}_n}{|\vec{x} - \vec{l}_n|^2}, \tag{1}$$

where m_n - are dimensionless masses whose position in the plane of the lens is determined by normalized radius-vectors $\vec{l}_n$, $\sum_n m_n = 1$

Equation (1) specifies single-valued mapping from linear vector space R_y^2 (source plane) into linear vector space R_x^2 (image plane):

$$L : (R_x^2 \setminus \Lambda) \to R_y^2, \tag{2}$$

where $\Lambda = \{l_i \mid i = 1,2,...,N\}$ - is a set of radius-vectors $\vec{l}_i$.

Unification of source plane and image plane is referred as picture plane.

Mapping (2) can be described by system of equations:

$$\begin{cases} y_1 = x_1 - \sum_{n=1}^{N} m_n \frac{x_1 - a_n}{(x_1 - a_n)^2 + (x_2 - b_n)^2} \\ y_2 = x_2 - \sum_{n=1}^{N} m_n \frac{x_2 - b_n}{(x_1 - a_n)^2 + (x_2 - b_n)^2} \end{cases} \tag{3}$$

where (a_n, b_n) are coordinates of point C_n in plane R_x^2.

LENS MAPPING COMPLEXIFICATION

It is more convenient to use complex form of lens mapping in order to find fixed points [8]. We introduce new complex variables:

$$\operatorname{Re} z = x_1, \operatorname{Im} z = x_2, \operatorname{Re} \zeta = y_1, \operatorname{Im} \zeta = y_2.$$

New variables are related to old ones as:

$$\begin{cases} x_1 = \frac{z + \bar{z}}{2} \\ x_2 = \frac{z - \bar{z}}{2} \end{cases} and \begin{cases} y_1 = \frac{\zeta + \bar{\zeta}}{2} \\ y_2 = \frac{\zeta - \bar{\zeta}}{2} \end{cases},$$

Using new variables, mapping can be described by following equation:

$$\zeta = z - \sum_{n=1}^{N} m_n \frac{1}{\bar{z} - \bar{A}_n}, \tag{4}$$

where $\sum_{n=1}^{N} m_n = 1$ and $A_n = a_n + ib_n$ are lenses coordinates; $n = 1, 2, ..., N$.

Deflection function was introduced in [8]:

$$\omega = \sum_{n=1}^{N} m_n \frac{1}{\bar{z} - \bar{A}_n} \tag{5}$$

And function is complex conjugated to ω and defined:

$$w = \sum_{n=1}^{N} m_n \frac{1}{z - A_n} \tag{6}$$

It is convenient to use w and ω to find fixed points of lens mapping, except that it is more convenient to use w.

We use properties of complex mapping that were studied in [8]. It is known [8,11] that deflection function $w = w(z)$ is analytical.

There are some theorems.

Theorem 1. Deflection function w can be represented

a) $$w = \frac{Q'(z)}{Q(z)}, \tag{7}$$

where $Q(z) = \prod_{n=1}^{N} (z - A_n)^{m_n}$;

b) $$w = \frac{1}{\deg P(z)} \cdot \frac{P'(z)}{P(z)}, \tag{8}$$

where $P(z)$ - is polynomial;

Theorem 2. (About number). Let n_0 be a number of fixed points of mapping $L:(\mathbb{C}_X \setminus \Lambda) \to \mathbb{C}_Y$, therefore $n_0:\ 1 \le n_0 \le N-1$.

Theorem 3. (About distribution). Fixed points of mapping L belong to the convex polygon that consists of point masses.

N-POINT LENSES

Consider N-point gravitational lens.

We change masses of point lenses and their positions are set to constant. Hence, fixed points depend on N parameters (masses of lenses). Besides, point masses are bounded by masses normalization equation. There is a necessary condition to find the parameters of fixed points distribution parameters. We need the same number of free parameters as number of equations. Therefore, we need either to decrease the number of parameters or to increase the number of equations.

To decrease number of equations we can express masses in terms of masses center of point masses system. It is convenient to describe 2- or 3- points gravitational lenses accordingly to this method. But we need to introduce new additional conditions to describe more complicated systems.

Deflection function of 1-point lens is:

$$w = \sum_{n=1}^{N} m_n \frac{1}{z - A_n} = \frac{m_1}{z - A_1}, \tag{9}$$

where $m_1 = 1,\ A_1 = 0$. There are no fixed points in 1-point gravitational lens.

Deflection function of 2-points lens is:

$$w = \sum_{n=1}^{N} \frac{m_n}{z - A_n} = \frac{m_1}{z - A_1} + \frac{m_2}{z - A_2}, \tag{10}$$

where $m_1 + m_2 = 1$.

Fixed point is given by:

$$z_{st} = A_1 m_2 + A_2 m_1 \tag{11}$$

To find fixed point, we can parameterize point masses in such way $m_1 = s, m_2 = 1 - s, s \in [0,1]$, then

$$z_{st} = A_1 + (A_2 - A_1)s \tag{12}$$

We can also use equation for center of mass: $z_c = m_1 A_1 + m_2 A_2$.

If we express fixed point using the center of mass, we obtain:

$$z_{st} = A_1 + A_2 - z_z. \tag{13}$$

Thus, we obtained equation for fixed point in 2-point gravitational lens. The equation is linear. Masses are located symmetrically in relation to the geometrical center of the system. Fixed point and center of mass can coincide only when there are 2 identical masses. In this case, fixed point and center of masses are located in the geometrical center of the line segment that is connecting 2 masses.

Deflection function of 3-point gravitational lens is:

$$w = \frac{m_1}{z - A_1} + \frac{m_2}{z - A_2} + \frac{m_3}{z - A_3} \tag{14}$$

We have an equation for fixed points:

$$\begin{gathered} z^2 + A_2 A_3 m_1 + A_1 A_3 m_2 + A_1 A_2 m_3 - \\ -\left(A_2 m_1 + A_3 m_1 + A_1 m_2 + A_3 m_2 + A_1 m_3 + A_2 m_3\right) z = 0 \end{gathered} \tag{15}$$

We can set different parameterization for point masses in this case. There are some different mass parameterizations in 3-point gravitational lenses on (fig.1-4). There are gravitational lenses with masses that form triangle on (fig.1-2) and line in (fig. 3-4).

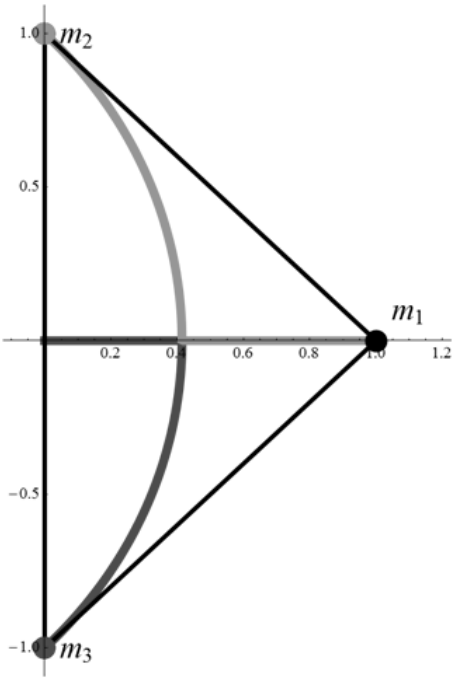

Fig. 1. 3-point lens with
$m_1 = 1 - s, m_2 = s/2, m_3 = s/2, A_1 = 1, A_2 = i, A_3 = -i$

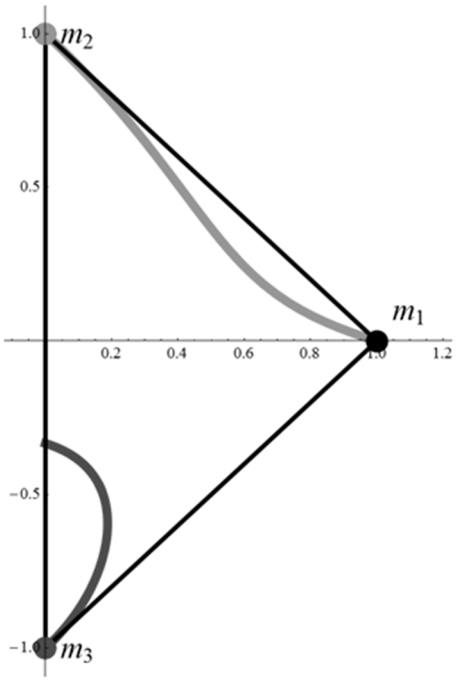

Fig. 2. 3-point lens with
$m_1 = 1 - s, m_2 = 2s/3, m_3 = s/3, A_1 = 1, A_2 = i, A_3 = -i$

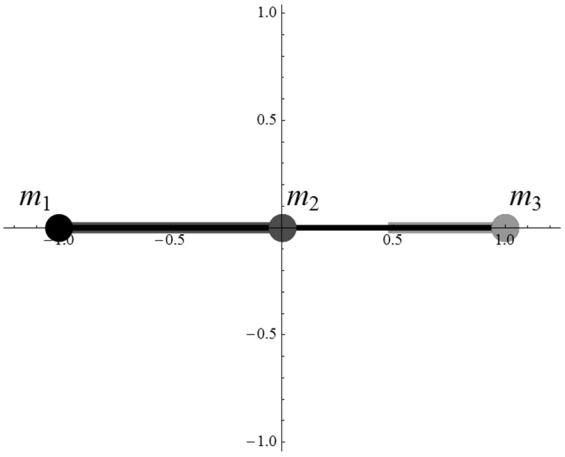

Fig. 3. 3-point lens with
$m_1 = 1 - s, m_2 = s/2, m_3 = s/2, A_1 = -1, A_2 = 0, A_3 = 1$

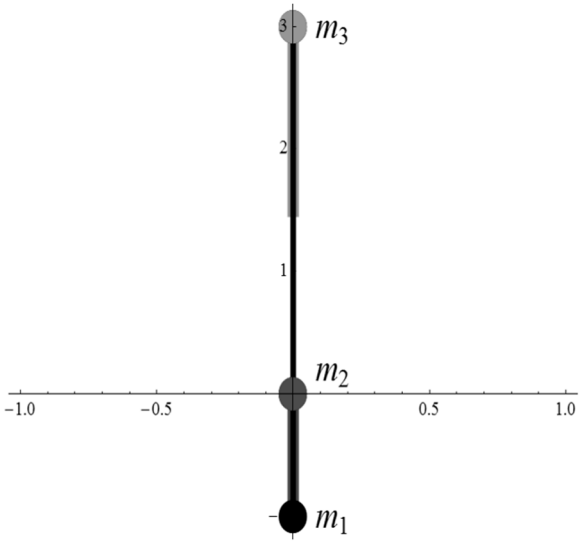

Fig. 4. 3-point lens with
$m_1 = 1 - s, m_2 = s/2, m_3 = s/2, A_1 = -i, A_2 = 0, A_3 = 3i$

We can describe a fixed point using the center of mass:

$$z_c = x_c + iy_c = m_1 A_1 + m_2 A_2 + m_3 A_3, \tag{16}$$

If point masses form a triangle, we can obtain one-valued dependence of fixed points on center of mass. There is only 1 pair of fixed points per each center of mass. We put point masses in positions with $A_1 = a_1 i, A_2 = a_2, A_3 = a_3$. We obtain equation on fixed points:

$$z_{1,2} = \frac{1}{2A_1}[A_1^2 + A_1A_2 + A_1A_3 - A_1x_c - A_1y_c \pm \\ \pm\sqrt{(A_1^2 + A_1A_2 + A_1A_3 - A_1x_c - A_1y_c)^2 + 4A_1(-A_1^2(A_2 + A_3 - x_c) + y_c(A_1A_2 + A_1A_3 - A_2A_3)}] \quad (17)$$

Using technical computing system, Wolfram Mathematica, we built mathematical model that shows the distribution of fixed points. A parameter in the model is the center of mass. To build a more general picture, we set simultaneously horizontal line of the possible center of mass. Thus, we can see 1 line of the center of mass and 2 curves of fixed points that match centers of masses.

Using our model, we obtain when 3-point lens forms equilateral triangle we have 2 fixed points that merge (Fig.5-6). In case when the center of mass of the triangle is geometrical center of the triangle, fixed points are located in 1 point. Situation, when masses are almost equal is shown on (Fig. 5) and equal masses are shown on (Fig.6).

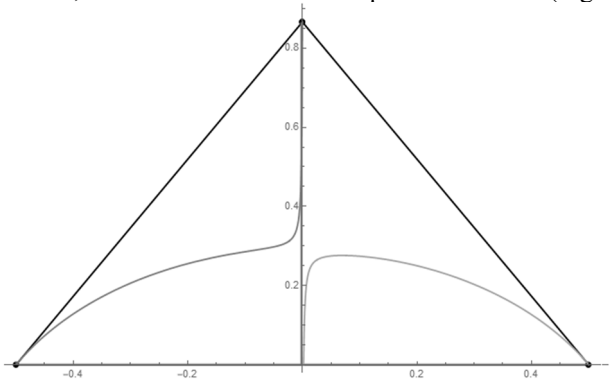

Fig. 5. Equilateral triangle with center of mass near to geometrical center

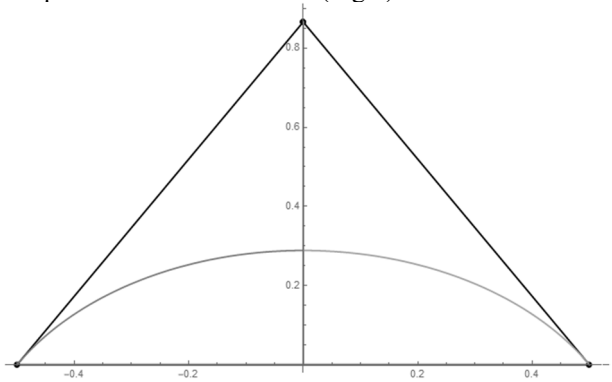

Fig. 6. Equilateral triangle with center of mass in geometrical center

Consider scalene triangle. There was an assumption in [8] that fixed points can merge only in case when point masses form regular polygon. But in case of scalene triangle we have found cases of merging of fixed points. There is a configuration of 3-point gravitational lens when in a forms scalene triangle with the merging of fixed points on (Fig.7-8). A mass configuration with two separate fixed points is shown in (Fig. 7) and configuration with merged fixed points is shown on (Fig. 8).

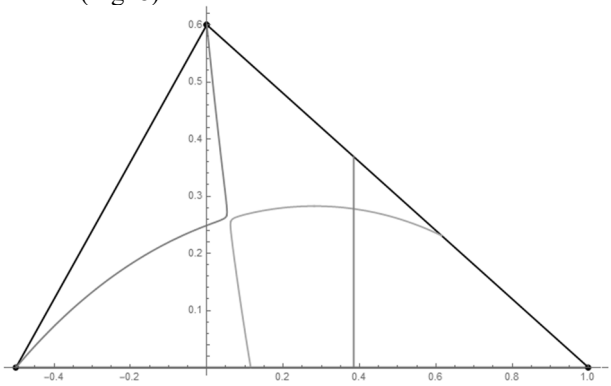

Fig. 7. Scalene triangle with 2 separate fixed points

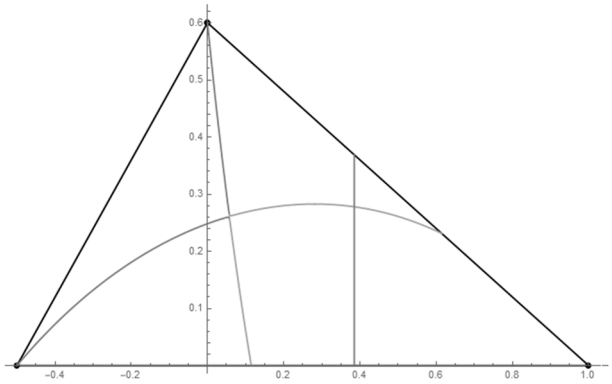

Fig. 8. Scalene triangle with merged fixed points

Fixed points in 3-point gravitational lens can coincide only in case either equilateral triangle or when the system is reduced to 2-point gravitational lens.

If point masses are located along line, number of equations, that are used to describe masses, decreases by 1. In this case we need to introduce 1 additional parameter. The same center of mass can describe different distribution of masses. Considering this feature, we can obtain different fixed points for the same center of mass. We introduce additional parameter, for example, $1-m_2=\alpha$. Thus, changing α, we can obtain different combinations of masses for the same center of mass. And besides, this parameter limits the position of center of mass. For example, when we have 3-point lens with masses in $(-0.5,0),(0,0),(0.7,0)$, position of center of mass is limited by $x_c \in (-0.5\alpha; 0.7\alpha)$.

There is a distribution of fixed points with different α on (Fig. 9). Lenses are located in (-0.5;0), (0,0) and (0.7;0), centers of mass are in (0.1;0). On left image $a=0.26$, on right image $a=0.92$.

Deflection function of 4-point gravitational lens:

$$w = \frac{m_1}{z - A_1} + \frac{m_2}{z - A_2} + \frac{m_3}{z - A_3} + \frac{m_4}{z - A_4} \tag{18}$$

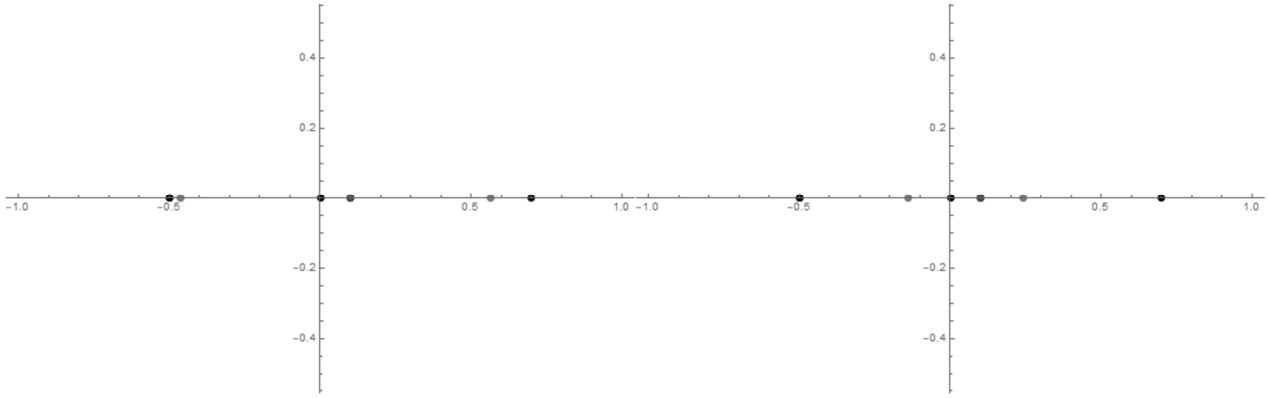

Fig. 9. 3-point lens with masses on a line with different parameter α

Using parameterization, different distributions of fixed points can be obtained. Examples of different parametrization in 4-point gravitational lenses are shown in (Fig.10-12). Triangle consists of 4 masses is shown on (Fig. 10), the square is shown in (Fig. 11) and triangle with 1 internal mass is shown in (Fig. 12).

We need to introduce more additional parameters to study gravitational lenses with 3 or more-point masses. Thus, it is more complicated to apply this method and it is only convenient to study 2- and 3- point gravitational lenses.

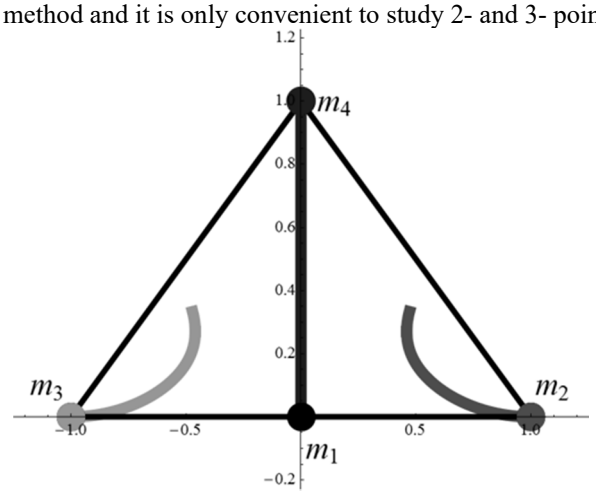

Fig. 10. 4-point lens with $m_1 = 1 - s, m_2 = s/3, m_3 = s/3, m_4 = s/3$ $A_1 = 0, A_2 = 1, A_3 = -1, A_4 = i$

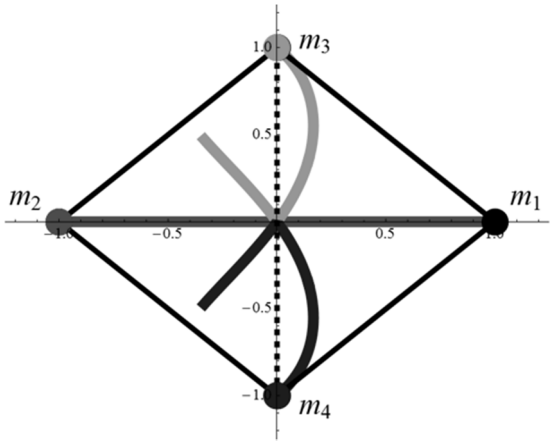

Fig. 11. 4-point lens with $m_1 = 1 - s, m_2 = s/3, m_3 = s/3, m_4 = s/3$ $A_1 = 1, A_2 = -1, A_3 = i, A_4 = -i$

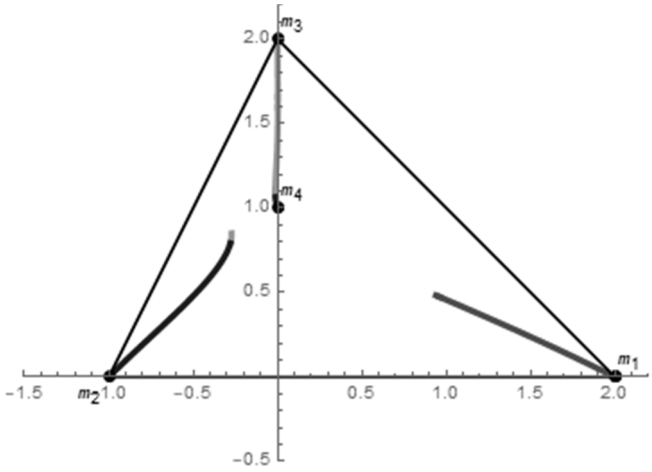

Fig. 12. 4-point lens with $m_1 = 1 - s, m_2 = s/3, m_3 = s/3, m_4 = s/3$ $A_1 = 2, A_2 = -1, A_3 = 2i, A_4 = i$

CONCLUSIONS

Method of obtaining of fixed points distribution in N-point gravitational lenses is shown in this study paper. We show a linear dependence of the fixed point location on center of mass in 2-point gravitational lens. Distribution of fixed points in 3-point gravitational lens is obtained using the center of mass of the system. We show that fixed points in 3-point gravitational lenses can merge. There are examples of distribution of fixed points in 4-point gravitational lens.

ORCID IDs

Volodymyr Shablenko https://orcid.org/0000-0003-4162-4154

REFERENCES

[1] E.Y. Bannikova and A.T. Kotvytskiy, MNRAS 445(4):4435–4442, (2014), DOI: 10.1093/mnras/stu2068.
[2] A.T. Kotvytskiy, TMP 184(1):160–174, (2015), DOI: 10.1007/s11232-015-0315-x.
[3] A.T. Kotvytskiy, S.D. Bronza and S.R. Vovk, Journal of Kharkov National University V.N. Karazin. Series: Physics, **24**, 55-59 (2016)
[4] A.T. Kotvytskiy, S.D. Bronza, K.Yu. Nerushenko and V.Yu. Shablenko, in: *Збірник наукових праць VI-ї Міжрегіональної науково-практичної конференції «Астрономія і сьогодення»: Collection of scientific researches of VI interregional scientific-practical conference "Astronomy and Present"* (Vinnytsia, 2017). pp.198-213 (in Ukrainian)
[5] A.T. Kotvytskiy and S.D. Bronza, Odessa Astronomical Publications, **29**, 31-33, (2016).
[6] S.D. Bronza and A.T. Kotvytskiy, Journal of Kharkiv National University V.N. Karazin, Series: Physics, **26**, 6-32 (2017).
[7] S.D. Bronza, Ju.V. Svyrydova and L.A. Kotvytska, Odessa Astronomical Publications, **31**, 6-10, (2018), DOI: 10.18524/1810-4215.2018.31.144434.
[8] A.T. Kotvytskiy, V.Yu. Shablenko and E.S. Bronza, Odessa Astronomical Publications, **31**, 24-28, (2018), DOI: 10.18524/1810-4215.2018.31.144558.
[9] A.O. Petters and F.J. Wicklin, Journal of Mathematical Physics 39, 1011 (1998), DOI: 10.1063/1.532367.
[10] P. Schneider, J. Ehlers, E.E. Falco, *Gravitational Lenses.* (Springer-Verlag, Berlin Heidelberg, 1997), pp. 266.
[11] H.J.Witt, A&A, **236(2)**, 311-322, (1990).

ОСОБЛИВОСТІ НЕРУХОМИХ ТОЧОК В N-ТОЧКОВИХ ГРАВІТАЦІЙНИХ ЛІНЗАХ

В.Ю. Шабленко

Харківський національний університет імені В.Н. Каразіна
Майдан Свободи, 4, 61022, Харків, Україна

В роботі проведене дослідження множини нерухомих точок в N-точкових гравітаційних лінзах. Для цього була використана комплексна форма лінзового відображення. Комплексна форма має перевагу над координатною: в координатний форми N-точкова гравітаційна лінза задається системою з двох рівнянь, а в комплексному вигляді досить одного рівняння. Це рівняння легко перетвориться в поліноміальне рівняння, яке зручне для дослідження. В роботі лінзове відображення представлено у вигляді лінійної комбінації двох відображень: комплексно-аналітичного і тотожного. Аналітичне відображення задає аналітична функція (функція відхилення). Нерухомими точками є корені функції відхилення. Показано, що всі нерухомі точки лінзового відображення належать мінімальному опуклому багатокутнику. Вершинами мінімального опуклого багатокутника є точки, в яких знаходяться безрозмірні точкові маси. В роботі розглянутий метод побудови нерухомих точок в N-точкових гравітаційних лінзах. Було показано, що нерухомих точок в одноточковій лінзі не існує. Досліджені властивості нерухомих точок і їх зв'язок з центром мас системи лінз. Отримані залежності розподілу нерухомих точок від центра мас. Проаналізовані різні можливі випадки розподілу в N-точкових гравітаційних лінзах. Показано, що у деяких випадках нерухомі точки збігаються з центром мас системи. Було отримано лінійну залежність між нерухомою точкою в двоточковій гравітаційній лінзі та центром мас та побудували модель. Отримали залежність нерухомих точок від центру мас в 3-точковій гравітаційній

лінзі в випадку коли лінза утворює трикутник та пряму. Показали, що в випадку трикутника існують приклади, коли збігаються нерухомі точки. Досліджені умови, коли неможливо однозначно отримати залежність розподілу нерухомих точок від центру мас у випадку 3-точкової гравітаційної лінзи та у більш складних випадках.
КЛЮЧОВІ СЛОВА: гравітаційне лінзування, нерухомі точки, функція відхилення, лінзове відображення

ОСОБЕННОСТИ НЕПОДВИЖНЫХ ТОЧЕК В N-ТОЧЕЧНЫХ ГРАВИТАЦИОННЫХ ЛИНЗАХ

В.Ю. Шабленко

Харьковський национальный университет имени В.Н. Каразина
Площадь Свободы, 4, 61022, Харьков, Украина

В работе проведено исследование множества неподвижных точек в N-точечных гравитационных линзах. Для этого была использована комплексная форма линзового отображения. Комплексный вид имеет преимущество на координатным: в координатном виде N-точечная гравитационная линза задается системой из двух уравнений, а в комплексном виде достаточно одного уравнения. Это уравнение легко превращается в полиномиальное уравнение, которое удобно для исследования. В работе линзовое отображение представлено в виде линейной комбинации двух отображений: комплексно-аналитического и тождественного. Аналитическое отображение задает аналитическая функция (функция отклонения). Неподвижными точками являются корни функции отклонения. Показано, что все неподвижные точки линзового отображения принадлежат минимальному выпуклому многоугольнику. Вершинами минимального выпуклого многоугольника являются точки, в которых находятся безразмерные точечные массы. В работе рассматривается метод построения неподвижных точек N-точечных гравитационных линзах. Было показано, что неподвижных точек в одноточечной линзе не существует. Были исследованы свойства неподвижных точек и их связь с центром масс системы линз. Получены зависимости распределения неподвижных точек от центра масс. Проанализированы различные возможные случаи распределения в N-точечных гравитационных линзах. Показано, что в некоторых случаях неподвижные точки совпадают с центром масс системы. Была получена линейная зависимость между неподвижной точкой в двухточечной гравитационной линзе и центром масс системы и была построена модель. Мы получили зависимость неподвижных точек от центра масс в 3-точечной гравитационной линзе в случае, когда линза образовывает треугольник и прямую. Показали, что в случае треугольника существуют примеры, когда неподвижные точки совпадают. Исследованы условия, когда невозможно однозначно получить зависимость распределения неподвижных точек от центра масс системы в случае 3-точечной гравитационной линзы и в более сложных случаях.
КЛЮЧЕВЫЕ СЛОВА: гравитационное линзирование, неподвижные точки, функция отклонения, линзовое отображение

East Eur. J. Phys. **3**. 29-37 (2019) DOI:10.26565/2312-4334-2019-3-04

PACS: 61.82.Bg, 62.20.-x, 62.65.+k

STRUCTURAL STATE EFFECT ON MECHANICAL PROPERTIES AND ACOUSTIC EMISSION OF HIGH-PURITY TITANIUM AT DIFFERENT TYPES OF DEFORMATION

Kseniya Kutniy*, Igor Kislyak, Alexander Kalchenko, Petr Stoev, Mikhail Tikhonovsky, Pavel Khaimovich**

National Science Center „Kharkiv Institute of Physics and Technology"
1, Akademichna St., 61108, Kharkiv, Ukraine
**E-mail: kutny@kipt.kharkov.ua, **E-mail: kislyak@kipt.kharkov.ua*
Received May 21, 2019; accepted June 27, 2019

The results on investigations of mechanical properties of high-purity titanium with grains ranging from tens of nanometers up to a few micrometers subjected to uniaxial tension, compression and microindenting are presented. Different structural states in high-purity titanium were formed by severe plastic deformation according to the scheme «upsetting – extrusion – drawing» in combination with annealing at temperatures of 250–550° C and quasi-hydrostatic extrusion at room and liquid nitrogen temperatures. The values of yield strengths and microhardness for samples of high-purity titanium with grains of different sizes are determined. It was shown that the combination of severe plastic deformation with cryogenic quasi-hydrostatic extrusion allowed to create high-purity nanocrystalline titanium with high mechanical properties. The obtained experimental data were analyzed for the implementation of the Hall-Petch relation and discrepancy between the values of yield strengths in tension and compression (strength differential or S-D effect). Satisfactory fulfillment of the Hall-Petch relation for high-purity titanium in the whole range of the studied grain size values was shown and a noticeable difference in the yield values for compression and tension was found. The values of the coefficients in the Hall-Petch equation for deformation by tension, compression and microindenting were determined. These coefficients are noticeably lower than the corresponding values for the industrial grades of titanium, i.e. in high-purity titanium, the grain boundaries are weaker barriers for moving dislocations than in the industrial titanium, whose boundaries are enriched with impurities. The features of the acoustic waves emission during compression of samples in various structural states were studied. It was concluded that the deformation of titanium in all the investigated structural states was carried out by dislocation slip.
KEY WORDS: high-purity titanium, nanostructure, tension and compression, Hall-Petch relation, acoustic emission

Titanium and its alloys are important materials for both commercial and medical purposes [1,2]. In particular, high-purity titanium and commercial grade titanium meet virtually all the requirements for the materials of medical implants according to the criteria of biocompatibility, corrosion resistance, hypoallergenicity, and absence (especially in high-purity titanium) of toxic elements [3]. However, the strength level of high alloys seems hardly achievable in pure metals (including titanium). Currently, the only way to increase the strength properties of pure titanium is to create fundamentally new structural states in it, which can be realized using the technology of extreme effects on solids [4]. Such effects include severe plastic deformation (SPD) and deformation at low (cryogenic) temperatures, or cryodeformation (CD) [4]. To obtain ultra-fine grains and extremely high strength characteristics, it seems natural to combine both considered methods of extreme impact on the material (SPD and CD) in the same technological chain [4]. Many schemes for the implementation of SPD [5-10] and CD [11-15] have been proposed. In the case of titanium, such a combination was realized in [12–14]. The SPD application by the method of «upsetting–extrusion–drawing» with subsequent additional drawing at liquid nitrogen temperature [13] allowed to obtain a wire from iodide titanium with the ultimate tensile strength of 1250 MPa, which is, apparently, one of the highest values for the material of a given purity. This strength is conditioned by small grain size, high uniformity of the grain structure and presence of high-angle boundaries. In [16] the role of the initial grain size of high-purity titanium samples, obtained by the SPD method and subsequent annealing, was studied in the evolution of their structure and variation of their properties under the impact of CD by the quasi-hydrostatic extrusion (QHE) method at liquid nitrogen temperature. Such a low-temperature deformation resulted in grains refinement in the high-purity sub-microcrystalline titanium up to nanolevel, i.e. to the size of grains less than 100 nm.

At the same time, the information about the regularities of the variations in the properties of titanium subject to the grain size, and about the mechanisms of metal deformation in the region of ultra-small grains is contradictory. It is known that the yield strength of many metals and alloys increases with the decrease in the grain size according to the known Hall–Petch relation $\sigma=\sigma_0+kd^{-1/2}$ [17]. In some works the classical linear dependence $\sigma(d^{-1/2})$ was found, in the others some facts about the absence of σ dependence on the grain size were noted, as well as the presence of the grain size interval, where a decrease in the yield strength with the decrease in the grain size was observed (the so-called "inverse" or "anomalous" Hall-Petch relation) [18]. Violation of the Hall-Petch law may be caused by a change in the basic mechanism of the material deformation. In this regard, it is of interest to study the mechanical properties of high-purity titanium when varying the grain size from tens of nanometers to several micrometers.

Besides, it is known [19, 20] that in some materials in the process of deformation the so-called S-D effect is observed, which lies in the different yield strengths when they are tested in uniaxial tension and uniaxial compression. We have no reference data about the influence of the grain size on the amount of this effect in the high-purity titanium.

Particular data on the mechanisms of metals and alloys deformation is given by acoustic emission (AE). The acoustic emission waves emitted in the course of the material deformation represent the processes of its dynamic adjustment and are determined by both characteristics of the material itself (structure, chemical and phase composition, etc.) and the conditions of its loading. However, the acoustic emission in the process of titanium deformation was studied, mainly, using the commercial grade VT1-0 titanium [21–23] in the standard coarse-grained state [24–26].

The objective of this work was to study the influence of the structural state of high-purity titanium, obtained by various methods (SPD, CD, annealing), on its mechanical properties in tension, compression and microindentation tests, as well as to study the characteristics of the acoustic emission in the process of the samples compression at room temperature.

MATERIALS AND RESEARCH METHODS

For the research iodide titanium was used, whose impurities content, according to the certificate, was as follows (wt.%): O − 0.01, N − 0.01, C − 0.01, Si − 0.009, Fe − 0.005, Ni − 0.005, Mg − 0.004, Mn − 0.004, Al − 0.005, Cr − 0.005. After double electron beam remelting in high ($1.3\cdot10^{-4}$ Pa) vacuum, the hardness of the obtained ingot was $H_B\approx1.13$ GPa. The ratio of the electrical resistances at temperatures 293K and 77K was $R_{293}/R_{77}=9.62$. The severe plastic deformation was realized in two stages. At the first stage the upsetting-extrusion of the initial ingot and its subsequent drawing into the wire rod were carried out [27]. In this case the ingot was upset from ∅43 mm to∅48.5 mm at room temperature (true, or logarithmic, deformation $e_1=0.24$). Then, the obtained sample was placed into the preheated muffle furnace, heated to temperature T=600°C (the heating process took 20–25 minutes), transported to the extrusion container, preheated to 250°C, and extruded to ∅28 mm ($e_2=1.10$). One more extrusion to ∅10 mm ($e_3=2.20$) was performed in the same way as the first one, with the only difference, that the sample was heated up to 550°C. The obtained wire rod with ∅10 mm was drawn to ∅5 mm at room temperature ($e_4=1.39$). The total true deformation was $e_{SPD}=e_1+e_2+e_3+e_4=4.93$.

The obtained rod with ∅5 mm was taken as the basis for the manufacture of the experimental samples: it was cut into samples 25 mm long, some of which were annealed in vacuum $1.3\cdot10^{-1}$ Pa at temperatures T_{ann}= 250, 300, 350, 450, 550ºC for one hour to achieve different structural states. Then the samples in the initial and annealed states were used both to study the microstructure and mechanical properties and to implement an additional stage of QHE deformation at liquid nitrogen and room temperatures (the QHE technique was described in [28, 29]). The degree of QHE deformation for all the samples was the same and made about 45% (the true deformation $e_5\approx0.6$). The total degree of deformation of the material, which was not subjected to the intermediate annealing, with QHE taken into account, made $e_{total}\approx5.53$.

The samples obtained according to the "upsetting – extrusion – drawing up to ∅5 mm" scheme will be referred to as "SPD"-titanium, with the state specification (un-annealed, i.e., in the initial state, or annealed at the specific temperature T_{ann}), the processes of quasi-hydrostatic extrusion and their results will be indicated as "QHE300" and "QHE77", according to the extrusion temperatures in Kelvins.

The samples microstructure was investigated by transmission electron microscopy method (electron microscope JEM-100 CX).

The microhardness H_μ of the samples was measured on the transverse sections using a PMT-3 microhardness tester with the load of 0.5 N. The mechanical tests in compression and tension were carried out at room temperature on the universal 1958-U10-1 testing machine with the deformation rate of $2\cdot10^{-4}$ s^{-1}. The samples for tension tests had a standard shape of dumbbells with the gage section diameter of 2 mm and length of 15 mm; here the cylindrical samples with the diameter of 3 mm and height of about 4 mm were compressed.

In the process of the samples compression, the resulting acoustic emission (AE) was investigated. To record AE signals the eight-channel acoustic complex M400, developed at the Institute of Mechanical Engineering Problems of the National Academy of Sciences of Ukraine, was used, which allowed recording pulses of different amplitudes [30]. ZTP-19 ceramic piezoelectric transducer (180 kHz resonance frequency) was pressed with a special holder with a constant force through a lubricant layer, which improved the acoustic contact, to the lower side of the sample-bearing platform. When testing samples, after a certain time interval (from 1 to 5 s), the deformation parameters (applied load, grip displacement) and the number of AE pulses, which were received by each of the eight amplitude counters-discriminators of the acoustic complex, were synchronously recorded. Collection, processing and analysis of experimental results were performed using a computer.

EXPERIMENTAL RESULTS AND THEIR DISCUSSION

Microstructure

Electron-microscopic studies of cross sections of deformed rods ∅5 mm showed (Fig. 1a) that the SPD scheme application resulted in formation of the submicrocrystalline state, characterized by an average grain size (subgrain) of about 150 nm (while in the process of warm deformation the grains were refined to 225 nm, the follow-up refinement was caused by drawing them at room temperature). In cross-section the grains have a non-equiaxial shape, and between them a low-angle misorientation prevails. In the longitudinal section of the rod the grains are strongly elongated in the

direction of drawing, and their average size is 2–3 times larger than that in the cross section. In the body of grains a rather high dislocation density is observed.

The samples, cut from the rod, were annealed isochronically for one hour in the temperature range of 250-550ºC. Annealing at temperatures up to 300ºC does not cause a noticeable change in the grain size, but leads to formation of clearer grain boundaries, the dislocation density in them decreases (Fig. 1b). In this case, predominantly small-angle grain misorientation is preserved.

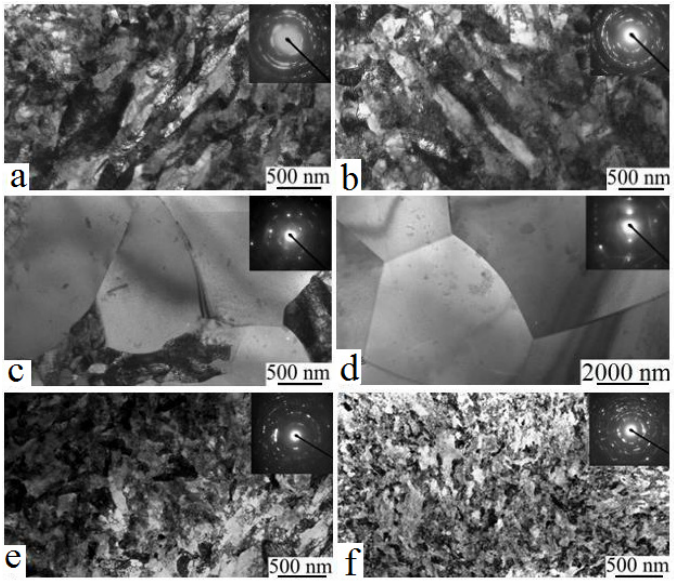

Fig.1. Microstructure of high-purity titanium after SPD, annealing at different temperatures and QHE at room and at liquid-nitrogen temperatures: (a) – SPD; (b) – SPD+annealing at 300°C; (c) – SPD+annealing at 350°C; (d) – SPD+annealing at 550°C, (e) – SPD+QHE300; (f) – SPD+QHE77.

An increase in the annealing temperature to 350°C leads to the onset of the recrystallization process and formation of a bimodal structure with the average grains size of 150 nm and 0.6 μm (Fig.1c). Further annealings at 450° and 550°C (Fig.1d) lead to an intensification of the recrystallization process: the developed grains, having large misorientation and clear thin boundaries, are of the average size of 4 and 9 μm in these samples, respectively.

The microstructure transformation by QHE was studied on the SPD-titanium samples with the initial average grain size of 150 nm (Fig.1a) and on the SPD+annealing samples. The electron-microscopic studies have shown that QHE causes refinement of the grain, but the degree of this refinement substantially depends on the treatment temperature. So, after QHE300 the structure of high-purity SPD-titanium changed a little as compared to that in the initial state: the average grain size made 130 nm (Fig.1e). An increased dislocation density was observed inside the grains. At the same time, QHE77 resulted in a significant refinement of the structure, the average grain size decreased by half and made 75 nm (Fig.1f). In this case the grains in the cross section of the sample became more equiaxial. The high density of point reflections in the micro-diffraction pattern also indicates to a significant refinement of the grains.

Mechanical properties

Figure 2 presents the obtained data on yield strength value $\sigma_{0.2}$ of the samples in the tension and compression studies. The behavior of the dependences turned out to be identical: the $\sigma_{0.2}$ value in samples of the "SPD+annealing" series dropped under compression as sharply as under tension (Fig. 2, curves 1). Quasi-hydrostatic extrusion significantly reduces the role of the preliminary annealing temperature, and this reduction is much more clearly marked at QHE77 (curves 3) than at QHE300 (curves 2). In this case, as can be seen, titanium, which has been treated according to the "SPD+QHE77" scheme, gives the highest value of the yield strength under compression $\sigma_{0.2}\approx$810 MPa.

The hatched areas in Fig. 2 visually demonstrate the above mentioned S-D effect: it can be seen, that in all states of the high-purity titanium under study the yield strength values under compression are higher than those under tension. The observed difference in the values of yield strengths under uniaxial compression ($\sigma_{0.2c}$) and tension ($\sigma_{0.2t}$) determines the value of relative S-D effect Δ. It was calculated by the formula [20]:

$$\Delta = \frac{2(\sigma_{0.2c} - \sigma_{0.2t})}{\sigma_{0.2c} + \sigma_{0.2t}} \cdot 100\% \cdot \quad (1)$$

The Δ values calculated by formula (1) are presented in Fig.3. As can be seen, the nature and value of the S-D effect depend on the structural state of the material. In the initial SPD samples and SPD+(350, 450)°C samples, the value of Δ is approximately constant and makes about 10%, and then it grows sharply to ≈21% for the SPD+550°C samples. The QHE300 treatment results in a more uniform, but inverse change in the value of the effect: from

maximum Δ≈22% for the samples SPD+QHE300 to Δ≈5% for the samples SPD+550°C+QHE300. And finally, the QHE77 treatment results in the loss of any significant dependence of Δ on the previous history of the samples: the effect is almost constant, within the level of ≤10%.

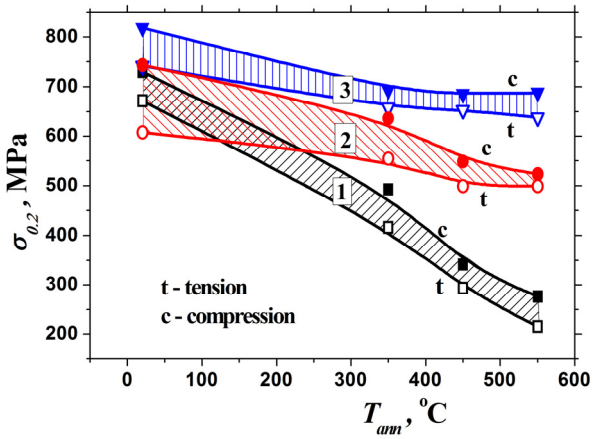

Fig.2. Dependences of the titanium samples yield strengths in compression and tension on the annealing temperature and processing scheme: 1 – SPD+annealing; 2 – SPD+annealing+QHE300; 3 – SPD+annealing+QHE77.

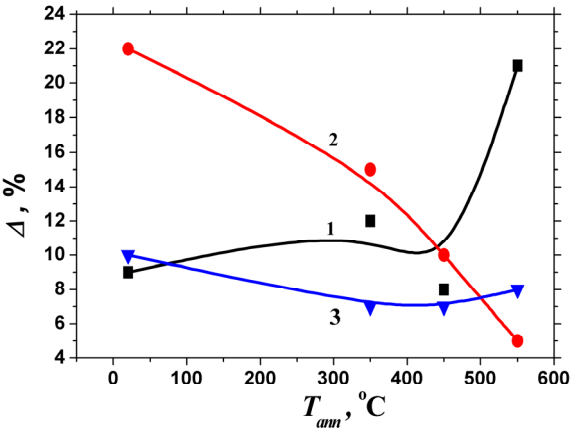

Fig.3. Dependences of the relative value of S-D effect on the annealing temperature and processing scheme: 1 – SPD+annealing; 2 – SPD+annealing+QHE300; 3 – SPD+annealing+QHE77.

The authors [31] reported on the observation of the S-D effect in commercially pure titanium, where its maximum value corresponded to a coarse-grained state (the average grain size was about 15 μm) and made Δ=32%. Here, the value of Δ decreased with grain size decreasing. Apparently, such a high value of Δ may be due to the increased oxygen content in their material (up to 0.34 wt.%, in contrast to 0.01 wt.% in our titanium). As is known, oxygen strongly affects the titanium mechanical properties: it increases strength, reduces ductility, and increases the value of S-D effect [32]. In our samples a high Δ≈21% value was observed for the samples annealed at 550°C and having a fully recrystallized structure and the grain size of 9 μm. At the same time, however, approximately the same Δ≈22% value was determined for the SPD+QHE300 samples having the small grain size of ≈130 nm. This may mean that the grain size is not the only parameter that determines the value of Δ. In [16] it was shown that despite the fact, that the quasi-hydrostatic extrusion of SPD samples at 300 K (SPD+QHE300) results in some grain refinement (130 nm as compared to 150 nm for the SPD samples), the yield strength $\sigma_{0.2t}$ decreases. It was suggested that one of the reasons for this anomalous effect could be a change in the stressed state and density of dislocations. Perhaps these factors also affect the value of the S-D effect.

The obtained data on the mechanical characteristics and grain size in the studied samples of high-purity titanium allowed representing the relationships between them in the Hall-Petch coordinates for the yield strengths in tension (Fig.4a), in compression (Fig.4b) and for microhardness (Fig.5).

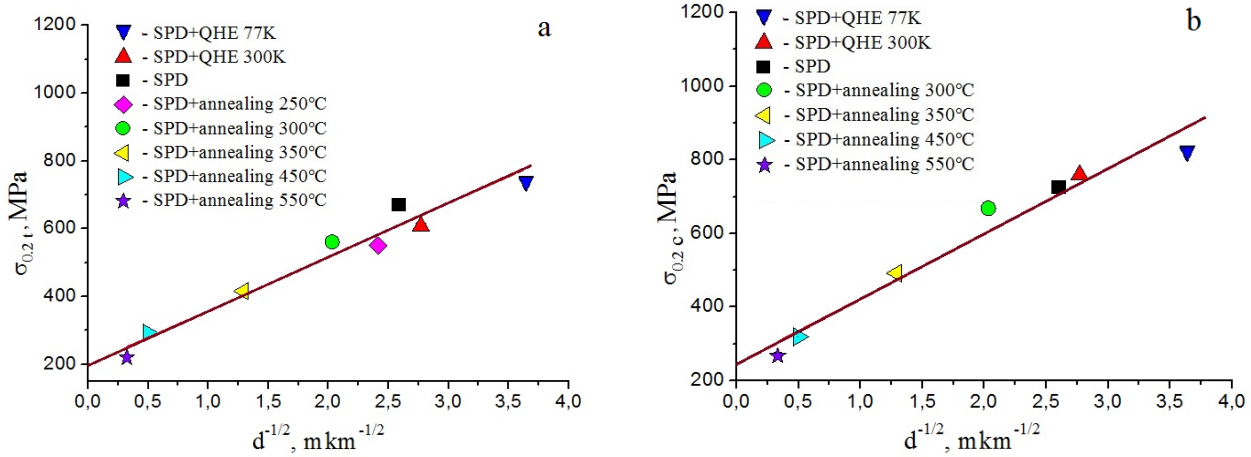

Fig.4. Dependencies of yield strengths in tension (a) and compression (b) on the grain size of the high-purity SPD-titanium after various heat treatments and quasi-hydrostatic extrusion at room temperature and liquid nitrogen temperature.

The presented graphs show that, despite the available scatter of data, in general the Hall-Petch ratio in the case of high-purity titanium is satisfactorily performed over the entire range of grain sizes from 75 nm (SPD+QHE77) to 9 μm (SPD+annealing at 550°C). This means that the most likely mechanism of deformation in the entire specified region is dislocation slip [33].

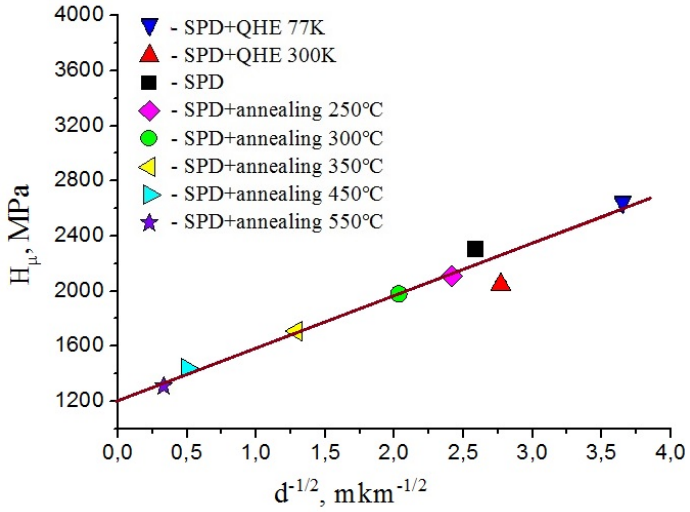

Fig.5. Dependence of microhardness on the grain size of high-purity SPD-titanium after various heat treatments and quasi-hydrostatic extrusion at room temperature and liquid nitrogen temperature.

Note, that the coefficients in the Hall-Petch equation for the yield strength in tension $\sigma_{0.2t}=\sigma_{0t}+k_t\cdot d^{-1/2}$ (k_t=0.155 MPa·m$^{1/2}$), in compression $\sigma_{0.2c}=\sigma_{0c}+k_c\cdot d^{-1/2}$ (k_c=0.178 MPa·m$^{1/2}$) and for microhardness $H_\mu=H_0+k_h\cdot d^{-1/2}$ (k_h=0.375 MPa·m$^{1/2}$) turned out to be much lower than the reference data obtained for the commercial grades of titanium (k_t makes 0.53 MPa·m$^{1/2}$ [18] and 0.21 MPa·m$^{1/2}$ [33] for titanium VT1-00, k_h for this grade of titanium makes 0.65 MPa·m$^{1/2}$ [33], and for titanium VT1-0 k_h makes 0.4 MPa·m$^{1/2}$ [34], 0.7 MPa·m$^{1/2}$ [35] and 0.4 MPa·m$^{1/2}$ [36]). As long as these coefficients characterize the "ease" of plastic deformation propagation through the grain boundaries, i.e. “transparency” of the grain boundaries for the dislocations transition from grain to grain, this result indicates to the fact, that in high-purity titanium the “transparency” of boundaries is higher than in the commercial titanium, in which the boundaries are enriched with impurities.

The values of σ_{0t}, σ_{0c} and H_0 in the Hall-Petch equations characterize the resistance (friction) stress of the crystal lattice to the dislocation slip. For the studied titanium these values are σ_{0t}=200 MPa, σ_{0c}=250 MPa and H_0=1200 MPa. These parameters turned out also lower than those for the commercial grades of titanium. Thus, according to the data by different authors, for VT1-00 σ_{0t} makes 290 MPa [33], for VT1-0, the values of H_0 are 1840 MPa [33], 1500 MPa [34], 1550 MPa) [35] and 1500 MPa [36]. The lower values of these parameters in our titanium are due to the lower concentration of the impurity atoms in the crystal lattice, which make additional obstacles to the dislocations motion.

Acoustic emission

AE signal recording has shown, that the activity, the total amount of the recorded signals and the amplitude distribution of the signals depend on the structural state of titanium.

Figure 6 shows the AE activity curves of the titanium samples after severe plastic deformation and subsequent annealing at temperatures of 350 and 550°C. A significant difference between these curves is observed. Thus, the AE activity of the SPD-titanium samples after a small growth in the initial part of the loading remains very low at further deformation.

The dependences of the AE activity after annealing of SPD-samples at temperatures of 350 and 550°C have quite a different character. In the stage of plastic deformation, the AE activity of these samples sharply grows, and maxima are observed on the AE curves; the absolute values of AE activity increase by an order of magnitude relative to the values at the elastic stress section. It can be seen, that the rise of AE activity in samples annealed at 350°C starts a little later than in the samples with T_{ann}=550°C. It should also be noted, that AE both in the initial SPD-samples and in the annealed samples starts immediately after the deformation onset in the stage of elastic deformations.

Fig. 7 shows graphs (in absolute values) and histograms (in relative values) of the number of pulses, which were recorded by 8 counters. Each of the counters (channels) was adjusted to record the AE signal of certain amplitude. The upper and lower amplitudes of each counter (adjusted to the preamplifier input) were 10-20, 20-30, 30-40, 40-50, 50-60, 60-70, 70-80, and >80 μV.

The analysis showed that histograms of the AE signals distribution in amplitudes had features related to the type of amplitude distribution and the quantitative ratio of high-amplitude AE signals to low-amplitude ones. Usually, in the case of plastic fracture of metals the amplitude distribution has an exponential form, and the number of low-amplitude signals always exceeds the number of high-amplitude ones. Violation of this rule in the process of material deformation is usually associated with a change in the deformation mechanism or the onset of the formation and propagation of cracks. In the tested SPD-titanium the amplitude distribution spectrum contains signals of both low and high amplitudes, but the number of low-amplitude signals is greater than that of the high-amplitude ones (see Fig. 7b). But for the

samples SPD+annealing at 350°C, the number of high-amplitude signals in the spectrum was significantly greater as compared to the number of low-amplitude AE signals. For the samples SPD+annealing at 550°C a sharp increase in the low-amplitude AE signals is observed in the spectrum, and the amplitude distribution is of exponential character (see Fig. 7a).

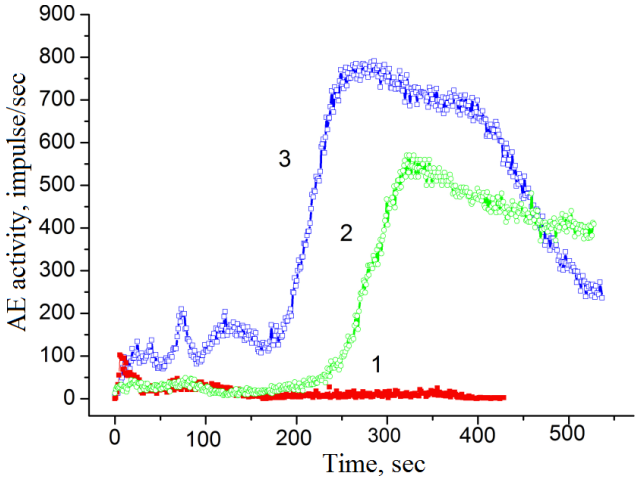

Fig.6. Dependence of AE activity on the titanium samples state: 1 – SPD; 2 – SPD+annealing at 350°C; 3 – SPD+annealing at 550°C.

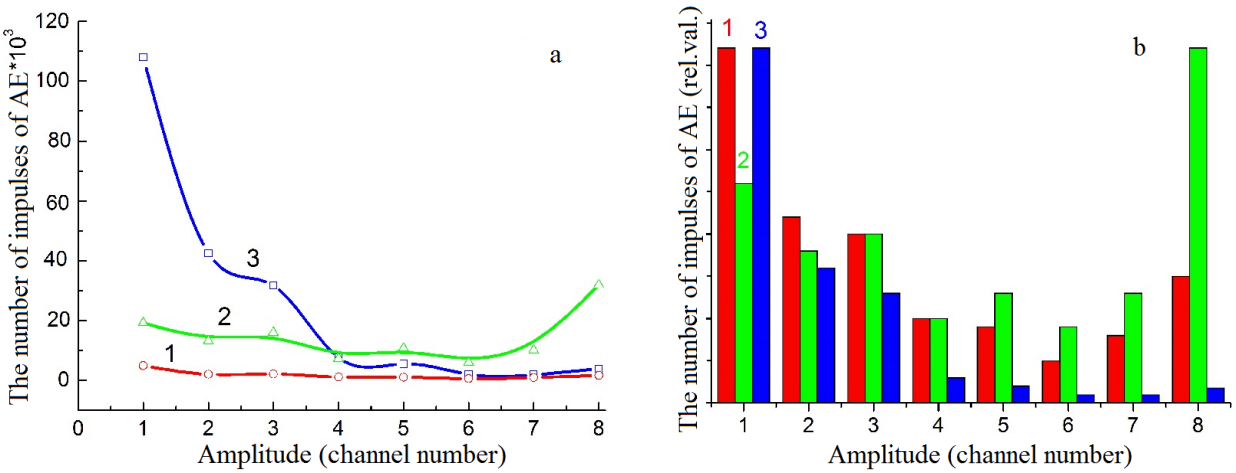

Fig.7. Dependencies of the number of recorded AE signals on their amplitude in absolute (a) and relative (b) units in titanium samples after treatment: (1) – SPD, (2) – SPD+annealing at 350°C, (3) – SPD+annealing at 550°C.

The specific features of the AE activity dependence on the deformation of titanium samples during their loading (Fig. 6) are determined by the structural state of the tested samples. Let us analyze these characteristic properties.

As noted above, in the process of SPD a submicrocrystalline state of titanium is formed with an average grain (subgrain) size of about 150 nm. Annealing at 350°C leads to the onset of the recrystallization process and to the formation of a bimodal structure with an average grain size of 150 nm and 0.6 μm; annealing at the temperature of 550°C leads to recrystallization and formation of grains of 9 μm in size. The microhardness of the SPD titanium samples makes H_μ=2.3 GPa, and, after annealing at 350 and 550°C, it is 1.7 and 1.36 GPa, respectively. Thus, the heat treatment of SPD titanium samples results in an increase in the grain size and a decrease in the hardening (hardness) of the metal.

Numerous experiments have shown, that the acoustic emission depends on the grain size in the metal: with the decrease of the grain size the AE signals generation also decreases [37]. This is due to the fact that, as the grain size decreases, the number of obstacles to dislocation slip, in the form of the grain boundaries, grows. A short distance of the dislocations sliding and an increase in the number of obstacles to their movement result in the decrease in the rate (and, hence, the energy) of the emitted AE pulses. This leads to a lower probability to detect the AE source when the grain size decreases. For the metals with very fine grains, the energy of the emitted pulses may be below the threshold of the equipment sensitivity, and the acoustic emission will not be observed until the sample is destroyed.

Hardening of titanium in the process of SPD and quasi-hydrostatic extrusion also results in a decrease in the AE activity. The effect of hardening on the activity of titanium AE is described in detail in [38].

Thus, the specific features of the AE activity curves for the SPD and SPD+annealing samples at temperatures of 350 and 550°C are determined by the grain size and the value of titanium hardening (hardness). Larger grain size and lower microhardness lead to the fact, that in the samples SPD+annealing at 550°C the plastic deformation starts at lower stress than in the SPD+annealing at 350°C samples (Fig. 6, curves 2 and 3).

The probable cause for the occurrence of specific amplitude distribution of AE in titanium samples SPD+annealing at 350°C, which have a bimodal structure, can be shear bands. Usually, the high-amplitude pulses are attributed to propagation of twins, the number and "power" of which increase with the grain size rise. SPD-titanium is characterized by submicron size grains, in which twinning is completely absent. Probably, the high level of the internal stresses, which is inherent in SPD-titanium, is summed up with the applied external stresses, what results in the formation of a large number of shear bands at the stage of the developed plastic deformation [39]. Elimination of these stresses by annealing (in our case it is annealing of SPD-titanium at 550°C) prevents the occurrence of shear bands, while the grain growth leads to the fact, that the character of the change in the AE low-amplitude component of the titanium, annealed at 550°C (Fig. 6, curve 3), is similar to the change in the activity that was observed when studying the acoustic emission of industrial sheet titanium in the process of its deformation [39]. It is determined by the dislocation mechanism of deformation and the structural features: the distribution of impurities and the degree of dislocations pinning.

To gain a more complete understanding of the detected specific features of AE signals amplitude distribution in titanium samples after SPD and subsequent annealing, further studies are required.

CONCLUSIONS

1. Mechanical tests on uniaxial tension, compression and microindentation of high-purity titanium samples in different structural states, formed by severe plastic deformation in combination with annealing and quasi-hydrostatic extrusion at room and liquid nitrogen temperatures, were carried out. The microstructure of the samples is characterized by an average grain size, which varies from 9 microns to 75 nm. The values of the yield strengths and the micro-hardness values for the samples with different grain sizes were determined.

2. In the obtained samples a noticeable difference was found in the values of the yield strength in compression and tension, the so-called S-D effect. The relative value of the S-D effect, Δ, depends on the structural state of the material and varies from about 10% to 21-22%. At the same time, there is no unambiguous relation between the grain size and the value of Δ.

3. Satisfactory performance of the Hall-Petch relation for the high-purity titanium in the whole range of the studied grain size values was shown. This fact indicates that deformation at the initial stage is realized by one mechanism – dislocations glide. The values of the coefficients in the Hall-Petch equation for tension deformation (k_t=0.155 MPa·m$^{1/2}$), compression (k_c=0.178 MPa·m$^{1/2}$) and for microindentation (k_h=0.375 MPa·m$^{1/2}$) were determined. These coefficients are noticeably lower, than the corresponding values for the commercial grades of titanium, i.e., in high-purity titanium grain boundaries are weaker barriers for moving dislocations. Also, the values of parameters σ_0 and H_0, which characterize the lattice resistance to the dislocation glide, turned out to be lower.

4 Acoustic emission of the high-purity titanium samples in various structural states was studied in the process of deformation by uniaxial compression. The analysis of the AE activity dependence on the degree of deformation and the nature of the amplitude distribution confirms the dislocation mechanism of plastic deformation of nano- and submicrocrystalline titanium samples. In this case, the presence of a significant number of high-amplitude AE signals in the samples with a bimodal microstructure, obtained by severe plastic deformation and annealing at 350°C, may be due to the formation of shear bands.

ORCID IDs

Kseniya Kutniy https://orcid.org/0000-0002-9328-1336, **Igor Kislyak** https://orcid.org/0000-0001-5016-8133,
Alexander Kalchenko https://orcid.org/0000-0003-0856-1868, **Petr Stoev** https://orcid.org/0000-0001-7942-5850,
Mikhail Tikhonovsky https://orcid.org/0000-0001-5889-0366, **Pavel Khaimovich** https://orcid.org/0000-0002-2523-9726

REFERENCES

[1] H.J. Rack and Qazi, Mater. Sci. Eng. C**. 26**, 1269 (2006).
[2] R.Z. Valiev, I.P. Semionova, V.V. Latyshev, A.V. Shcherbakov, E.B. Yakushina, Российские нанотехнологии [Russian Nanotechnologies]. **3**(9-10), 106 (2008). (in Russian).
[3] *Биосовместимость [Biocompatibility],* (Ed. by V.I.Sevastianov, IC VNIIIgeosystem, Moscow, 1999), p. 368. (in Russian).
[4] A.M.Glezer, УФН [Physics-Uspekhi (Advances in Physical Sciences)]. **182**, 559 (2012). (in Russian).
[5] R.Z. Valiev, I.A. Aleksandrov, *Объемные наноструктурные материалы: получение, структура и свойства [Bulk Nanostructured Materials: Mnufacturing, Structure, and Properties],* (Akademkniga, Moscow, 2007), p. 398. (in Russian).
[6] A.A. Popov, R.Z. Valiev, I.Yu. Pyshmintsev, S.L. Demakov, A.G. Illarionov, ФММ [The Physics of Metals and Metallography]. **83**, 127 (1997). (in Russian).
[7] R.Z. Valiev, A.V. Sergueeva, and A.K. Mukherjee, Scripta Mater. **49**, 669 (2003).
[8] S.P.Malysheva, G.A. Salishchev, R.M. Galeyev, V.N.Danilenko, M.M. Myshliayev, A.A.Popov, ФММ [The Physics of Metals and Metallography]. **95**, 98 (2003). (in Russian).
[9] Y. Beygelzimer, V. Varyukhin, D. Orlov, B. Efros, V. Stolyarov, and H. Salimgareyev, in: *TMS Annual Meeting, Ultrafine Grained Materials II*, (Washington, 2002), p. 43.

[10] A.Yu. Yeroshenko, Yu.P. Sharkeyev, A.I. Tolmachov, G.P.Korobitsyn, V.I.Danilov, Перспективные материалы [Advanced Materials]**.** **7**, 107 (2009). (in Russian).
[11] I.M. Neklyudov, V.I. Sokolenko, L.A. Chirkina, G.P. Kovtun, I.F. Borisova, V.V. Kalinovskiy, D.G. Malykhin, E.N. Metolidi, V.S. Okovit, Металлофиз. и новейшие технологии [Metallofizika i Noveishie Tekhnologii]**.** **29**, 359 (2007). (in Russian).
[12] E.D. Tabachnikova, A.V. Podolskiy, S.N. Smirnov, M.A. Tikhonovsky, P.A. Khaimovich, N.I. Danylenko, S.A. Firstov, Вісник Харківського національного університету, Серія «Фізика» [Visnyk Kharkivs'kogo Natsional'nogo Universytetu, Seriya "Fizyka"]. **28**, 63 (2018). (in Ukrainian).
[13] M.A. Tikhonovskii, I.F. Kislyak, O.I. Volchok, T.Yu. Rudycheva, V.G.Yarovoi, A.V. Kuz'min, N.V. Kamyshanchenko, and I.S. Nikulin, ФТВД [Physics and Technology of High Pressures]. **18**, 96 (2008). (in Russian)**.**
[14] K.V. Kutniy , O.I. Volchok, I.F. Kislyak, M.A. Tikhonovsky, and G.E. Storozhilov, Mater. Sci. Engineering Technology (Mat.-wiss.u.Werkstofftech.). **42**, 114 (2011).
[15] V.A. Moskalenko, A.R. Smirnov, and A.V. Moskalenko, ФНТ [Low Temp. Phys.]. **35**, 1160 (2009). (in Russian)**.**
[16] M.A. Tikhonovsky, P.A. Khaimovich, K.V. Kutniy, I.F. Kislyak, V. S. Okovit, and T.Yu. Rudycheva, ФНТ [Low Temp. Phys.]. **39**, 1261 (2013). (in Russian)**.**
[17] P. Lukáč, Z. Trojanová, Materials Engineering. **18**, 110 (2011).
[18] A.V. Nokhrin, V.N. Chuvil'deyev, E.S. Smirnova et. al. *Механические свойства нано- и микрокристаллических металлов. [Mechanical Properties of Nano- and Microcrystalline Metals]* (NNGU, Nizhniy Novgorod, 2007), p. 46. (in Russian).
[19] J.P. Hirth and M. Kohen, Met. Trans. **1**, 3 (1970).
[20] C.A. Pampillo, L.A. Davis, and J.C.M. Li, Scripta Met. **6**, 765 (1972).
[21] H. Tanaka and R. Horiuchi, Scripta Met. **9**, 777 (1975).
[22] M. Frizel and S.H. Carpenter, Metall. Trans. **15A**, 1849 (1984).
[23] J.R. Kennedy, Scripta Met. **16**, 525 (1982).
[24] P.I. Stoev, I.I. Papirov, and V.I. Moshchenok, Вопросы атомной науки и техники, Серия: Вакуум, чистые материалы, сверхпроводники [Problems of Atomic Science and Technology. Section: Vacuum, Pure Materials and Superconductors]. **15**(1), 15 (2006). (in Russian).
[25] P.I. Stoev, I.I. Papirov, Вопросы атомной науки и техники, Серия: Вакуум, чистые материалы, сверхпроводники [Problems of Atomic Science and Technology. Section: Vacuum, Pure Materials and Superconductors]. **16**(4), 119 (2007). (in Russian).
[26] E.Z. Kayumova, V.V. Astanin, and A.A. Girfanova, Письма о материалах [Materials Letters]**.** **3**, 193 (2013). (in Russian).
[27] I.F. Kislyak, K.V. Kutniy, M.A. Tikhonovsky, A.I. Pikalov, T.Yu. Rudycheva, N.F. Andrievskaya, and R.L. Vasilenko, ФТВД [Physics and Technology of High Pressures]. **23**, 53 (2013). (in Russian).
[28] P.A. Khaimovich, Low Temperature Physics. **44** (5), 349 (2018).
[29] P.A. Khaimovich, Перспективные материалы [Advanced Materials]**.** **3**, 363 (2009). (in Russian).
[30] I.I. Papirov, P.I. Stoev, G.F.Tikhinskiy, M.I. Palatnik, M.B. Mileshkin, and E.I. Muzyka, ФММ [The Physics of Metals and Metallography]. **57**(2), 1037 (1984). (in Russian).
[31] E.D. Tabachnikova, V.Z. Bengus, A.V. Podolskiy, S.N. Smirnov, and R.Z.Valiev, Кристаллография [Crystallography]. **54**, 1119 (2009). (in Russian).
[32] T.P. Cherniayeva, A.I. Stukalov, and V.M. Gritsyna, ВАНТ [Problems of Atomic Science and Technology. Section: Vacuum, Pure Materials and Superconductors]. **1**, 96 (2002).
[33] M.M. Myshliayev, S.Yu. Mironov, Физика твердого тела [Solid State Physics]. **44**(4), 711 (2002). (in Russian).
[34] Yu.P. Sharkeev, I.A. Kurzina, I.A. Bozhko, and A.Yu. Eroshenko, in: *10-th International Conference on Modification of Materials with Particle Beams and Plasma Flows, Oral Session: Beam and Plasma Nanoscience and Nanotechnology*, (Tomsk, Russia, 2010), pp. 705-708. (in Russian).
[35] A.A. Chabanets, in: *XVII Международная научно-практическая конференция «Современные техника и технологии», Секция 6: Материаловедение [XVII International Scientific and Commercial Conference "Modern Engineering @ Technologies". Section 6: Materials Science]* (Tomsk, Russia, 2012), pp. 261-262. (in Russian).
[36] I.A. Kurzina, I.A. Bozhko, M.P. Kalashnikov et. al., Материаловедение [Materials Science]. **5**, 48 (2010). (in Russian).
[37] V.A. Greshnikov, Yu.V. Drobot, *Акустическая эмиссия. Применение для испытаний материалов и изделий [Acoustic Emission: Application for Materials and Products Testing]*. (Mashinostroyeniye, Moscow, 1974), p. 368. (in Russian).
[38] P.I. Stoev, I.I. Papirov, Металлофизика [Physics of Metals]. **XIII** (10), 28 (1991). (in Russian).
[39] M.A. Meyers, A. Mishra, and D.J. Benson, Progress in Materials Science. **51**, 427 (2006).

ВПЛИВ СТРУКТУРНОГО СТАНУ НА МЕХАНІЧНІ ВЛАСТИВОСТІ ТА АКУСТИЧНУ ЕМІСІЮ ВИСОКОЧИСТОГО ТИТАНУ ЗА РІЗНИХ ВИДІВ ДЕФОРМАЦІЇ

К.В. Кутній, І.П. Кісляк, О.С. Кальченко, П.І. Стоєв, М.А. Тихоновський, П.О. Хаймович
Національний науковий центр «Харківський фізико-технічний інститут»
вул. Академічна 1, 61108, м. Харків, Україна

Представлені результати дослідження механічних властивостей високочистого титану з розмірами зерен від десятків нанометрів до кількох мікрометрів за одноосного розтягнення, одноосного стискання і мікроіндентування. Різні структурні стани в високочистому титані були сформовані шляхом інтенсивної пластичної деформації за схемою «осаджування-видавлювання-волочіння» в поєднанні з відпалами при температурах 250-550ºС і квазігідроекструзією при кімнатній температурі та температурі рідкого азоту. Визначено значення меж плинності і величини мікротвердості для зразків високочистого титану з різним розміром зерна. Показано, що поєднання інтенсивної пластичної деформації та кріогенної квазігідроекструзії дозволило створити високочистий нанокристалічний титан з високими механічними властивостями. Дані експериментів проаналізовані щодо виконання співвідношення Хола-Петча та розбіжностей величин меж плинності при стисканні та розтягненні (S-D ефект). Показано задовільне виконання співвідношення Хола-Петча для високочистого титану

в усій області досліджених значень розміру зерна і встановлено помітне розходження у величинах меж плинності на стиснення і розтягнення. Визначено значення коефіцієнтів в рівнянні Хола-Петча для деформації розтягненням, стисненням і для мікроіндентування. Ці коефіцієнти помітно нижче відповідних значень для технічних сортів титану, тобто в високочистому титані границі зерен є слабшими бар'єрами для рухомих дислокацій, ніж в технічному титані, у якого границі збагачені домішками. З'ясовані особливості емісії акустичних хвиль за стискування зразків, що мають різний структурний стан. Зроблено висновок, що деформація титану в усіх досліджених структурних станах відбувається шляхом дислокаційного ковзання.

КЛЮЧОВІ СЛОВА: високочистий титан, наноструктура, стискання та розтягнення, співвідношення Хола-Петча, акустична емісія

ВЛИЯНИЕ СТРУКТУРНОГО СОСТОЯНИЯ НА МЕХАНИЧЕСКИЕ СВОЙСТВА И АКУСТИЧЕСКУЮ ЭМИССИЮ ВЫСОКОЧИСТОГО ТИТАНА ПРИ РАЗЛИЧНЫХ ВИДАХ ДЕФОРМАЦИИ

К.В. Кутний, И.Ф. Кисляк, А.С. Кальченко, П.И. Стоев, М.А. Тихоновский, П.А. Хаймович

Национальный научный центр «Харьковский физико-технический институт»

ул. Академическая 1, 61108, г. Харьков, Украина

Представлены результаты исследования механических свойств высокочистого титана с размерами зерен от десятков нанометров до нескольких микрометров при одноосном растяжении, одноосном сжатии и микроиндентировании. Различные структурные состояния в высокочистом титане были сформированы путем интенсивной пластической деформации по схеме «осадка−выдавливание−волочение» в сочетании с отжигами при температурах 250–550ºС и квазигидроэкструзией при комнатной температуре и температуре жидкого азота. Определены значения пределов текучести и величины микротвердости для образцов высокочистого титана с различным размером зерна. Показано, что сочетание интенсивной пластической деформации с криогенной квазигидроэкструзией позволило создать высокочистый нанокристаллический титан с высокими механическими свойствами. Данные экспериментов проанализированы на предмет выполнения соотношения Холла-Петча и несовпадения величин пределов текучести при сжатии и растяжении (S-D эффект). Показано удовлетворительное выполнение соотношения Холла-Петча для высокочистого титана во всей области исследованных значений размера зерна и установлено заметное различие в величинах пределов текучести на сжатие и растяжение. Определены значения коэффициентов в уравнении Холла–Петча для деформации растяжением, сжатием и для микроиндентирования. Эти коэффициенты заметно ниже соответствующих значений для технических сортов титана, т.е. в высокочистом титане границы зерен являются более слабыми барьерами для движущихся дислокаций, чем в техническом титане, у которого границы обогащенные примесями. Определены особенности эмиссии акустических волн при сжатии образцов, имеющих различное структурное состояние. Сделан вывод о том, что деформация титана во всех исследованных структурных состояниях осуществляется дислокационным скольжением.

КЛЮЧЕВЫЕ СЛОВА: высокочистый титан, наноструктура, сжатие и растяжение, соотношение Холла-Петча, акустическая эмиссия

EAST EUROPEAN JOURNAL OF PHYSICS
East Eur. J. Phys. **3**. 38-45 (2019) DOI:10.26565/2312-4334-2019-3-05

PACS: 28.41.Qb, 81.40.Ef, 61.10.Nz, 61.72.Hh

ON STRUCTURAL ASPECTS OF TEXTURE CHANGES DURING ROLLING OF Zr-2.5%Nb ALLOY

Victor Grytsyna[1], Dmitry Malykhin[1]*, Tetiana Yurkova[1], Kostiantyn Kovtun[3], Tetiana Chernyayeva[1], Gennadiy Kovtun[1,2], Iryna Tantsura[1], Victor Voyevodin[1]

[1] *NSC "Kharkiv Institute of Physics & Technology" NASU, Kharkiv, 61108, st. Akademicheskaya 1, Ukraine*
[2] *V.N. Karazin Kharkiv National University, Kharkiv, 61022, Svobody Sq. 4, Ukraine.*
[3] *Public Enterprise «NTC «Beryllium», NASU, Kharkiv, 61108, st. Akademicheskaya 1, Ukraine*
**E-mail: dmitr.malykhin@gmail.com*

Received July 15, 2019; revised August 7, 2019; accepted August 27, 2019

Using X-ray structural analysis, features of changes in characteristics of crystallographic texture during cold working of Zr-2.5%Nb alloy plates by longitudinal and cross rolling has been investigated. To make original plates, longitudinal fragments and rings of ∅15.0×1.5 mm² tube annealed at 580 °C were used. The plates were rolled at room temperature to the degrees in the range from 6 to 56% with 5…7% per pass and the rate of 5...10s^{-1}. Using the method of inverse pole figures with measuring by the Bragg-Brentano optical scheme, densities of reflections along normal to plane of the plates (pole densities) was determined. Based on this, distributions of orientations of *c*-axes of hcp lattice of the material have been analyzed. Local features of the distributions, which were attributed to signs of twinning effects in texture changes in the alloy, are revealed. At subsequent analysis, an effect of strain non-uniformity associated with prehistory of the plates was taken into account. It is established that the second stage of (moderate) changes in Kearns textural coefficient of the plates with the deformation degrees differs from the initial stage of accelerated changes by activation of compression twins. By the method of tilt scanning (of rocking curves) around the Bragg-Brentano position at registration of (0004) reflection intensities, changes in orientation distributions of *c*-axes in longitudinal and cross section of the plates for both parties were investigated. It is noted that the main textural changes in process of deformation of the plates occur in the cross-sectional plane of the original tube and are most expressed on the cross-rolling plates. The doublet in the distributions of *c*-axes, characteristic for rolling texture of hcp metals of titanium subgroup, was noted just at the second stage of the texture changes in the material. Its directionality is mainly associated with the plane of cross-section of the original tube. A connection is revealed between features of the pole density distributions and expression degree of the textural doublet on the rocking curves. According to the results obtained and analysis of other publications, twinning nature of the textural doublet was confirmed and a schematic sequence of its formation was proposed with participation of compression twins of $\{11\bar{2}2\}\langle\bar{1}\bar{1}23\rangle$ system and tensile twins of $\{10\bar{1}2\}\langle\bar{1}011\rangle$ and $\{11\bar{2}1\}\langle\bar{1}\bar{1}26\rangle$ systems.

KEYWORDS: zirconium alloys, rolling, XRD, texture, twinning.

This work is a continuation of studies of regularities and mechanisms of texture changes during plastic deformation of the Zr-2.5%Nb alloy widely used in nuclear industry [1]. Texture of products with hcp lattice of material, in particular, of zirconium alloys, is a factor of anisotropy of the materials and many of its properties. They are mechanical, electrical and thermal characteristics, etc. Effect of radiation growth of tubes made of zirconium alloys in the reactor core is closely related to crystallographic texture.

A special feature of the work is a study of material with a lowered initial texture and, herewith, the use the method of inverse pole figures (IPFs) with sample scanning by the usual diffractometric scheme. From the textural method of direct pole figures, widely used recently, this method differs by its significant simplicity. In addition, this method has advantages in accuracy of determining of certain texture parameters of the materials directly related to the listed characteristics of products. All this as a whole gives the possibility to study quantitative regularities of changes in texture characteristics depending on physical and technological factors.

The main such parameter, which was proposed for studies of samples of zirconium alloys, is Kearns textural coefficient [2]. This is a characteristic expressing degree of directionality of *c*-axes of crystalline hcp cell of grains in polycrystalline material along a given geometric direction in a product:

$$f_k = \left\langle \cos^2 \alpha_{ki} \right\rangle, \tag{1}$$

where α_{ki} are the angles between a given direction (k) and orientations (i) of *c*-axes.

Most of the listed product characteristics, dependent on crystallographic anisotropy of zirconium alloys, are associated with the f coefficient linear dependence. In particular, the textural coefficient of radiation growth of zirconium elements of reactor core and fuel assembly components is unambiguously connected with it: $G = 1 - 3f$ [3].

In the previous work [4], studies were carried out on regularities of changes in the textural coefficient depending on degrees of deformation by longitudinal and cross rolling of plates made from fragments of a tube of this alloy. Existence of two stages was revealed: the initial stage of an increased rate of growth of the coefficient and the subsequent moderate stage. By analyzing dynamic of *c*-axes distributions with deformation degrees of the alloy, the leading role of twinning in the changes on the initial stage of deformation was established.

The purpose of this work is to continue the studies of role of structural mechanisms in regularities of changes in crystallographic texture of this alloy at longitudinal and cross rolling. This is envisaged by implementation additional studies with detailed analysis of texture of samples made and investigated at the previous stage of work. In this regard, we use additional techniques and approaches to X-ray analysis of texture.

EXPERIMENTAL

On material [4]**.** For making samples of Zr-2.5%Nb alloy, the original material was a tube ∅15.0×1,5 mm² of RBMK reactor fuel assemblies with final annealing at 580 °C for 3 h.

Samples in the form of plates were made of longitudinal fragments and rings of the tube, 40×20 mm² and 20×10 mm² of size, respectively. The plates were annealed at 580 °C for 24 h in $1.5 \cdot 10^{-3}$ Pa vacuum, and then etched up to 65 μm.

The plates were rolled at room temperature from 6 to 55% on the whole with a step of 5...7% per pass and a speed of 5...$10s^{-1}$ without intermediate annealing. According to the nature of texture of the original tube [4], the rolling was considered as an analogue of longitudinal (for plates of longitudinal fragments) and cross rolling (for plates of rings).

Methods. The IPF method with the principle of calculating the textural coefficient is described in [4].

At this stage, as one of the research approach, we analyzed the distribution of orientation of *c*-axes along the normal to surface of the samples – density of *c*-axes distribution by the angle of their deviation from the normal direction (ND), regardless of other coordinate angles. As an analogue of such a distribution, the pole density values ($P_{(hkil)}$) were used. In this case, only pyramidal planes of the first kind – $(h0\bar{h}l)$ – were taken into account. Such a group represents the densest sequence of $P_{(hkil)}$ values, where the result of the changes may be most noticeable.

As a second additional method of analysis, the technique of tilt scanning of plates (rocking curve measurements) was used. This is aimed at analyzing *c*-axes distribution within the planes of orthogonal plate section. The distributions of (0004) X-ray intensities were analyzed when the shooting direction deviated from the normal to the plate plane (ND) towards the rolling direction (RD) and towards the transverse direction (TD) associated with the rolling geometry.

To eliminate the effects associated with misalignment of the optimal X-ray optic scheme, a wide receiving slit of the counter was used, and the intensity measured was averaged over two opposite tilts.

RESULTS END DISCUSSION

Graphical regularities

Fig. 1,2 show the pole density distribution ($P_{(hkil)}$; *c*-axes distributions) for $(h0\bar{h}l)$ reflections in the ND direction of plates, including (0002) and $(10\bar{1}0)$ reflections. Distributions are presented in cos²α coordinates for the initial and deformed state of samples after longitudinal (Fig. 1) and cross rolling (Fig. 2). The graphs, presented in common-logarithmic scale, are located with deformation degrees above each other through the single-unit interval of the ordinate grid.

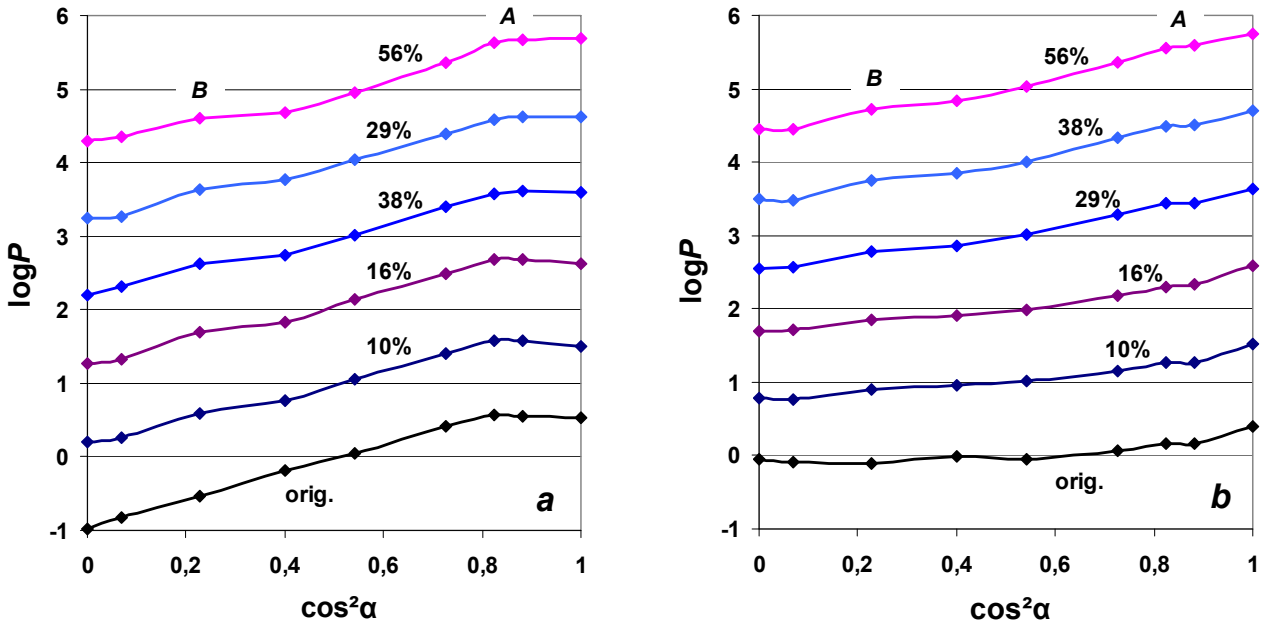

Fig. 1. *C*-axes distributions at $(h0\bar{h}l)$-reflecting positions of grains in ND direction of longitudinally-rolled Zr-2.5%Nb plates on texture measurements on the inside (a) and outside (b) of original tube.

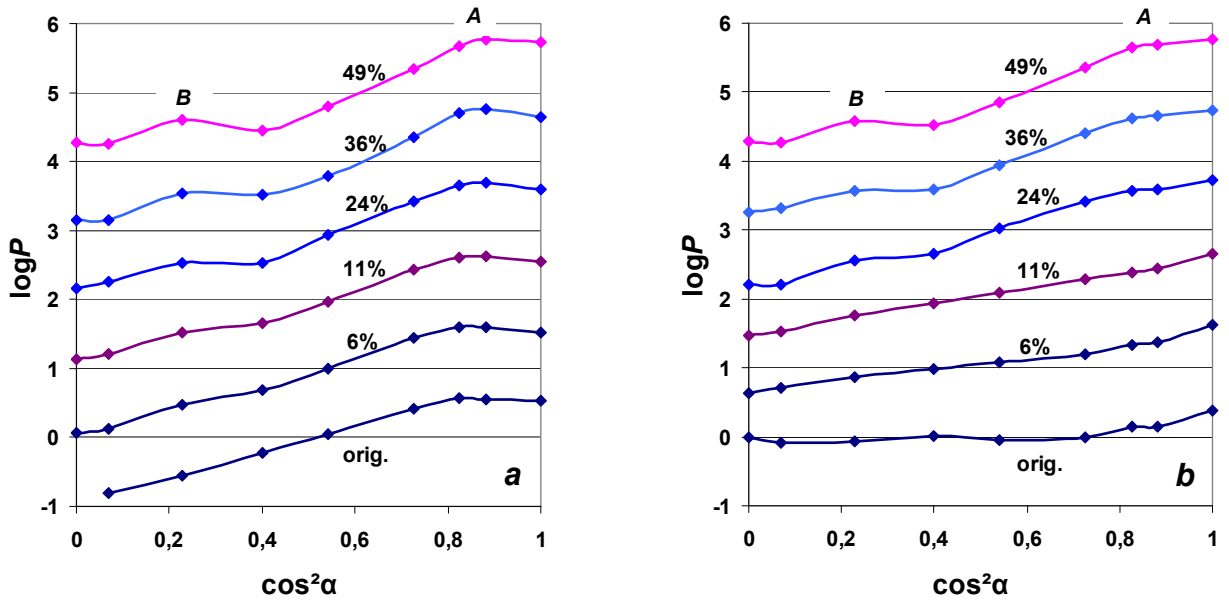

Fig. 2. *C*-axes distributions at $(h0\bar{h}l)$-reflecting positions of grains in ND direction of cross-rolled Zr-2.5%Nb plates in presentation of texture data measured on the inside (a) and outside (b) of original tube.

The most characteristic regularities should be noted on the data obtained from the surface of the plates on the inside of the original tube (Fig. 1a, 2a). The main course of the graphs in logarithmic representation of data is linear and uniform for all states and for each of two batches. This corresponds to the second stage of the change of the textural coefficient (*f*) with the plate deformation – to the stage of moderate changes [4]. These data are represented by graphs with light circles in Fig. 3a,b. They indicate that for the texture of the inner surface areas of the tube, its blanks, it is sufficient to reach the second stage by straightening the blanks, which for these areas is similar to rolling by 10% regardless of the subsequent preliminary annealing the samples in the α-phase.

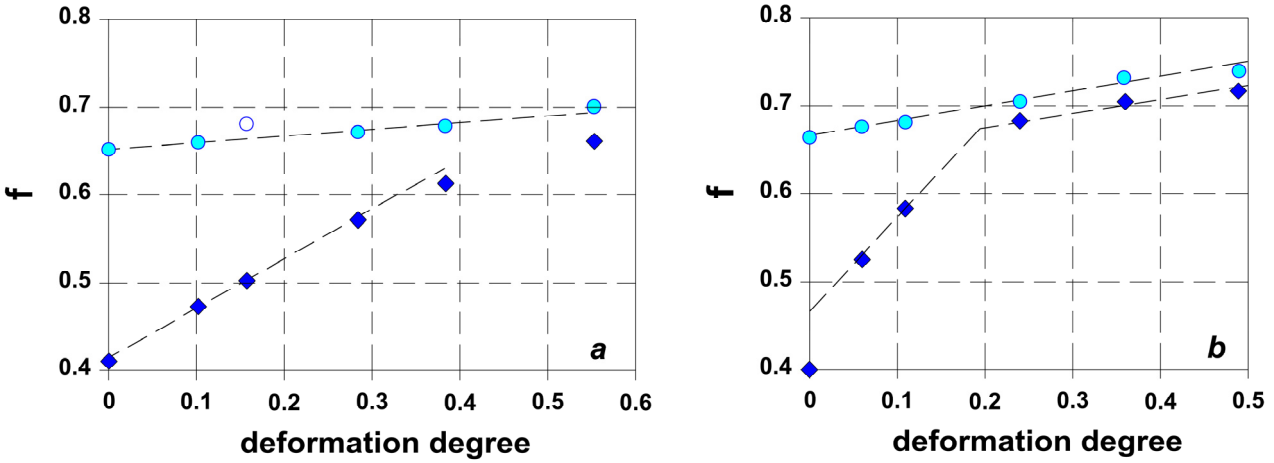

Fig. 3. Change in textural coefficient with degrees of deformation of plates during longitudinal (a) and cross rolling (b) [4]. Data from plate surfaces on the outside (◆) and inside (○) of original tube.

The second characteristic feature of Fig. 2 and, especially, Fig. 1 is the existence of an upper limit of linearity of graphs (*A* position; α = 20...25°) and a narrow area in *B* position (α = 55...65°) with exceeding its linear changes, which refers to neighborhood of the $(10\bar{1}1)$ reflection line. According to Fig. 3a,b, the evolution of *B* position and the formation of *A* position as a maximum of the distribution are clearly observed in the second stage of texture changes with deformation. It is also meant that at the cross rolling of plates, for their near-surface areas – on the outside of the original tube, – the second stage begins approximately from 20% deformation (Fig. 3b; black squares). At the same time, it is necessary to especially note the obvious connection between expression degree of *A* and *B* positions (Fig. 1,2).

Associated with the second stage for deformed medium of the material, the noted features which including the linearity of logarithmic graphs are similar to the results of such investigation of pure zirconium and hafnium [5].

Analysis of tilt scanning data

As noted above, in these studies another technique was used to analyze evolution of *c*-axes distributions in process of plate deformation.

Fig. 4 shows diagrams of tilt scanning (rocking curve measurements) of the original and deformed samples of both parties in (0004) reflection from the inner side of the original tube. Angular scanning was carried out in the plane of the transverse and longitudinal section of the samples (respectively, N-T and N-R scan) and represents *c*-axes angular distributions in these planes relative to ND. The graphs are located above each other by the single-unit interval of the ordinate grid. Scale parameters are identical for all fragments of the figure. The data, as noted above (Fig. 3), actually refer to the second stage of texture changes of the alloy with deformation.

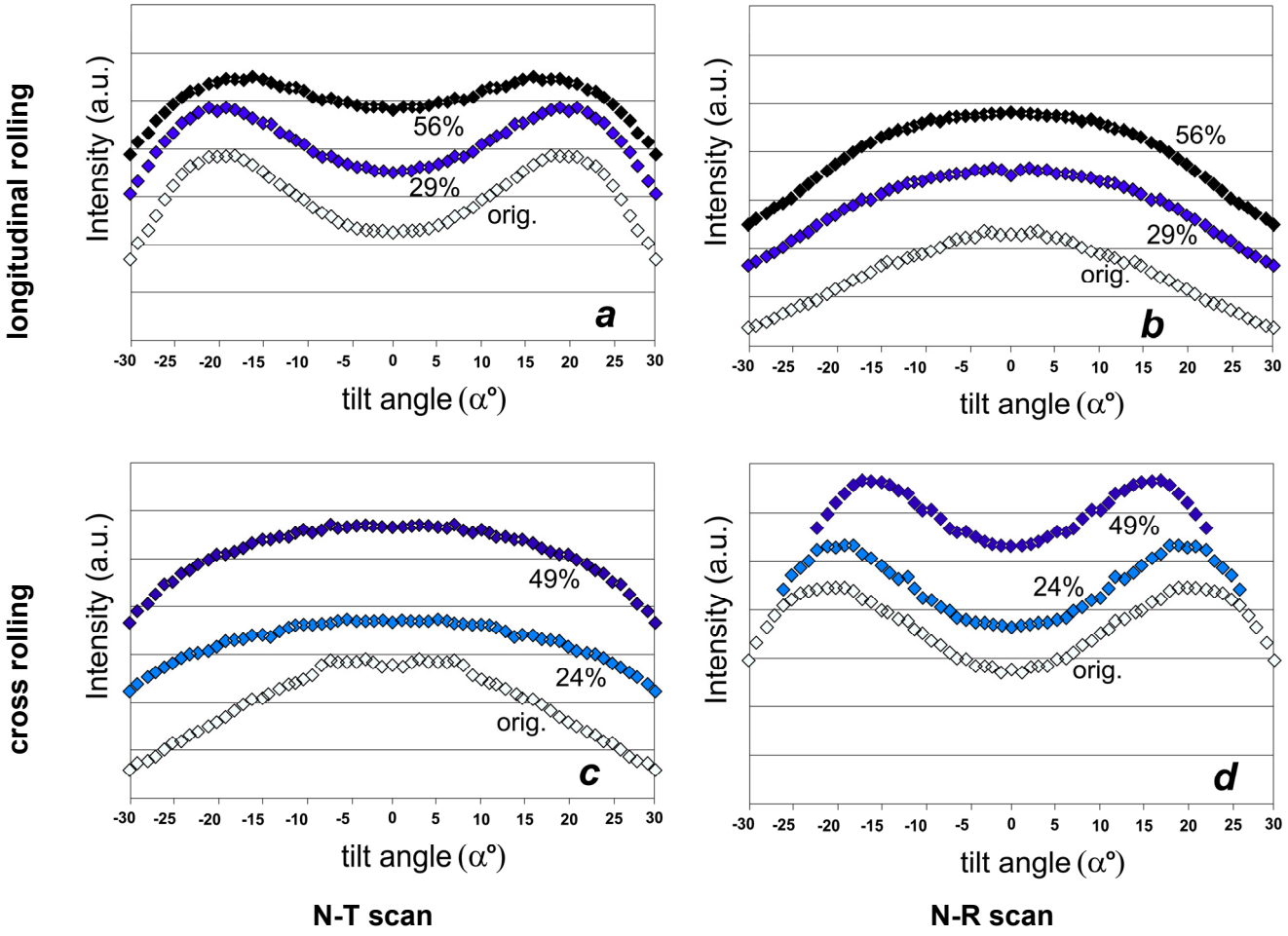

Fig. 4. Distributions of *c*-axes along cross (a, c) and longitudinal (b, d) sections of longitudinally- (a, b) and cross-rolled plates (c, d). Data from surfaces which corresponding to inner side of original tube; arbitrary units. Deformation degrees are indicated.

The double peak of the distributions (Fig. 4a,d) – a textural doublet with ±20...25° maxima deviations from ND – is unambiguously combined with the expression degree of the maximum of distributions in Fig. 1,2 (*A* position; α = 20...25°). Data on longitudinal rolling (Fig. 4a,b) represent evolution of the typical rolling texture of metals of the titanium subgroup with orientation of the doublet in the cross-sectional plane of the plates (N-T; perpendicular to RD). Data on cross rolling of the plates reflect an unusual situation with the direction of the doublet in the longitudinal section of the plates (perpendicular to TD; Fig. 4d), but a tendency to form such a doublet according to the typical scheme in the N-T plane also exists (Fig. 4c).

Fig. 5 presented in the same format, shows data of tilt scanning from the "outer" side of the plates. Fig. 5 actually reflects evolution of the textural features of Fig. 4, which should be considered characteristic of lower degrees of deformation, mainly for the initial stage of accelerated textural changes [4]. Here, this process shows some signs of instability, although this is practically not reflected in change regularity of the textural coefficient (Fig. 3). In the same time, these data confirm that the process of formation of the textural doublet occurs in the second stage. This follows, for example, from the scanning results for samples after their rolling with degrees above the order of 20%. This is most expressed after cross rolling, especially in the N-R scan (Fig. 5d).

In general, the results indicate that the most characteristic textural changes occur along the cross-sectional plane of the original tube and at cross rolling of plates.

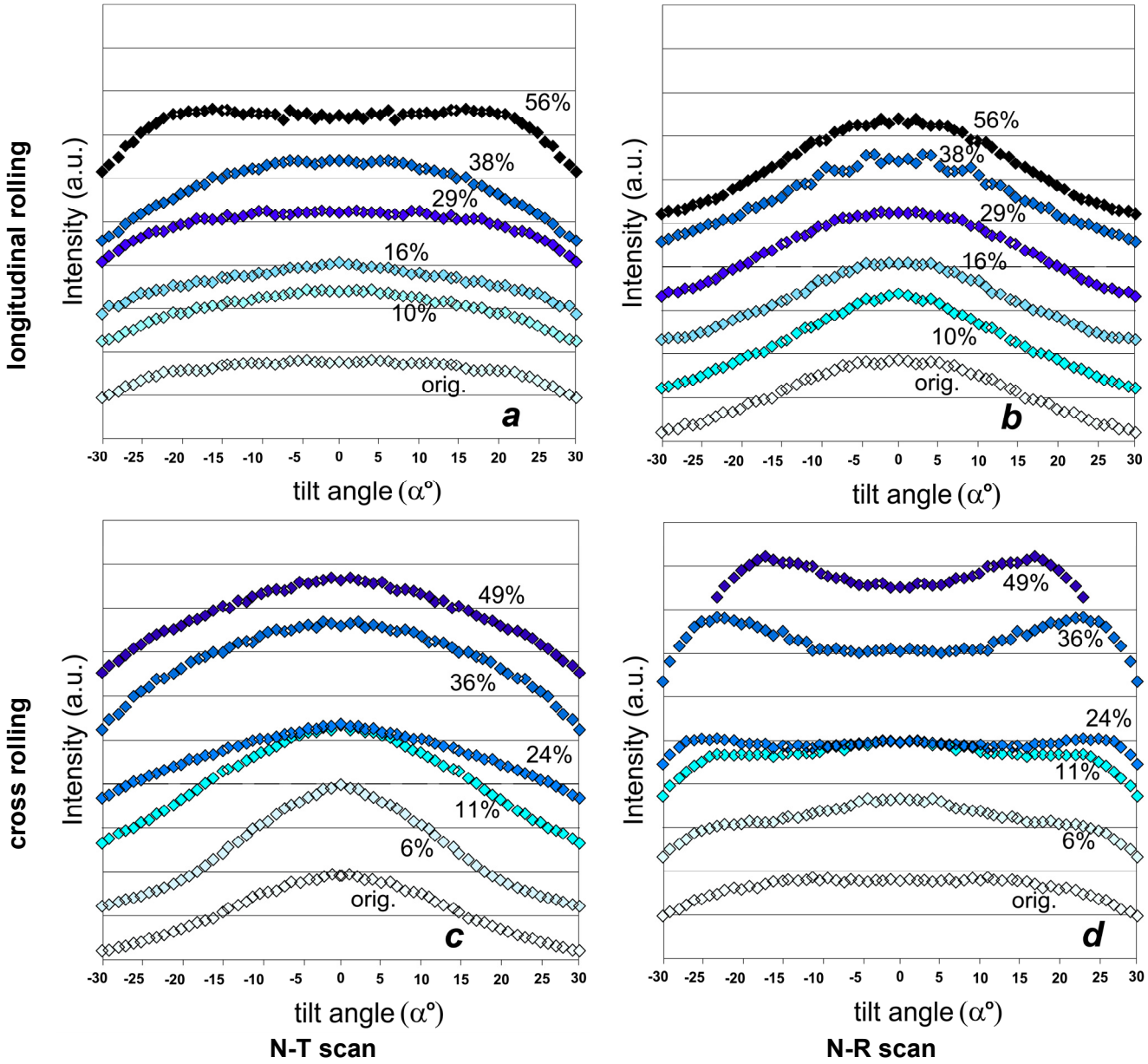

Fig. 5. Distributions of *c*-axes along cross (a, c) and longitudinal (b, d) sections of longitudinally- (a, b) and cross-rolled plates (c, d). Data from surfaces which corresponding to outer side of original tube; arbitrary units. Deformation degrees are indicated.

On twinning schemes of forming the texture at longitudinal and cross rolling of alloy

As was established [4], the reason of the accelerated rate of textural changes at the initial deformation stage of the alloy is activity of tensile twins of $\{10\bar{1}2\}[\bar{1}011]$ system. This system rotates *c*-axes of grains by 85° [6]. The end of the initial stage was associated with significant reduction of the twinning substrate – a fraction of grains with a crystallographic orientation favorable for their subsequent twinning by this system.

From simple considerations, a decrease in activity of this twinning system at the end of the initial stage is further compensated by activity of other deformation systems. Thus, appearance of irregularity of the distributions (Fig. 1,2) in *B* position (α = 55...65°), mainly in the second stage, can be associated with activity of compression twins systems. These systems rotate *c*-axes through an angle of 60 ± 5° [6]. $\{10\bar{1}1\}$ reflection in *B* position can be caused either by rotation of the axes from the ND direction by $\{\bar{1}011\}[10\bar{1}2]$ twin system or by rotation of the grains in this position around its own *c*-axes in result of action of prismatic slip systems.

In the non-ambiguity of the combination of *A* (α = 20...25°) and *B* positions (Fig. 1,2), what was noted above, a reason can be seen. So, if the real *A* and *B* positions were oriented in opposite directions from the ND normal (Fig. 6), then Δα interval between them would be 85°. This could be a sign of axes rotation from *B* position (B_0, Fig. 6) to *A* position directly by $\{10\bar{1}2\}[\bar{1}011]$ tensile twins system. In this case, *A* position would be at an angle 28°.

Since *A* position is associated with the textural doublet, such a scheme would represent the N-T plane for longitudinal rolling and the N-R plane for cross rolling of the plates as the plane of turns. B_0 (Fig. 6) displays *B* position in

these planes. However, as a result of additional measurements of the plates in the RD and TD directions, signs of B_0 position were not detected. In particular, the absence of such signs was noted from results of measurements of cross-rolled plates in RD direction (rolling up to 49%, Fig. 7; area of $\cos^2\alpha = 0.75\ldots0.85$). In part, this was due to the extremely low ability of B_0 position to appear in principle in RD and TD. This does not give grounds either to confirm or to disprove the ability of the sequence of $\{10\bar{1}1\}[\bar{1}012]$ and $\{10\bar{1}2\}[\bar{1}011]$ twinning systems to form *A* position.

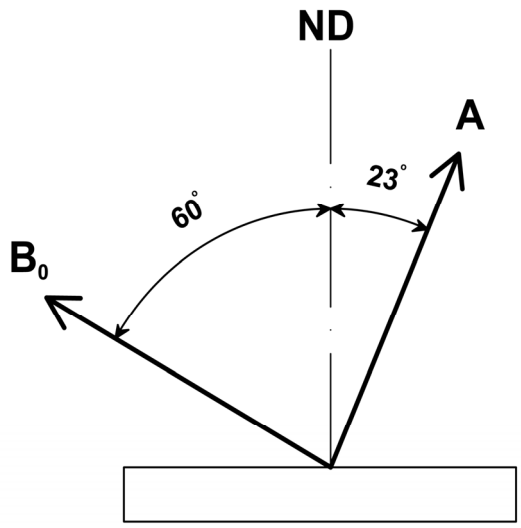

Fig. 6. Variant of location of *A* and *B* positions (Fig. 2.3). View in plane of longitudinal section of cross-rolled plates (N-R).

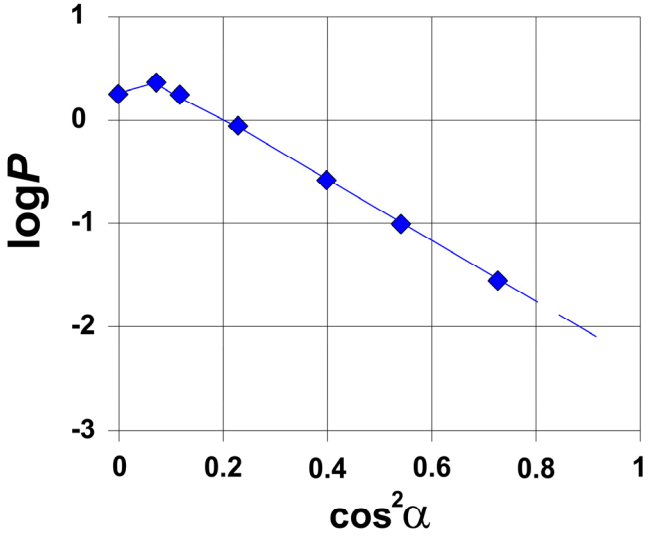

Fig. 7. Distribution of *c*-axes deviations from cross-rolling direction for $(h0\bar{h}l)$-reflecting positions. Common-logarithmic scale.

Thus, *B* position remains only a sign of activity of the main systems of compression twins [6]. $\{11\bar{2}2\}[\bar{1}\bar{1}23]$ system is the most active of these systems [7-9]. Its twins rotate *c*-axes of grains from the ND limits (measurement direction) to the angular position *B*. However, these grains take another foreshortening and are oriented in the ND direction by the normal of planes of the $\{hh\overline{2h}l\}$ group corresponding to the "pyramid" of the second kind. Actually, that plane does not fall within the X-ray reflections area and does not appear in *B* positions, although it gives orientation of *c*-axes in limits of this position ($\alpha = 64.2°$) [6].

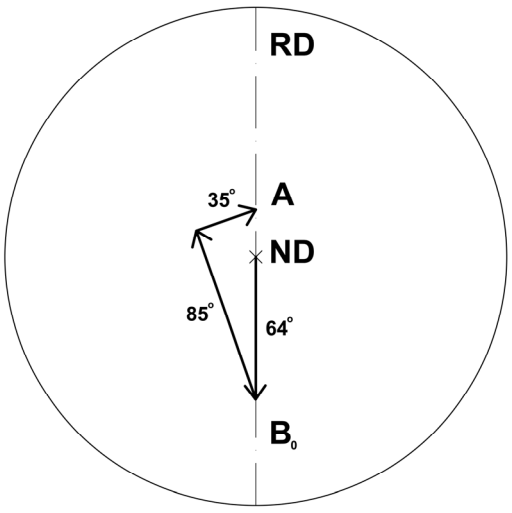

Fig. 8. Scheme of forming textural doublet by sequence of *c*-axis rotations. Cross-rolled samples.

As noted in [7–9], at deformation of zirconium and its alloys, such compression twins (of $\{11\bar{2}2\}[\bar{1}\bar{1}23]$ system) initiate $\{10\bar{1}2\}[\bar{1}011]$ system – the main system of tensile twins – as a second generation. However, their $\{1120\}$-plane of turns (of twinning shears) deviates by 30° from the $\{1100\}$-plane of the primary turns. It was noted [8] that $\{11\bar{2}1\}[\bar{1}\bar{1}26]$ system of tensile twins is accompanied with activity of $\{10\bar{1}2\}[\bar{1}011]$ secondary twins. According to analysis of Fig. 4,5, and to formal concepts, it remains to conclude that these twins (first ones), participate in rotations the axes at an angle of 34.8° [6], transfer them, from the plane of the previous turns, to *A* position limits

(30°-34.8°; Fig. 8). The resulting rotation from *B* position reaches an angle of 86°, and the final orientation (*A* position) is expected at an angle of 22°.

Such a scheme of formation of the textural doublet is most consistent with Fig. 4a,d and 5a,d. The probable traces of twinning by the previous scheme can be observed only at the beginning of the second textural stage in the cross rolling process (Fig. 5d; 24% deformation). In [7–9], no such signs were found.

On the example of pure zirconium, a noticeable slip contribution to texture changes with formation of the textural doublet is not expected [8].

This conclusion is done in relation to research data, mainly of cross-rolling samples. However, such conclusions formally apply to longitudinal rolling of this alloy.

SUMMARY

X-ray studies of effect of longitudinal and cross rolling on features of texture of plates made from blanks of the fuel assembly central tube of Zr-2.5%Nb alloy used in RBMK reactor were carried out on the basis of the tilt scanning technique (rocking curve measurements) and an analysis of pole density distributions. As a result, the following has been established:

Most characteristic texture changes with longitudinal and cross rolling of plates up to 50% occur within the cross-sectional plane of original tube and at cross rolling of plates.

In contrast to the initial stage of an increased rate of changes in Kearns textural coefficient, the subsequent stage of moderate changes is characterized by activity of compression twins and by process of formation of the textural doublet in distributions of *c*-axes of grains, that is more expressive along the cross-section plane of tube and at cross rolling of plates.

Probability of twinning schemes of formation of the textural doublet in process of alloy rolling was analyzed. The main schematic sequence of it is proposed:

– twinning by $\{11\bar{2}2\}[\bar{1}\bar{1}23]$ system of compression twins rotating *c*-axes by 64° from the normal to plate plane within the main plane of turns (cross section of the tube);

– twinning by $\{10\bar{1}2\}[\bar{1}011]$ system of tensile twins rotating these *c*-axes at an angle of 85° in the nearly opposite direction;

– participation of tensile twins of $\{11\bar{2}1\}[\bar{1}\bar{1}26]$ system with rotations these *c*-axes to the main plane of turns (cross section of the tube).

ORCID IDs

Victor Grytsyna https://orcid.org/0000-0003-4341-007X, **Dmitry Malykhin** https://orcid.org/0000-0003-0259-0211, **Tetiana Yurkova** https://orcid.org/0000-0003-1264-640X, **Kostiantyn Kovtun** https://orcid.org/0000-0002-0524-5053, **Gennadiy Kovtun** https://orcid.org/0000-0003-4242-7697

REFERENCES

[1] A. Nikulina, S. Shishov, B. Cox, F. Garzarolli and P. Rudling, Manufacturing of Zr-Nb Alloys, ZIRAT-11, *Special Topic Report. ANT International*, (Skultuna, Sweden, 2006), pp.45p.

[2] J.J. Kearns, *Thermal expansion and preferred orientation in Zircaloy, WAPD-TM-472*, (Westinghouse Electric Corporation, Pittsburg, USA, 1965).

[3] P.A. Tempest, J. Nucl. Mater. **92**(2-3) (1980) pp.191-200, DOI: 10.1016/0022-3115(80)90102-6

[4] V. Grytsyna, D. Malykhin, T. Yurkova, K. Kovtun, T. Chernyayeva, G. Kovtun, V. Kornyeyeva, O. Slabospitskaya, I. Tantsura and V. Voyevodin, East-European Journal of Physics, **2,** 39-45 (2019).

[5] G.P. Kovtun, K.V. Kovtun, D.G. Malykhin, T.S. Yurkova and T.Yu. Rudycheva, East-European Journal of Physics, **4**(3), 36-42 (2017).

[6] E. Tenckhoff, J. of ASTM International, **2**(4), 1-26 (2005), DOI: 10.1520/JAI12945.

[7] M. Zhang, B.F. Luan, Z.I. Song, R.I. Xin, K.I. Murty and Q. Liu, Scripta Materialia, **122**, 77-81 (2016).

[8] Bai-feng Luan, Qing Ye, Jian-wei Chen, Hong-bing Yu, Dong-li Zhou and Yun-chang Xin, Trans. Nonferr. Met. Soc. China **23**(10), 2890-2895 (2013), in: https://www.sciencedirect.com/science/article/abs/pii/S1003632613628113

[9] R.J. McCabe, G. Proust, E.K. Cerreta and A. Misra, Int. J. of Plast. **25**(3), 454-472 (2009), DOI: 10.1016/j.ijplas.2008.03.010

ПРО СТРУКТУРНІ АСПЕКТИ ТЕКСТУРНИХ ЗМІН ПРИ ПРОКАТЦІ СПЛАВУ Zr-2.5%Nb

Грицина В.М.[1], Малихін Д.Г.[1], Юркова Т.С.[1], Ковтун К.В.[3], Черняєва Т.П.[1], Ковтун Г.П.[1,2], Танцюра І.Г.[1], Воєводін В.М.[1]

[1]ННЦ «Харківський фізико-технічний інститут» НАНУ
Україна, 61108, г. Харків, ул. Академічна 1
[2]Харківский національний університет ім. В.Н. Каразіна
Україна, 61022, м. Харків, майдан Свободи, 4
[3]ДП «НТЦ «Берилій» НАНУ
Україна, 61108, м. Харків, вул. Академічна 1

Методом рентгеноструктурного аналізу досліджено особливості змін характеристик кристалографічної текстури при холодній деформації пластин зі сплаву Zr-2,5% Nb поздовжньої і поперечної прокатки. Матеріалом для виготовлення вихідних пластин були поздовжні фрагменти і кільця труби ∅15,0×1,5 мм², відпалені при 580 °С. Прокатка пластин здійснювалася

при кімнатній температурі в інтервалі від 6 до 56% у ступінчастому режимі з кроком 5…7% і швидкістю 5...10 сек$^{-1}$. На основі методу зворотних полюсних фігур з дифрактометрічною зйомкою за оптичною схемою Брега-Брентано визначалась густина відбиття вздовж нормалі до площини пластин сплаву (щільність полюсів). За цими даними проведено аналіз розподілу орієнтацій кристалографічних осей «с» ГЩУ-решітки матеріалу. Виявлено локальні особливості розподілів, які було віднесено до ознак прояви двійникування в змінах текстури пластин. При подальшому аналізі було враховано ефект неоднорідності деформації, пов'язаний з передісторією пластин. Встановлено, що друга стадія (помірних) змін текстурного параметру Кернса зі ступенем деформації пластин відрізняється від початкової стадії прискорених змін активізацією двійників стиснення. Методом зйомок кривих хитання з регістрацією інтенсивностей відбиття (0004) навколо центральної позиції досліджено зміни розподілів орієнтації осей «*c*» в поздовжньому і поперечному перетині пластин сплаву обох партій. Відзначено, що основні текстурні зміни в процесі деформації пластин здійснюються в площині поперечного перетину вихідної труби і найбільш виражені на пластинах поперечної прокатки. Дублет в розподілі осей «*c*», що характерний для текстури прокатки ГЩУ-металів титанової підгрупи, відзначено на другій стадії текстурних змін у матеріалі, зокрема – з його спрямованістю уздовж площини поперечного перетину вихідної труби. Виявлено зв'язок особливостей розподілів щільності полюсів зі ступенем вираженості текстурного дублету на кривих хитання. Згідно з отриманими результатами та аналізом інших публікацій підтверджено двійникову природу текстурного дублету і запропоновано схематичну послідовність його формування за участю двійників стиснення системи $\{11\bar{2}2\}\langle\bar{1}\bar{1}23\rangle$ і двійників розтягування систем $\{10\bar{1}2\}\langle\bar{1}011\rangle$ та $\{11\bar{2}1\}\langle\bar{1}\bar{1}26\rangle$.

КЛЮЧОВІ СЛОВА: сплави цирконію, прокатка, рентгенографія, текстура, двійникування.

О СТРУКТУРНЫХ АСПЕКТАХ ТЕКСТУРНЫХ ИЗМЕНЕНИЙ ПРИ ПРОКАТКЕ СПЛАВА Zr-2.5%Nb

Грицина В.М.[1], **Малыхин Д.Г.**[1], **Юркова Т.С.**[1], **Ковтун К.В.**[3], **Черняева Т.П.**[1], **Ковтун Г.П.**[1,2], **Танцюра И.Г.**[1], **Воеводин В.Н.**[1]

[1]*ННЦ «Харьковский физико-технический институт» НАНУ*
Украина, 61108, г. Харьков, ул. Академическая 1
[2]*Харьковский национальный университет им. В.Н. Каразина*
Украина, 61022, г. Харьков, пл. Свободы, 4
[3]*ГП «НТЦ «Бериллий» НАНУ*
Украина, 61108, г. Харьков, ул. Академическая 1

Методом рентгеноструктурного анализа исследованы особенности изменений характеристик кристаллографической текстуры при холодной деформации пластин из сплава Zr-2,5%Nb продольной и поперечной прокаткой. Материалом для изготовления исходных пластин были продольные фрагменты и кольца трубы ∅15,0×1,5 мм², отожжённые при 580 °С. Прокатка пластин осуществлялась при комнатной температуре в интервале от 6 до 56% в ступенчатом режиме с шагом 5…7% и со скоростью 5…10 сек$^{-1}$. На основе метода обратных полюсных фигур с дифрактометрической съёмкой по оптической схеме Брэгга-Брентано определялась плотность отражений вдоль нормали к плоскости пластин сплава (плотность полюсов). По этим данным проведен анализ распределения ориентаций кристаллографических осей «*c*» ГПУ-решётки материала. Выявлены локальные особенности распределений, которые были отнесены к признакам проявления двойникования в изменениях текстуры пластин. При последующем анализе учтён эффект неоднородности деформации, связанный с предысторией пластин. Установлено, что вторая стадия (умеренных) изменений текстурного параметра Кернса со степенью деформации пластин отличается от начальной стадии ускоренных изменений активизацией двойников сжатия. Методом съёмок кривых качания с регистрацией интенсивности отражения (0004) исследованы изменения распределений ориентации осей «*c*» в продольном и поперечном сечении пластин сплава для обеих партий. Отмечено, что основные текстурные изменения в процессе деформации пластин осуществляются в плоскости поперечного сечения исходной трубы и наиболее выражены на пластинах поперечной прокатки. Дублет в распределении осей «*c*», характерный для текстуры прокатки ГПУ-металлов титановой подгруппы, отмечен на второй стадии текстурных изменений в материале. Его направленность в основном связывается с плоскостью поперечного сечения исходной трубы. Выявлена связь особенностей распределений плотности полюсов со степенью выраженности текстурного дублета на кривых качания. Согласно полученным результатам и анализу других публикаций подтверждена двойниковая природа текстурного дублета и предложена схематическая последовательность его формирования с участием двойников сжатия системы $\{11\bar{2}2\}\langle\bar{1}\bar{1}23\rangle$ и двойников растяжения систем $\{10\bar{1}2\}\langle\bar{1}011\rangle$ та $\{11\bar{2}1\}\langle\bar{1}\bar{1}26\rangle$.

КЛЮЧЕВЫЕ СЛОВА: сплавы циркония, прокатка, рентгенография, текстура, двойникование.

EAST EUROPEAN JOURNAL OF PHYSICS
East Eur. J. Phys. **3**. 46-53 (2019) DOI:10.26565/2312-4334-2019-3-06

PACS: 03.65.Sq

ENERGY EXCHANGE BETWEEN THE FIELD AND THE ACTIVE MEDIUM OF THE WAVEGUIDE

Volodymyr Kuklin*, Eugen Poklonskiy
V.N. Karazin Kharkiv National University, Kharkiv, Ukraine
Svobody Sq. 4, Kharkiv, Ukraine, 61022
**E-mail: kuklinvm1@gmail.com*
Received July 2, 2019; revised August 2, 2019; accepted August 29, 2019

The work based on a semiclassical description, presents the results of studying the processes of absorption and radiation of a field in the form of a standing wave in a waveguide filled with a two-level active medium. Under conditions of spatial inhomogeneity of the field intensity, interference of quasi-periodic oscillations of population inversion occurs in different local regions of the waveguide. A quasiperiodic change in population inversion is determined by the Rabi frequency, which is known to be associated with the probability of induced radiation with a positive population inversion, or induced absorption with its negative value. Since the population inversion change is accompanied by absorption or emission of field quanta, this leads to the exchange of energy between the field and the active medium located in the waveguide. It is shown that the attenuation of a large-amplitude field to a waveguide filled with an unexcited active medium is nonlinear. In the developed mode, this process has the character of energy exchange between the field and the active medium. In this case, the wave attenuation is replaced by its growth, just as it happens in the well-known case of Landau kinetic damping. Competition of the processes of radiation and absorption leads to the fact that the nature of the oscillations (nutations) of the population inversion at different points of the waveguide space is different. The interference of nonsynchronous spatially localized oscillations of the population inversion in the volume of the waveguide leads to changes in the field amplitude. The paper also discusses the process of field excitation in a waveguide with a pre-inverted two-level active medium, taking into account external mechanisms for the absorption of wave energy. Consideration of these problems is important for understanding the processes of generation of induced radiation, which, as noted by C. Towns, is to a large extent coherent radiation.
KEYWORDS: absorption and radiation of the field, two-level active medium, Rabi frequency, interference of oscillations of population inversion.

The quasiclassical model of the interaction of the field and the active system, in particular, a system of dipoles with two energy levels, allowed consider these phenomena in the media [1-4]. This model combined a quantum-mechanical approach using a density matrix to describe a system of dipoles, and the classical field representation in limited volumes, particularly in waveguides. An important characteristic of the dynamics of a dipole system in the presence of an external electric field is the Rabi frequency, which determines the probabilities of induced emission or absorption of field quanta [1, 2] and describes the population inversion oscillations (nutation).

Previously, the focus was on the processes of relaxation and excitation of a quantum system in the external media [1-2], as well as modes of oscillation generation in unbounded media with nonlinearity, dispersion and finite temperature [3-4] (see also [5-9]). However, a consequence of the limitations of the system is the appearance of line spectra of oscillations and standing waves, which leads to a noticeable non-uniformity of the field intensity distribution. This can change the nature of the field interaction with the active medium placed in the waveguide, because in areas with different field intensities the Rabi frequency and, accordingly, the nature of the oscillatory behavior of the population inversion of the active substance will differ significantly.

Below we discuss the influence of the spatial inhomogeneity of the field on the nature of its interaction with the active medium. Let us consider the features of the absorption and excitation of a field in a waveguide filled with an active two-level medium. Let the field in the waveguide be a standing wave, and at each point in space, it changes only with time. We show that the interference of quasi-periodic changes in population inversion in different areas with the Rabi frequency, depending on the local field intensity in these areas, determines both the nature of the attenuation of a large amplitude wave and the nature of the field generation.

The aim of the article is to present the physical mechanism of attenuation of a large-amplitude wave in a waveguide filled with an active two-level medium, as well as to elucidate the nature of electromagnetic field excitation at finite levels of population inversion.

RABI FREQUENCY

If the waveguide is filled with an active substance, the semiclassical theory, which was actively discussed in particular in [2–4], describes the generation of oscillations. To simplify the description, we consider a one-dimensional model for disturbances of the electric field E , polarization P and population inversion μ that slowly varies with time, describing the excitation of electromagnetic oscillations in a two-level active medium, whose equations can be represented as

$$\frac{\partial^2 E}{\partial t^2} + \delta \frac{\partial E}{\partial t} - c^2 \frac{\partial^2 E}{\partial x^2} = -4\pi \frac{\partial^2 P}{\partial t^2}, \qquad (1)$$

$$\frac{\partial^2 P}{\partial t^2} + \omega^2 \cdot P = -\frac{2\omega \mid d_{ab} \mid^2}{\hbar} \mu E \,, \tag{2}$$

$$\frac{\partial \mu}{\partial t} = \frac{2}{\hbar \omega} < E \frac{\partial P}{\partial t} >, \tag{3}$$

where the frequency of the transition between the levels corresponds to the field frequency. We are neglect the line width in the equation for polarization and the inversion relaxation due to external causes. There are δ - the decrement of field absorption in the medium, d_{ab} - the matrix element of the dipole moment (or rather its projection on the direction of the electric field), the population difference $\mu = n \cdot (\rho_a - \rho_b)$ in the unit volume, and the relative populations ρ_a , ρ_b of levels in the absence of a field, n is the density of the dipoles of the active medium. Fields are represented by $E = [E(t) \cdot \exp\{-i\omega t\} + E^*(t) \cdot \exp\{i\omega t\}]/2$ and $P = [P(t) \cdot \exp\{-i\omega t\} + P^*(t) \cdot \exp\{i\omega t\}]/2$. Wherein $< E^2 > = \mid E(t) \mid^2 /2$.

For slowly varying field amplitudes $E(t)$ and polarizations $P(t)$, the following equations are valid

$$\frac{\partial E(t)}{\partial t} + \delta \cdot E(t) = 2i\pi\omega P(t) \,, \tag{4}$$

$$\frac{\partial P(t)}{\partial t} = \mid d_{ab} \mid^2 (\mu / \hbar) \frac{E(t)}{i} \,. \tag{5}$$

Using (3) - (5) in the absence of energy loss, you can get the ratio

$$\frac{\partial}{\partial t} \left(\frac{\partial \mu}{2 \mid E \mid \partial t} \right)^2 = -\frac{\mid d_{ab} \mid^2}{4\hbar^2} \frac{\partial}{\partial t} \mu^2 \tag{6}$$

from which the equation for population inversion follows

$$\frac{\partial \mu}{\partial t} = i \frac{2 \mid E \mid \mid d_{ab} \mid}{2\hbar} \mu \,, \tag{7}$$

the meaning of this equation is that population inversion oscillates with the Rabi frequency Ω (the so-called nutation of population inversion)

$$\Omega = \frac{2 \mid E \mid \mid d_{ab} \mid}{2\hbar} \,. \tag{8}$$

It can be shown [10] that equation (7) remains valid also in the case when the energy loss is significant, that is, at $\delta \neq 0$.

EQUATIONS OF MODEL

Here it is useful to pay attention to the fact that population inversion is a real value. Therefore, only the real part of the expression $\mathrm{Re}\,\mu = (\mu + \mu^*)/2$ we may use. From equation (3) you can get the law of energy conservation in the system

$$\mathrm{Re}(\mu - \mu_0) = N_0 - N - \delta \int_0^t N(t')\, dt' \tag{9}$$

We use the following notation:

$N = \sum_{j=1}^{S} N_j$, $N_j = 2 \cdot \frac{1}{S} N \cdot \mathrm{Cos}^2 \{2\pi \frac{j}{S} + \alpha\}$, $\mu_j = \mu_{0j} \cdot \exp(i\Phi_j)$ - initial population inversion, $N = \mid E \mid^2 /4\pi\hbar\omega\mu_0$ - relative number of quanta in the system. Here the waveguide length is chosen equal to the radiation wavelength[1], - the constant phase. The spatial structure of the field, which is determined by the boundary conditions, the nature of

[1] If the waveguide length is longer, but a multiple of the emission wavelength, which, generally speaking, the description will not change qualitatively, only the value of the damping factor will be different.

reflection and radiation, will be considered constant for fixed values and, the time scale will be determined from the relation $\tau = \Omega_0 t = \frac{(4\pi\omega)^{1/2}\sqrt{|\mu_0|}\,|d_{ab}|}{\hbar^{1/2}} t$, then $\delta_1 = \delta / \Omega_0$, we divide the entire system length into segments with a single population inversion value $0 < j \le S = 100$.

Consider the case when the field in the waveguide will attenuate in the presence of an unexcited active medium. In this case, we choose the initial conditions

$$M_j(0) = M_{0j} = -\frac{1}{S},\ \Phi_j(\tau = 0) = 0,\ N(\tau = 0) = N_0 = 1.45,\ N_j(\tau = 0) = 2\frac{1}{S}\cdot N_0 \cdot \mathrm{Sin}^2\{2\pi\frac{j}{S}\}.$$

When this equation (7), (9) can be written as

$$\frac{\partial \Phi_i}{\partial \tau} = \sqrt{N_j}\ , \tag{10}$$

$$\sum_{j=1}^{S} M_{j0}\,\mathrm{Cos}\,\Phi_j + 1 = N_0 - N\ . \tag{11}$$

If the active medium is excited, it is possible to consider problems of field excitation in a waveguide under conditions of different absorption levels. You can choose the initial conditions $M_j(0) = M_{0j} = S^{-1}$, $\Phi_j(\tau = 0) = 0$, $N(\tau = 0) = N_0 = 0.001$, $N_j(\tau = 0) = 2\frac{1}{S}\cdot N_0 \cdot \mathrm{Sin}^2\{2\pi\frac{j}{S}\}$.

In this notation, the system of equations (7), (9) is written in the form

$$\frac{\partial \Phi_i}{\partial \tau} = \sqrt{N_j}\ , \tag{12}$$

$$\sum_{j=1}^{S} M_{j0}\,\mathrm{Cos}\,\Phi_j - 1 = N_0 - N - \delta_1 \int_0^{\tau} d\tau' N(\tau') = N_0 - \sum_{j=1}^{S} N_j - \delta_1 \int_0^{\tau} d\tau' N(\tau')\ . \tag{13}$$

RESULTS OF NUMERICAL CALCULATIONS

Absorption of a large amplitude wave in the waveguide with unexcited active medium

Each region of space of the active medium contributes to the total number of field quanta in the waveguide. The field in the waveguide is a standing wave, so the amplitude of the field and the Rabi frequency at each point in the waveguide space depend only on time. An increase in population inversion leads to absorption of field quanta by the active medium, a decrease in population inversion, on the contrary, increases the number of quanta in the system. In each region of space, the Rabi frequency is different and the total field is formed under the influence of the interference of local oscillations (local nutation) of population inversion in the entire waveguide volume. For this case, described by equations (10) and (11), changes in the relative number of quanta in the system $N = N(\tau)$ are shown in Fig.1. The first minimum $N_{\min} = 0.047$ and the maximum field $N_{\max} = 0.75$ are reached at $\tau = 45.47$ and $\tau = 90.92$, respectively.

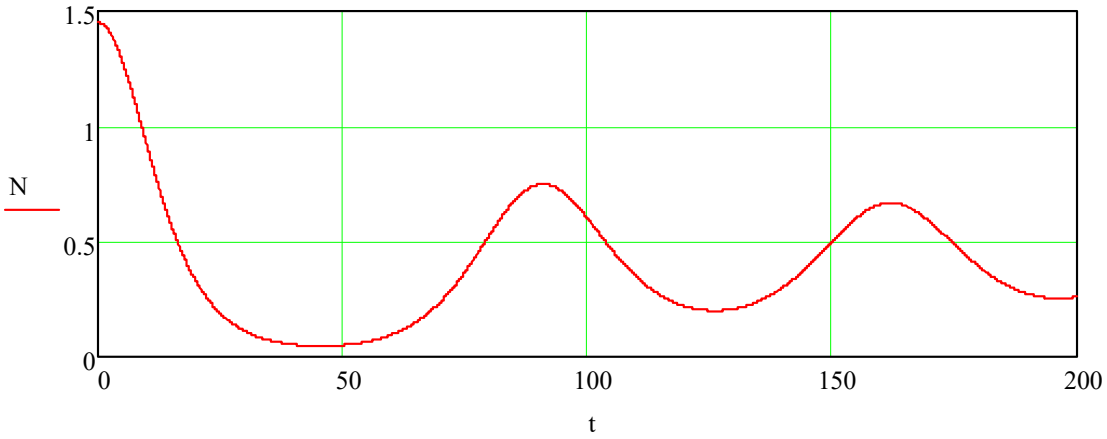

Fig. 1. The process of field attenuation - the relative number of quanta $N = N(\tau)$ in the system with time in the absence of external losses ($\delta_1 = 0$).

Periodic changes in the number of quanta in the nonlinear mode are attenuated due to the interference of population inversion oscillations in different segments. The behavior of the population inversion of individual segments is presented in detail in Fig.2. The linear decrement of the field attenuation $\delta_{1N} = (dN / Nd\tau)$ in the selected time scale at the linear stage of the process, obtained from the analysis of Fig. 1 is equal to $\delta_{1N} = -0.113$

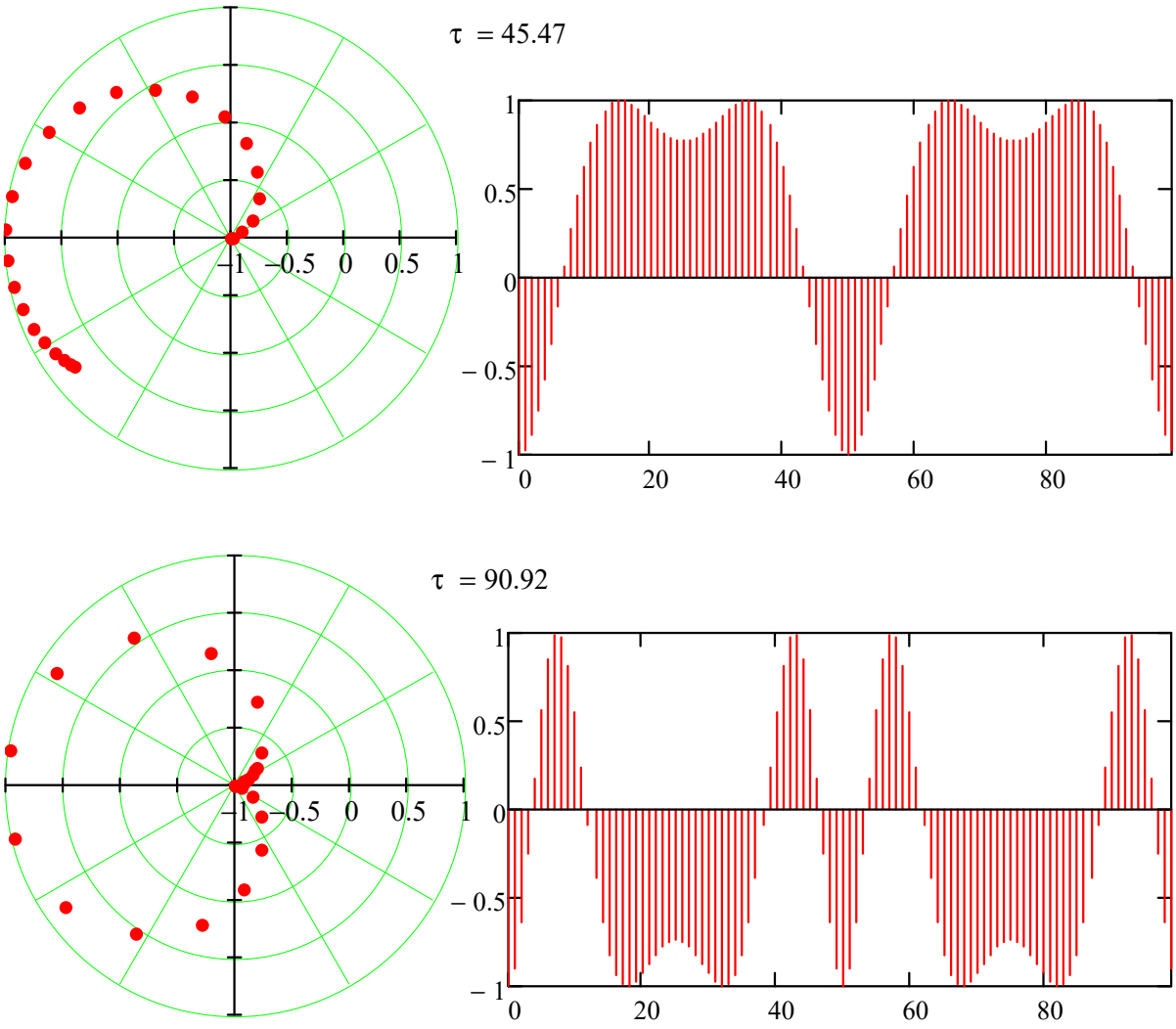

Fig. 2. The behavior of the real part of the population inversion $\mathrm{Re}\, M_j = |M_j| \cdot \mathrm{Cos}\,\Phi_j$ in each of the segments $0 < j \le S/4$ in the phase space $(\mathrm{Cos}\,\Phi_j; \Phi_j)$ (left), and in the diagrams for all segments $0 < j \le S = 100$ (right) for points in time $\tau = 45.47$ (above) and $\tau = 90.92$ (below)

This type of attenuation is nonlinear attenuation and is characterized by a periodic energy exchange between the wave and the active medium, just as it happens in the case of Landau attenuation [11].

Generation of a field in a waveguide filled with an excited active medium

The description of this process is possible within the framework of the system of equations (12) and (13). We first consider the case of the absence of external losses in the waveguide ($\delta_1 = 0$). The change in the relative number of quanta $N = N(\tau)$ in the system is shown in Fig.3.

It is not difficult to see that the periodic changes in the number of quanta in the nonlinear mode are attenuated due to the interference of the oscillations of population inversion in different segments. The behavior of the population inversion of individual segments at $\tau = 72$ and $\tau = 94$ is shown in detail in Fig.4.

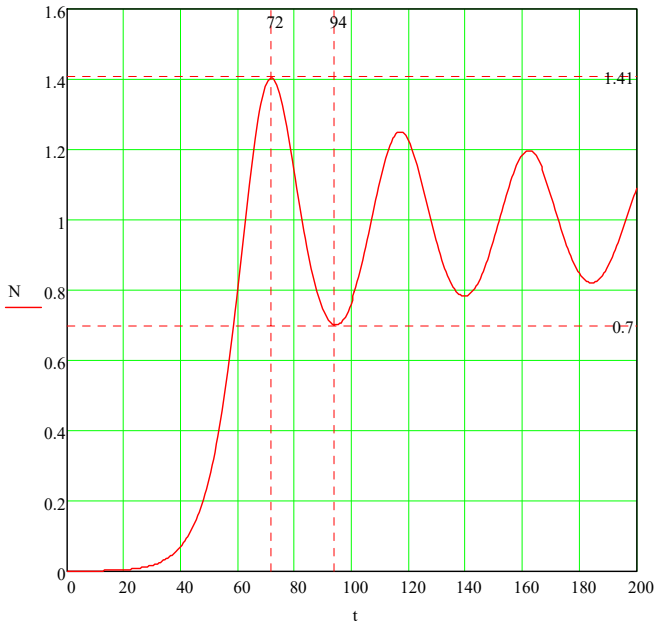

Fig. 3. The behavior of the relative number of quanta $N = N(\tau)$ in the system with time in the absence of loss ($\delta_1 = 0$)

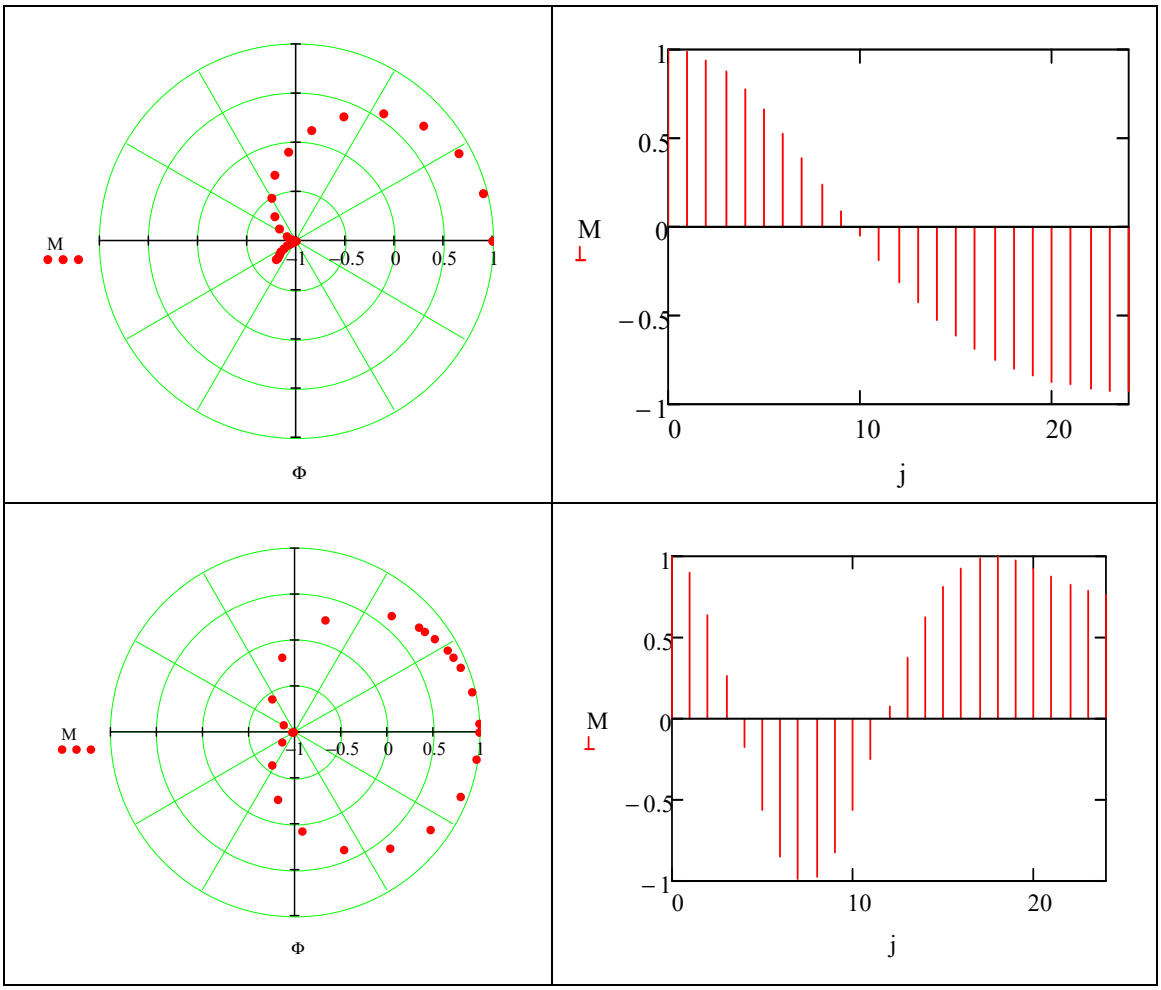

Fig.4. The behavior of the real part of the population inversion $\mathrm{Re}\, M_j = |M_j| \cdot \mathrm{Cos}\,\Phi_j$ in each of the segments $0 < j \le S/4 = 25$ in the phase space $(\mathrm{Cos}\,\Phi_j; \Phi_j)$ (left), and in the diagrams for all segments $0 < j \le S = 100$ (right) for points at $\tau = 72$ (above) and $\tau = 94$ (below)

Accounting for the absorption or removal of energy from the system corresponds to the case $\theta = (\delta / \Omega_0) / \gamma_0 = \delta_1 / \gamma_0 > 0$, where $\gamma_0 = \gamma(\theta = 0) = (dN / Nd\tau)_{MAX} = 0.138$ is the linear increment of instability development in the selected time scale at the linear stage of the process, obtained from the analysis of Fig. 5. It is easy to see that θ here the ratio of the field absorption decrement in the system in the absence of an active medium δ_1 to the increment of the non-dissipative (or non-radiative) instability mode $\gamma_0 = \gamma(\theta = 0)$.

In the case of radiation from a waveguide, when $\delta \neq 0$, better to choose $N_j(\tau = 0) = 2\frac{1}{S} \cdot N_0 \cdot \mathrm{Sin}^2\{2\pi\frac{j}{S} + \varphi\}$, where φ is an constant phase associated with δ the following way. Generally speaking $\delta \approx \frac{c}{4\pi} |E(x=0)|^2 / (\frac{\lhd |E|^2 \rhd}{4\pi} b)$, where b is the waveguide length, where, by our assumption, a countable number of modes fit. It is easy to see that $|E(x=0)|^2 = 2 \lhd |E|^2 \rhd \mathrm{Sin}^2 \varphi$ and $\delta \approx (2c/b) \cdot \mathrm{Sin}^2 \varphi$. It is important to note that if $b = m\lambda$, where λ is the wavelength, then under conditions of a fixed attenuation value $\delta = \delta \approx (2c \cdot m / b) \cdot \mathrm{Sin}^2 \varphi$. The result of this does not change.

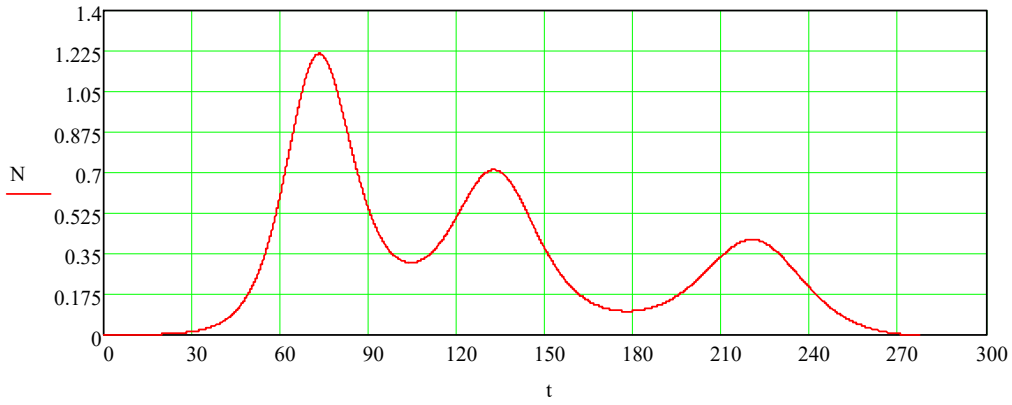

Fig. 5. The behavior of the relative number of quanta in a system with absorption (radiation) with time ($\delta_1 = 0.01$, or $\theta = 0.073$)

In this case, the behavior of the number of quanta in the system acquires a damped oscillating character. It is useful to present the change in the linear increment of the process $dN / Nd\tau$, the maximum attainable relative field intensity N_{MAX}, as well as the maximum energy flow from the system $(\theta \cdot N)_{MAX}$ as a function of θ (Fig. 6.).

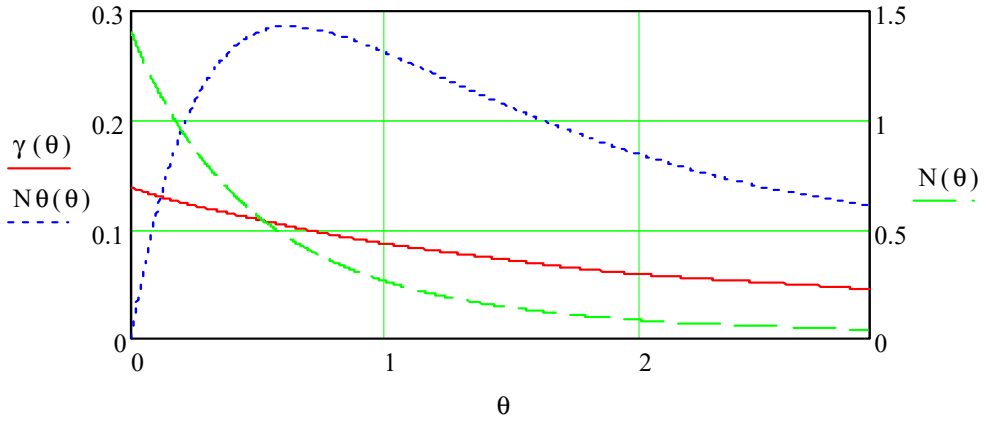

Fig. 6. The values of the linear increment of the process $dN / Nd\tau$, the maximum attainable relative number of quanta N_{MAX}, as well as the maximum energy flux from the system $(\theta \cdot N)_{MAX}$ as a function of θ

CONCLUSION

Above, we consider the energy exchange between the field, which is a standing wave in the waveguide and the active medium that fills its space. In each region of the waveguide space, the amplitude of the field of a standing wave formed due to partial or full reflection from the ends of the system is different and varies only with time. A quasi-periodic change in population inversion is determined by the Rabi frequency, which, is associated[1, 2], with the probability of induced radiation with a positive population inversion, or induced absorption with its negative value. An increase in population inversion leads to absorption of field quanta by the active medium, a decrease in population

inversion, on the contrary, increases the number of quanta in the system. The total field is formed under the action of the interference of oscillations of population inversion of the local regions of the active medium in the entire volume of the waveguide.

The attenuation of a field of large amplitude to a waveguide filled with an unexcited active medium is nonlinear. In the developed mode, this process has the character of energy exchange between the field and the active medium. In this case, the wave attenuation is replaced by its growth, just as in the well-known case of Landau kinetic damping [11].

The nature of the excitation of a field by an inverted active medium in a waveguide is also discussed. Under the conditions of the final level of external losses, absorption or output of the radiation energy leads to a decrease in the field intensity in the active zone. The competition of the processes of radiation and absorption leads to the fact that the nature of oscillations (nutation) of population inversion at different points in the waveguide space is different. The interference of asynchronous spatially localized oscillations of population inversion in the waveguide volume leads to changes in the amplitude of the field. The change in the linear increment of the process $dN / Nd\tau$, the maximum attainable relative field intensity N_{MAX}, and the maximum energy flow from the system $(\theta \cdot N)_{MAX}$ as a function of θ which determine the level of wave energy absorption, are presented. Consideration of these problems is important for understanding the processes of generation of induced radiation, which, as noted by Towns Ch. [12], is to a large extent coherent radiation.

ACKNOWLEDGEMENTS

The authors are sincerely grateful to V. A. Buts and V. D. Khodusov for useful discussions and attention to the work.

ORCID IDs

Volodymyr Kuklin http://orcid.org/0000-0002-0310-1582, **Eugen Poklonskiy** https://orcid.org/0000-0001-5682-6694

REFERENCES

[1] A.S. Davydov, *Quantum mechanics*, (Fizmatgiz, Moscow, 1963), pp. 748. (in Russian)
[2] L. Allen and J. Eberly, *Optical resonance and two-level atoms,* (John Wiley and Sons, New York, London, Sydney, Toronto, 1975), pp. 222.
[3] S.G. Zeiger, Yu.L. Klimontovich, P.S. Landa, E.G. Lariontsev and E.E. Fradkin, *Wave and fluctuation processes in lasers*, (Nauka, Moscow, 1974), pp. 415. (in Russian)
[4] Landa P.S. *Auto-oscillations in distributed systems*, (Nauka, Moscow, 1983), pp. 320.
[5] G. Haken, *Synergetics,* (Mir, Moscow, 1980), pp. 403. (in Russian)
[6] V.V. Yanovskiy, *Лекции о нелинейных явлениях. Том 1* [*Lectures on nonlinear phenomena, Vol. 1*], (Institute of Single Crystals, Kharkiv, 2006), pp. 456; V.V. Yanovskiy, *Лекции о нелинейных явлениях. Том 2* [*Lectures on nonlinear phenomena, Vol. 2*], (Institute of Single Crystals, Kharkiv, 2007), pp. 448. (in Russian)
[7] V.A. Buts, Problems of Atomic Science and Technology, **5**(6), 146-148 (2012).
[8] V.M. Vorobiev, V.M. Kuklin, Letters in ZhTF, **13**(22), 1354-1360 (1987).
[9] E.V. Belkin, A.V. Kirichok and A.S. Petrenko, Problems of Atomic Science and Technology, **4**, 299-301 (2010).
[10] V.M. Kuklin, Problems of atomic science and technology, Series “Plasma Electronics and New Methods of Acceleration”, **4**(122), 91–95 (2019).
[11] A.A. Andronov, Izvestiya Vuzov. Radiophysics, **4**(5), 861–866 (1961). (in Russian)
[12] Ch. Towns, UFN, **88**(3), 461–483 (1966). (in Russian)

ОБ ОБМЕНЕ ЭНЕРГИЕЙ МЕЖДУ ПОЛЕМ И АКТИВНОЙ СРЕДОЙ ВОЛНОВОДА

В.М. Куклин, Е.В. Поклонский

Харьковский национальный университет имени В. Н. Каразина, Харьков, Украина
пл. Свободы 4, г. Харьков, Украина, 61022

Работа на основе полуклассического описания представляет результаты изучения процессов поглощения и излучения поля в форме стоячей волны в волноводе, заполненном двухуровневой активной средой. В условиях пространственной неоднородности интенсивности поля возникает интерференция квазипериодических осцилляций инверсии населенностей в различных локальных областях волновода. Квазипериодическое изменение инверсии населенностей определяется частотой Раби, которая как известно, связана с вероятностью индуцированного излучения при положительной инверсии населенностей, или индуцированного поглощения при ее отрицательном значении.Так как изменение инверсии населенностей сопровождается поглощением или излучением квантов поля, это приводит к обмену энергией между полем и активной средой, размещенной в волноводе. Показано, что затухание поля большой амплитуды волноводе, заполненном невозбужденной активной средой, является нелинейным. В развитом режиме этот процесс носит характер обмена энергией между полем и активной средой. При этом затухание волны сменяется ее ростом, подобно тому, как это происходит в известном случае кинетического затухания Ландау. Конкуренция процессов излучения и поглощения приводит к тому, что характер осцилляций (нутации) инверсии населенностей в разных точках пространства волновода оказывается различным. И в этом случае именно интерференция несинхронных пространственно локализованных осцилляций инверсии населенностей в объеме волновода приводит к изменениям амплитуды поля. В работе обсуждается процесс возбуждения поля в волноводе предварительно инвертированной двухуровневой активной средой при учете внешних механизмов поглощения энергии колебаний. Рассмотрение этих проблем важно для понимания процессов генерации индуцированного излучения, которое как отметил Ч. Таундс в большой степени является излучением когерентным.

КЛЮЧЕВЫЕ СЛОВА: поглощения и излучения поля, двухуровневая активная среда, частота Раби, интерференция осцилляций инверсии населенностей.

ПРО ОБМІН ЕНЕРГІЄЮ МІЖ ПОЛЕМ ТА АКТИВНИМ СЕРЕДОВИЩЕМ ХВИЛЕВОДУ

В.М. Куклін, Є.В. Поклонський

Харківський національний університет імені В.Н. Каразіна, Харків, Україна
м. Свободи 4, м. Харків, Україна, 61022

Робота на основі напівкласичного опису представляє результати вивчення процесів поглинання та генерації поля в формі стоячій хвилі в хвилеводі, що заповнений дворівневим активним середовищем. В умовах просторової неоднорідності інтенсивності поля виникає інтерференція осциляцій інверсії заселеності в різних локальних областях хвилеводу. Квазіперіодичні зміна інверсії заселеності визначається частотою Рабі, яка як відомо, пов'язана з ймовірністю індукованого випромінювання при позитивній інверсії заселеності, або індукованого поглинання при її негативному значенні. Так як зміна інверсії заселеності супроводжується поглинанням або випромінюванням квантів поля, це призводить до обміну енергією між полем та активним середовищем, що розміщено у хвилеводі. Показано, що затухання поля великої амплітуди в хвилеводі, що заповнений активним середовищем, є нелінійним. У розвиненому режимі цей процес носить характер обміну енергією між полем і активним середовищем. При цьому загасання хвилі змінюється її зростанням, подібно до того, як це відбувається у відомому випадку кінетичного загасання Ландау. Конкуренція процесів випромінювання і поглинання призводить до того, що характер осциляцій (нутацій) інверсії заселеності в різних точках простору хвилеводу виявляється різним. І в цьому випадку саме інтерференція несинхронних просторово локалізованих осциляцій інверсії заселеності в обсязі хвилеводу призводить до змін амплітуди поля. У роботі обговорюється також процес збудження поля в хвилеводі попередньо інвертованою дворівневим активним середовищем при обліку зовнішніх механізмів поглинання енергії коливань. Розгляд цих проблем важливий для розуміння процесів генерації індукованого випромінювання, яке як зазначив Ч. Таундс в великій мірі є випромінюванням когерентним.

КЛЮЧОВІ СЛОВА: поглинання і випромінювання поля, дворівневе активне середовище, частота Рабі, інтерференція осциляцій інверсії заселеності.

East European Journal of Physics
East Eur. J. Phys. **3**. 54-62 (2019) DOI:10.26565/2312-4334-2019-3-07

PACS: 29; 29.40.Mc; 29.40.-n

THE INVESTIGATION OF MECHANISMS OF FAST NEUTRON REGISTRATION IN OXIDE SCINTILLATORS

Gennadiy Onyshchenko[1,2*], Volodymyr Ryzhikov[2], Ivan Yakymenko[1], Valery Khodusov[1], Sergei Naydenov[3,2], Alexandr Opolonin[2], Sergei Makhota[2]

[1] *V. N. Karazin Kharkiv National University, 4 Svobody Sq., Kharkiv, 61022, Ukraine;*
[2] *Institute for Scintillation Materials, STC "Institute for Single Crystals", National Academy of Sciences of Ukraine, 60 Nauky Ave., 61001 Kharkiv, Ukraine;*
[3] *Institute for Single Crystals, STC "Institute for Single Crystals", National Academy of Sciences of Ukraine, 60 Nauky Ave., 61001 Kharkiv, Ukraine*
**E-mail: gennadij.m.onyshchenko@karazin.ua*

Received June 30, 2019; Received August 8, 2019; accepted September 16, 2019

The contributions of gamma rays from the inelastic scattering reaction and the resonant reaction in the process of slowing down fast neutrons inside the oxide detector volume are investigated. For this the countable efficiency of the $ZnWO_4$, $CdWO_4$, $Bi_4Ge_3O_{12}$ oxide scintillators in terms of pulses/neutron during the registration of the fast neutrons from a ^{239}Pu-Be source was measured. It is assumed that the response of detectors during neutron moderation in oxide scintillators with an effective thickness of about 40—50 mm is formed by instantaneous gamma rays from inelastic, resonant inelastic scattering reactions, as well as delayed gamma rays from the capture reaction of resonance neutrons. The parameters of the nuclei, which determine the detector response — the density of the nuclear levels of the compound nuclei being formed, the widths of the resonance regions, the lifetimes of the excited nucleus state were considered. It was found that the registration of a cascade of gamma rays from the discharge of excited levels leads to a significant increase in the countable efficiency of the detector and, as a consequence, an increase in the sensitivity of the detector to fast neutrons. The measured response in terms of pulses/neutron for the ZWO detector — 64, for CWO — 36, for BGO — 2.5. The response of the detectors was recorded by the broadband tract with a time feedback of $\tau\sim$ 0.7 ns. The measured values of the efficiency are explained by the fact that, in our case, the reaction of inelastic scattering is the starting process, which starts the process of discharging nuclear long-lived ($\sim$ 1–1000 ns) states excited in both inelastic scattering and in resonance capture reaction. The registration of the gamma-quanta from discharge leads to an increase the countable efficiency of the detector. The observed increase of the countable efficiency of the secondary gamma quanta is realized when neutrons are moderated inside the oxide detectors with a thickness of 40—50 mm or more. The measurement error of the registration efficiency was about 7%.

KEY WORDS: detector, fast neutrons, excited states, countable efficiency, density of nuclear levels.

The creation of highly sensitive detectors for neutron and gamma-neutron radiation monitoring systems is an important task. The study of the response of single-crystal detectors under irradiation with fast neutrons is being done to develop efficient neutron and gamma-neutron detectors to control the unauthorized movement of fissile and radioactive materials. The goal of this work is to determine the countable efficiency of ZWO ($ZnWO_4$), CWO ($CdWO_4$), BGO ($Bi_4Ge_3O_{12}$) oxide single-crystal scintillators used in the registration of fast neutrons from a ^{239}Pu-Be source. In this work, also the contributions of the mechanisms of neutron energy conversion to secondary gamma quanta during moderation in the detector material also were studied. Earlier, in [1, 2], it was shown that the mechanism of inelastic scattering $(n, n'\gamma)_{in}$ in the energy range of 0.1–10 MeV can be used to register fast neutrons of the ^{239}Pu-Be source with heavy oxide scintillators [3–5].

In this paper, it is assumed that the response from detectors during neutron moderation in oxide scintillators is formed by instant gamma quanta of inelastic, resonance inelastic scattering, as well as delayed gamma quanta of radiation capture in the resonance region emitted by excited states of both compound nuclei and nuclei – products reactions. When fast neutrons are moderated in detector volume with a thickness of 4–5 cm and a resonance region of energies is $E \sim 0.1 - 100$ keV, in addition to the inelastic scattering reaction $(n, n'\gamma)_{in}$, inelastic resonance scattering $(n, n'\gamma)_{in\_res}$ is possible with the emission of instantaneous gamma

quanta, since the lifetime of a compound nucleus is very short. In this reaction $(n, n'\gamma)_{in}$, $n + A \to (A+1)^* \to A + n' + \gamma_{prt}$, the neutron emitted from the nucleus, having a significantly lower energy, is more likely to be re-captured by the nucleus in the radiation capture reaction in the resonance region $(n, \gamma)_{rad\_cap\_res}$ and form a new compound-core: $n + A \to (A + 1)^* \to (A + 1) + \gamma_{del}$, in which long-lived states are excited with lifetimes from some nanoseconds to some microseconds, which genetically related to quanta of the primary reaction of inelastic $(n, n'\gamma)_{in}$ scattering [6, 7]. Thus, the inelastic scattering reaction $(n, n'\gamma)_{in}$ is the "trigger", which starts the cascade process of creation and discharge of excited states in the nuclei of the crystals under study. It is the inelastic $(n, n'\gamma)_{in\_res}$ channel of resonance scattering and radiative capture $(n, \gamma)_{rad\_cap\_res}$ that serves as an effective source of additional neutrons and gamma quanta capable of generating gamma quantum cascades. If the lifetimes of the excited states are in the range of some nanoseconds and above, then registering the detector response using the broadband setup leads to increase the detector countable efficiency and, consequently, to increase the sensitivity to neutron and gamma radiation.

RESEARCH METHODS

To estimate the registration efficiency, we used the parameter "countable" efficiency or $pulses * s^{-1} * cm^{-2}/neutron * s^{-1} * cm^{-2}$ – the ratio of the detector count rate from $S_{win.det} = 1\ cm^{-2}$ to the particle flux density on the detector. In fact, if the detector had a window area of 1 cm^{-2}, then the number of pulses per one input particle was measured. Note that the energy efficiency of the detector cannot exceed 1, while the countable efficiency of the detector, in which multiple processes are possible, accompanied by the creation of a cascade of low-energy particles, may exceed 1.

A fast neutron with an energy of $E_n < 10$ MeV in the process of scattering and moderation in the detector material with linear dimensions of $\sim 3 - 5$ cm passes the energy range from 10 MeV to a few keV or less. This makes it possible to use, for the purposes of detection, processes that have, firstly, high cross sections for neutron interaction and, secondly, effectively produce secondary particles, for example, gamma rays, recoil protons. The processes generated a long-lived states exited with lifetimes ranging from some nanoseconds to some microseconds are due to the inelastic scattering $(n, n'\gamma)_{in}$, radiation capture in the resonance region $(n, \gamma)_{rad\_cap\_res}$ (Fig. 1).

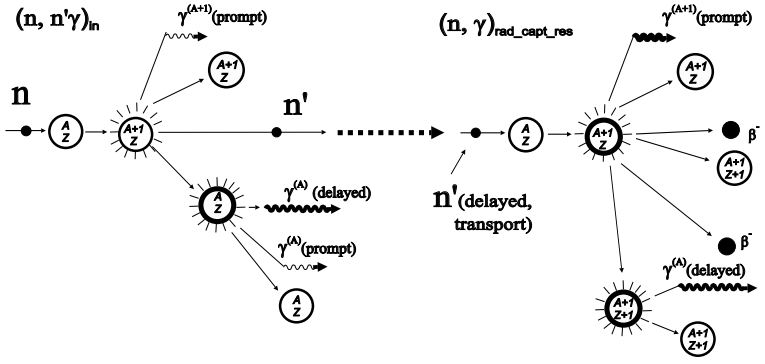

Fig. 1. The processes of inelastic scattering $(n, n'\gamma)_{in}$, radiation capture in the resonance region $(n, \gamma)_{rad\_capt\_res}$, in which instantaneous and delayed secondary gamma quanta produce in the range of 1 ns – 1 μs or more.

For the nuclei of the natural isotopic mixture the cross sections for inelastic scattering $(n, n'\gamma)_{in}$, inelastic resonance scattering $(n, \gamma)_{in\_res}$, radiation capture $(n, \gamma)_{rad\_cap\_res}$ with $E = 14$ MeV, radiation capture in the resonance region $(n, \gamma)_{rad\_cap\_res}$, radiation capture in the thermal region $(n, \gamma)_{rad\_cap}$ (see Table 1) were used from nuclear data bases [8, 9].

Measurement of the countable efficiency of the single-crystal ZWO, CWO, BGO detectors under irradiation of ^{239}Pu-Be source fast neutrons was carried out in spherical geometry [10], the photomultiplier was Hamamatsu R1307, the distance to the source detector was 1000 mm. ^{239}Pu-Be neutron source with a neutron flux of $0.95 \cdot 10^5$ neutron$*s^{-1}$ was used. The source was placed inside a lead ball Ø100 mm with a well Ø20 mm. The source size is Ø20x30 mm, weight is 52 g. The lead ball, besides the main task of reducing the influence of the accumulation factor in the material of the ball, simultaneously attenuates the accompanying gamma radiation from the ^{239}Pu-Be source. In the neutron source there is a concomitant high-energy gamma radiation from the reactions: ^{4}He+^{9}Be $\to$ ^{13}C* $\to$ ^{12}C*+n$\to^{12}$C+γ+n, $E_\gamma = 4.43$ MeV, ^{13}C* $\to$ ^{13}C+γ, $E_\gamma = 3.68$ MeV. In connection with the incomplete suppression of the accompanying high-energy gamma-quanta from the ^{239}Pu-Be source, an correction was add to the efficiency of detecting fast neutrons by registering gamma-quanta with energy $E_\gamma = 4.43$ MeV, which was $\simeq 0.08$ for the ZWO oxide scintillator. It is consist of the γ/n ratio for the ^{239}Pu-Be source, equal to 0.71 [11], the absorption of gamma rays with an energy of 4.43 MeV in d=40 mm

of lead, which was 0.15, the absorption efficiency of gamma quanta with an energy of 4.43 MeV in ZWO Ø50 mm was $\simeq$ 0.80. The correction for the absorption of fast neutrons in a protective lead ball due to the radiative capture reaction (n,γ) was determined experimentally using a ^{6}LiI(Eu) detector and amounted to 2.5%. The size of the scintillator ^{6}LiI(Eu) is Ø15x10 mm, the enrichment in ^{6}Li is 96%. The thermal peak (α+t) for ^{6}LiI(Eu) had a gamma equivalent of 3.98 MeV, fast neutrons were recorded in the energy range 3.98 MeV $\div$ 10 MeV. The correction for gamma rays with energy E = 4.43 MeV was taken into account. The contribution of scattered fast neutrons from the walls of the room did not exceed 3%. The correction is determined using a ^{6}LiI(Eu) detector by measuring the deviation from the inverse square law when registering fast neutrons. The contribution of scattered gamma radiation in the source-detector distance range R = 1$\div$2 m did not exceed $\sim$ 1%. The correction is determined by measuring the deviation from the inverse square law when registering ^{137}Cs quanta. An additional 5 mm thick lead shield served to protect the detectors from background gamma radiation. The background attenuation coefficient in the range of 10 keV-150 keV is $\simeq$ 3.

Table 1

Cross sections of inelastic scattering reactions $(n,n'\gamma)_{in}$, inelastic resonance scattering $(n,n'\gamma)_{in\_res}$, radiation capture $(n,\gamma)_{rad\_cap\_in}$, radiation capture in the resonance region $(n,\gamma)_{rad\_cap\_res}$, radiation capture in thermal region $(n,\gamma)_{rad\_cap}$ for the nuclei of the natural isotopic mixture that made scintillators BGO, CWO, ZWO.

Isotops mixture, nat.	Reactions	σ, barn (E = 0.0253 eV)	σ, barn, (res.) (0.5 eV- 10 MeV)	σ, barn (E = 14 MeV)	$E-$ thresh., keV
$_{48}$Cd	$(n,n'\gamma)_{in}$	-	-	0.4163	247.6
	$(n,\gamma)_{rad\_cap\_in}$	-	-	0.8386 mb	-
	$(n,\gamma)_{rad\_cap\_res}$	-	66.59	-	-
	$(n,\gamma)_{rad\_cap}$	2468	-	-	-
$_{74}$W	$(n,n'\gamma)_{in}$	-	-	0.4281	46.74
	$(n,\gamma)_{rad\_cap\_in}$	-	-	0.7421 mb	-
	$(n,\gamma)_{rad\_cap\_res}$	-	355.1	-	-
	$(n,\gamma)_{rad\_cap}$	18.15	-	-	-
$_{30}$Zn	$(n,n'\gamma)_{in}$	-	-	0.6192	94.72
	$(n,\gamma)_{rad\_cap\_in}$	-	-	0.924 mb	-
	$(n,\gamma)_{rad\_cap\_res}$	-	2.539	-	-
	$(n,\gamma)_{rad\_cap}$	1.062	-	-	-
$_{83}$Bi	$(n,n'\gamma)_{in}$	-	-	0.3611	900.7
	$(n,\gamma)_{rad\_cap\_in}$	-	-	0.756	-
	$(n,\gamma)_{rad\_cap\_res}$	-	0.1715	-	-
	$(n,\gamma)_{rad\_cap}$	0.03421	-	-	-
$_{32}$Ge	$(n,n'\gamma)_{in}$	-	-	0.5655	-
	$(n,n'\gamma)_{in\_res}$	-	3.684	-	-
	$(n,\gamma)_{rad\_cap\_in}$	-	-	-	-
	$(n,\gamma)_{rad\_cap\_res}$	-	5.997	0.5333 mb	-
	$(n,\gamma)_{rad\_cap}$	2.217	-	-	-

The statistical error in measuring the neutron registration efficiency was 7% for detectors with an effective thickness of d $\simeq$ 40 mm. The data accumulation time was 100 minutes for the source irradiation and the same time for background accumulation.

The block diagram of the electronic measuring setup, which includes PMT the Hamamatsu R1307 and a low-noise fast amplifier, is given in [12]. The signals with PMT amplitude from 2 mV (total noise of PMT and electronics was 10 mV) were amplified by a wideband (Δf$\simeq$500 MHz) preamplifier. In this time domain, both instantaneous signals from gamma quanta that occur in inelastic and resonance neutron scattering and capture

reactions, and discharge signals from long-lived ($\tau \simeq$ 1–1000 ns and more) nuclear states excited in reactions with neutrons can be present. In Fig. 2 shows the simultaneously registered signals (pulses /1 neutron) under the interaction of fast neutrons with the ZWO detector: the upper figure is from the broadband setup, $\tau \sim 7$ ns, taking into account the PMT, the lower figure is from the narrow-band path, $\tau \sim 1$ μs. Signals at the output of the preamplifier and at the input of the ADC were recorded by counters and observed with an oscilloscope.

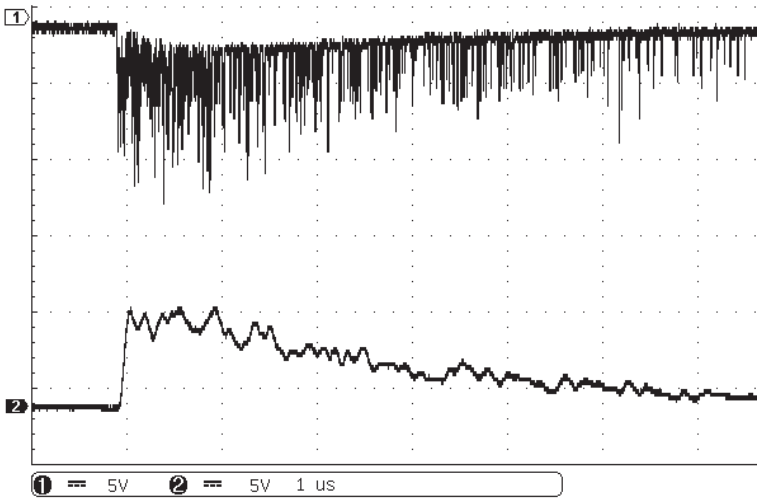

Fig. 2. Simultaneously registered signals forms (pulses / 1 neutron) for the ZWO detector. The upper pattern is from a broadband setup, the lower pattern is from a narrowband setup. X axis — time, 1 division = 1 μs. Y axis — volts. Visualisation — 500 MHz oscilloscope.

In accordance with the thermodynamic model of nuclei reactions [13] the average energy of the final products, temperature of nuclei in the reactions of inelastic scattering $(n, n'\gamma)_{in}$ and resonance radiation capture $(n, \gamma)_{rad\_cap\_res}$ neutrons at nuclei that are part of the oxide scintillators, were estimated Table 2. In calculation we supposed that the ^{239}Pu-Be source has an average neutron energy about 4.5 MeV and a maximum energy about 10 MeV.

In the present work, on the basis of the energy analysis performed, a systematic analysis of the discharge patterns of the states of isotopes excited in reactions with neutrons, which are part of the oxide scintillators available to us, and also formed in compound nuclei was carried out. The suitability of the isotopic composition of the detectors to generate gamma quanta from excited short-lived nuclear states is estimated. The nuclear states excited by fast neutrons with an average energy $E_n \simeq 4.5$ MeV are systematized, their number, the energies of the excited levels are estimated. The density of the levels excited in compound nuclei was estimated based on data from [14]. The results of the analysis for the natural mixture of ^{182}W-^{187}W isotopes that are part of the scintillators are presented in Table 3. A similar analysis also was performed for isotopes — ^{110}Cd – ^{114}Cd, ^{116}Cd, ^{64}Zn, ^{66}Zn, ^{68}Zn, ^{209}Bi.

From the Table 3 it can be seen that the most low-energy gamma-quanta emitted by excited states of the nuclei that make up the scintillators under study have lifetimes in the range of 1-1000 ns, born in inelastic scattering reactions $(n, n'\gamma)_{in}$: $(n+A) \rightarrow (A+1)^* \rightarrow A^* + n' + \gamma_{prt} \rightarrow A + \gamma_{del} + n' + \gamma_{prt}$, (A is the target nuclei, A+1 – compound nuclei). Also a slow neutrons produce gamma-quanta in the reaction of radiation capture in the resonance region $(n, \gamma)_{rad\_cap\_res}$: $(n + A) \rightarrow (A + 1)^* \rightarrow (A + 1) + \gamma_{del}$. It can be assumed that the response of the detector to fast neutrons is determined, firstly, by the registration of instantaneous secondary gamma quanta from inelastic scattering, inelastic resonance scattering and radiation capture in the resonance region. In addition, genetically related cascades of gamma-quanta of discharge of excited states of nuclei in the range of 1–1000 ns from the listed reactions were taken into account. The model response of detectors to fast neutrons was formed on the basis of the cross sections of the main processes, the densities of the levels of the compound nuclei produced during scattering, the width of the resonance region, the number of excited states were taken into account Table 4 [8, 9, 14–16]. The duration of the lifetime of radiation products of short-lived (1–1000 ns) states of the daughter nuclei genetically related to the emitted instantaneous gamma quanta excited in the compound nucleus as in inelastic scattering $(n, n'\gamma)_{in}$ neutrons in the energy range $E_n \sim 0.1 \div 10$ MeV, was also taken into account inelastic resonance scattering $(n, n'\gamma)_{in\_res}$ the energy range $E_n \sim 0.1 \div 150$ keV and radiation capture in the resonance region $(n, \gamma)_{rad\_cap\_res}$. The abundance of the considered isotopes was taken into account.

Table 2

The esimate of the average energy, temperature of the final products in the reactions of neutron inelastic scattering $(n, n'\gamma)_{in}$ for $E_n \simeq 4.5$ MeV, 10 MeV and inelastic radiation capture $(n, \gamma)_{rad\_cap\_res}$ at $E_n \sim 0.15$ MeV on nuclei of oxide scintillators. A – target nuclei, C – compaund nuclei.

$(n, n'\gamma)_{in}$	^{65}Zn	^{182}W	^{65}Zn	^{182}W	$(n, \gamma)_{rad\_cap\_res}$	^{65}Zn	^{182}W
Neutron separation energies, B_n	11.1	6.2	11.1	6.2	Neutron separation energies, B_n	11.1	6.2
T_{n_inp}	4.5	4.5	10	10	T_{n_inp}	0.15	0.15
$U_{ex}, max(C^*)$	15.6	10.7	21.1	16.2	$U_{ex}, max(C^*)$	11.25	6.35
$U_{ex}, max(A^*)$	4.5	4.5	10	10			
$Temperature\, \Theta, (A^*)$	1.5	0.7	2.2	1	$Temperature\, \Theta, (C^*)$	2.4	0.8
$T_{n\_out}, 2\Theta$	3	1.4	4.4	2			
$U_{ex\_remain.}, (A^*)$	1.5	3.2	5.6	8			

Table 3

Parameters of energy states of W isotopes excited by fast neutrons in inelastic scattering $(n, n'\gamma)_{in}$ reactions, radiation capture in the resonance region $(n, \gamma)_{rad\_cap\_res}$.

Reactions	Level energy, keV	Life-time, ns	J^π	Reactions	Level energy, keV	Life-time, ns	J^π
^{182}W(n, n'γ)^{182}W	g.s. 100.1 1289.1	 1.38 1.12	0^+ 2^+ 2^-	^{184}W(n, n'γ)^{184}W	g.s. 111.1 1285	 1.29 8330	0^+ 2^+ 5^-
^{182}W(n, γ)^{183}W	g.s. 308.5 453	 5.3 s 18.5	$1/2^-$ $7/2^-$	^{184}W(n, γ)^{185}W	g.s. 173.7 197.4 243.6	75.1 d 1.5 1.67 min 19.3	$3/2^-$ $7/2^-$ $11/2^+$ $7/2^-$
^{183}W(n, n'γ)^{183}W	g.s. 308.5 453	 5.3 s 18.5	$1/2^-$ $7/2^-$	^{186}W(n, n'γ)^{186}W	g.s. 122.6 1517.2	 1.04 18000	0^+ 2^+ 7^-
^{183}W(n, γ)^{184}W	g.s. 111.1 1285	 1.29 8330	0^+ 2^+ 5^-	^{186}W(n, γ)^{187}W	g.s. 350.4 364.2 410.1	 5 15 1380	$3/2^-$ $7/2^-$ $9/2^-$ $11/2^+$

The registration of gamma-discharge quanta in the region of lifetimes of nuclear states about 1 - 100 ns or more was possible due to the use of the fast preamplifier based on a current – voltage converter with a speed of $\sim$ 500 MHz ($\tau \sim 0.7$ ns). When using the spectrometric tract ($\tau \simeq 1$ μs), the value of the countable efficiency for ZWO and CWO decreases by approximately two orders of magnitude and is 0.6-0.7, that's why significant number of short-lived signals are combined (integrated). In the spectrometric mode, the key role is played by the inelastic scattering cross section, and the secondary reaction products with neutrons are combined into one detector response, which can be called instantaneous. Despite the fact that W and Cd have a large capture cross section in the resonance region, $\sigma_{res}(W) \simeq 355$ b, $\sigma_{res}(Cd) \simeq 67$ b, it does not manifest itself in the spectrometric mode, since the fast detector signals are integrated. Apparently, the secondary products of reactions with neutrons emitted by compound nuclei $C = (A + 1)$ are concentrated in the range from units to several hundred nanoseconds, which confirms experimentally the result of registration. The countable efficiency for BGO during the transition to the spectrometric regime remains almost at the same level, i.e. $\sim$2.5 pulses/neutron. This can be explained by the fact that compound nuclei formed in reactions with BGO nuclei have practically no states with an interval of lifetimes about $1 - 10^3$ ns. In addition, the Bi and Ge nuclei have a small cross section for resonance scattering; therefore, the broadband setup offers no advantages over the narrowband when using a BGO-based detector.

Table 4

Nucleus parameters weighted by the abundance in the natural mixture of isotopes of BGO, CWO, ZWO scintillators: σ_{in}, σ_{res} cross sections, density of levels in the resonance region $\rho(E)$, MeV^{-1}, ΔE of resonance region, keV, lifetime of exited states, gap of exited levels, number of exited levels.

	Nuclei	Z	σ_{in}, barn	σ_r, barn	$\rho(E)$, dens.	ΔE, res.	Exited states τ, ns	Gap of exited levels ΔE_{ex}, keV	Number of excited levels in ΔE_{ex}
ZWO	Zn W	30 74	0.619 0.428	2.539 355.1	230.1 23825	150 5	4000 20	53.9 - 1910 244 - 1200	6 3
CWO	Cd	48	0.416	66.6	14608	9	85	245 - 316	1
BGO	Bi Ge	83 32	0.361 0.565	0.19 5.997	250 538	200 30	59 418	433 - 1500 175 - 5540	2 3

RESULTS

In the present work, experimental values of the countable efficiency for fast neutrons of the ^{239}Pu-Be source for single-crystal BGO detectors – 2.5 pulses/neutron, ZWO – 64 pulses/neutron and CWO – 36 pulses/neutron (Fig. 3, Table 5) are obtained. The data are expressed in units of ($pulses \cdot s^{-1} \cdot cm^{-2}/neutron \cdot s^{-1} \cdot cm^{-2}$), i.e. as a ratio of the countable rate from 1 cm^2 of the detector input window to the neutron flux density on the detector. In fact, this parameter gives the number of pulses from the entire detector, which are generated by one particle falling on the detector. On the Fig. 3, the experimental data are dark columns.

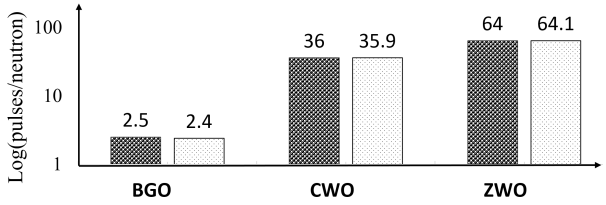

Fig. 3. Response to fast neutrons for BGO — 2.5 pulses/neutron, ZWO — 64 pulses/neutron, CWO — 36 pulses/neutron. Y-axis — ratio of countable rate from 1 cm^2 of the detector input window area to the flux density (pulses/neutron). The experimental data — dark columns, model data — light columns.

Also in this work, a model analysis of the most important, in terms of countable efficiency, characteristics of the nuclear levels of the nuclei that contain the detectors under study is made. The model responce of detectors was defined: $R \Longleftrightarrow \sigma_{in} \otimes \sigma_{res} \otimes \rho(E) \otimes \Delta E_{res} \otimes \Delta E_{ex} \otimes \tau_{ex} \otimes N_{ex}$. The model estimate (light columns, Fig. 3) of the response of the ZWO, CWO, BGO detectors agree quite satisfactorily with the experimental results obtained for the detection countable efficiency of fast neutrons.

Table 5

Experimental countable efficiency and model responce for BGO, CWO and ZWO in $pulses * s^{-1} * cm^{-2}/neutron * s^{-1} * cm^{-2}$ units. Neutron source — ^{239}Pu-Be. Experimental errors $< 7\%$.

Scintillators	Experimental countable efficiency, pulses/neutron	Model countable efficiency, pulses/neutron
BGO	2.5	2.4
CWO	36	35.9
ZWO	64	64.1

CONCLUSIONS

In the present work the countable efficiency of registration of fast neutrons of the ^{239}Pu-Be source for single-crystal detectors BGO, ZWO, CWO were measured. Also the most significant parameters of nuclei that are part of oxide scintillators, such as ZWO, CWO and responsible for improving the efficiency of detecting fast neutrons during their deceleration and entry into the resonance region, namely: inelastic scattering cross section, inelastic scattering cross section and capture in the resonance region, the width of the resonance region, the density of the nuclear levels of compound nuclei, the lifetimes of isomeric states, the energy of the excited levels, the quontity of excited states. The significance of these parameters is experimentally confirmed by an increase in the countable efficiency by about two orders of magnitude for gamma quanta with lifetimes $\tau \sim 1$–1000 ns for ZWO and CWO single crystal detectors compared to a recording method using a spectrometric amplification mode with $\tau \sim 1\,\mu$s, in which significant suppressions of response pulses from short-lived states. To effectively register the decay quanta of short-lived states, a broadband, fast-acting setup is required.

Thus, the use of heavy oxide scintillators in the countable mode of short impulses of response can significantly improve the registration statistics and the sensitivity of neutron detectors through the use of radiation capture in the resonance region $(n, \gamma)_{rad\_cap\_res}$, in which a chain of secondary gamma-quanta emitted by short-lived nuclear states and which are genetically related to the primary inelastic scattering reaction gamma-quantum $(n, n'\gamma)_{in}$. Note that in this case, the increase in statistics is due to the qualitative effect due to the genetic linkage of the mechanisms, and hence the reaction products. This will make it possible to create neutron and gamma-neutron detectors that are significantly more compact compared to existing ^{3}He-counters for monitoring low-intensity neutron and gamma-neutron fields.

ORCID IDs

Volodymyr Ryzhikov https://orcid.org/0000-0002-2833-2774,
Gennadiy Onyshchenko https://orcid.org/0000-0001-6945-8413,
Valery Khodusov https://orcid.org/0000-0001-6945-8413,
Ivan Yakymenko https://orcid.org/0000-0002-0194-8376,
Sergei Naydenov https://orcid.org/0000-0002-5585-763X.

REFERENCES

[1] M. Anelli, G. Battistoni, S. Bertolucci et al. Nucl. Inst. Meth. Phys. Res. **A, 580**, 368 – 372 (2007), DOI: 10.1016/j.nima.2007.08.005.

[2] L. L. Nagornaya, V. D. Ryzhikov, B. V. Grinyov, L. A. Piven', G. M. Onyshchenko and E. K. Lysetska, in: *Abstracts IEEE Nuclear Science Symposium*, (Drezden, Germany, 2008), pp. 1-3.

[3] B. Grynyov, V. Ryzhikov, L. Nagornaya, G. Onishcenko, L. Piven'. US Patent N 8.058.624 B2 (15 November 2011).

[4] V. D. Ryzhikov, B. V. Grinyov, G. M. Onyshchenko, L. A. Piven, O. K. Lysetska, O. D. Opolonin, S. A. Kostioukevitch and C. F. Smith, in: *XVI SPIE Optical Engineering Proceedings, "Hard X-Ray, Gamma-Ray, and Neutron Detector Physics"*, Editor(s): Arnold Burger; Larry Franks; Ralph B. James; Michael Fiederle (IEEE, San Diego, 2014), doi: 10.1117/12.2058185.

[5] V.D. Ryzhikov, S.V. Naydenov, G.M. Onyshchenko, L.A. Piven, T. Pochet and C.F. Smith, Nucl. Inst. Meth. Phys. Res. A, **903**, 287–296 (2018), doi: 10.1016/j.nima.2018.06.074.

[6] B. Grinyov, V. Ryzhikov, G. Onyshchenko, I. Yakymenko, S. Naydenov, O. Opolonin and S. Makhota, in: *Sixth International Conference "Engineering Of Scintillation Materials And Radiation Technologies"*, (ISMART, Minsk, 2018), pp. 46.

[7] V. Ryzhikov, G. Onyshchenko, I. Yakymenko, S. Naydenov, O. Opolonin and S. Makhota, in: *XVII конференция по физике высоких энергий и ядерной физике, ННЦ ХФТИ НАН Украины* [XVII Conference on High Energy Physics and Nuclear Physics, NSC KIPT NAS of Ukraine], (IPHE&NP, Kharkiv, 2019), pp. 96, (in Russian).

[8] Japan Atomic Energy Agency, Nuclear Data Center, in: https://wwwndc.jaea.go.jp/jendl/j40/j40nat.html, https://wwwndc.jaea.go.jp/jendl/j40/j40.html.

[9] The Nuclear Reaction Data Centres Network (JANIS, NRDC), in: http://www.oecd-nea.org/janisweb.

[10] O. Kazachkovskij, Atomic Energy, **83**(1), 509-515 (1997).

[11] G. Venkataraman, Dayashankar and J.S. Jayakar, Nuclear Instruments and Methods, **82**, 49-50 (1970).

[12] V. Ryzhikov, G. Onyshchenko, I. Yakymenko, S. Naydenov, A. Opolonin and S. Makhota, East Eur. J. Phys., **2**, 11-18 (2019).

[13] J.M. Blatt and V.F. Weisskopf, *Theoretical Nuclear Physics.* (Wiley, New York, 1952), pp.864.

[14] T. Egidy and D. Bucurescu. Physical Review C, **72**, 044311(1–22) (2005), doi: 10.1103/PhysRevC.72.044311.

[15] *Nuclear Data Sheets*, in: https://www.journals. elsevier.com/nuclear-data-sheets.

[16] M.C. Lederer and V.S. Shirley, editors, *Table of isotopes*, (Wiley-Blackwell, New Jersey, 1979), pp. 1632.

ИССЛЕДОВАНИЕ МЕХАНИЗМОВ РЕГИСТРАЦИИ БЫСТРЫХ НЕЙТРОНОВ В ОКСИДНЫХ СЦИНТИЛЛЯТОРАХ

Г. М. Онищенко[1], В. Д. Рыжиков[2], И. И. Якименко[1], В. Д. Ходусов[1], С. В. Найденов[3,2], А. Д. Ополонин[2], С. В. Махота[2]

[1]*Харьковский национальный университет имени В. Н. Каразина, Пл. Свободы, 4, Харьков, 61022, Украина;*
[2]*Институт сцинтилляционных материалов, НТЦ "Институт Монокристаллов", Национальная Академия Наук Украины, Пр. Науки, 60, 61001 Харьков, Украина;*
[3]*Институт Монокристаллов, НТЦ "Институт Монокристаллов", Национальная Академия Наук Украины, Пр. Науки, 60, 61001 Харьков, Украина*

Были изучены вклады гамма-квантов из реакции неупругого рассеяния и реакции резонансного рассеяния в процессе замедления быстрых нейтронов внутри объема оксидного детектора. Для этого измерена счетная эффективность оксидных сцинтилляторов $ZnWO_4$, $CdWO_4$, $Bi_4Ge_3O_{12}$ в терминах "импульсы/нейтрон"при регистрации быстрых нейтронов от источника ^{239}Pu-Be. Предполагается, что отклик детекторов при замедлении нейтронов в оксидных сцинтилляторах с эффективной толщиной около 40–50 мм формируется мгновенными гамма-квантами из реакций неупругого, резонансного неупругого рассеяния, а также задержанными гамма-квантами из реакции захвата замедленных нейтронов в резонансной области. Были рассмотрены параметры ядер, определяющие отклик детектора - плотность ядерных уровней образующихся составных ядер, ширина резонансной области, времена жизни возбужденного ядра состояния. Было установлено, что регистрация каскада гамма-квантов из разрядки возбужденных уровней ведет к значительному повышению эффективности счета детектора и, как следствие, повышению чувствительности детектора к быстрым нейтронам. Измеренный отклик в единицах импульс/нейтрон для детектора ZWO составил 64, для CWO — 36, для BGO — 2,5. Отклик детекторов регистрировался широкополосным трактом с быстродействием $\tau \sim 0{,}7$ нс. Измеренные значения счетной эффективности объясняются тем фактором, что в нашем случае реакция неупругого рассеяния является стартовым процессом, который запускает процесс разрядки ядерных долгоживущих ($\sim 1 \div 1000$ нс) состояний, возбуждаемых как в неупругом рассеянии, так и в резонансном захвате. Регистрация гамма-квантов разрядки приводит к увеличению счетной эффективности детектора. Наблюдаемое увеличение счетной эффективности вторичных гамма-квантов реализуется при замедлении нейтронов в оксидных детекторах толщиной 40–50 мм и более. Погрешность измерений эффективности регистрации нейтронов составляла 7 %.

КЛЮЧЕВЫЕ СЛОВА: детектор, быстрые нейтроны, возбужденные состояния, счетная эффективность, плотность ядерных уровней.

ДОСЛІДЖЕННЯ МЕХАНІЗМІВ РЕЄСТРАЦІЇ ШВИДКИХ НЕЙТРОНІВ В ОКСИДНИХ СЦИНТИЛЯТОРАХ

Г. М. Онищенко[1], В. Д. Рижиков[2], І. І. Якименко[1], В. Д. Ходусов[1], С. В. Найденов[3,2], О. Д. Ополонін[2], С. В. Махота[2]

[1]*Харківський національний університет імені В. Н. Каразіна, Пл. Свободи, 4, Харків, 61022, Україна;*
[2]*Інститут сцинтиляційних матеріалів, НТЦ "Інститут Монокристалів", Національна Академія Наук України, Пр. Науки, 60, 61001 Харків, Україна;*
[3]*Інститут Монокристалів, НТЦ "Інститут Монокристалів", Національна Академія Наук України, Пр. Науки, 60, 61001 Харків, Україна*

Були досліджені внески гамма-квантів із реакції непружного розсіяння і реакції резонансного розсіяння у процесі уповільнення швидких нейтронів всередині об'єма детектора. Для цього виміряна лічильна ефективність оксидних сцинтиляторів $ZnWO_4$, $CdWO_4$, $Bi_4Ge_3O_{12}$ у термінах "імпульси/нейтрон"при реєстрації швидких нейтронів від джерела ^{239}Pu-Be. Зроблено припущення, що відгук детекторів при уповільненні нейтронів у оксидних сцинтиляторах з ефективною товщиною близько 40—50 мм формується миттєвими гамма-квантами із реакції непружного, резонансного непружного розсіяння, а також затриманими гамма-квантами із реакції захвата уповільнених нейтронів у резонансній області. Були розглянуті параметри ядер, які визначають відгук детектора - щільність ядерних рівнів, що утворюються у складених ядрах, ширина резонансної області, час життя збуджених станів ядра. Встановлено, что реєстрація каскаду гамма-квантів із розрядки збуджених станів призводить до значного підвищення ефективності лічення детектора і, як наслідок, до підвищення чутливості детектора до швидких нейтронів. Виміряний відгук у одиницях імпульси/нейтрон для детектора ZWO склав 64, для CWO — 36, для BGO — 2,5. Відгук детекторів реєструвався широкополосним трактом із швидкодією $\tau \sim 0{,}7$ нс. Виміряні величини лічильної ефективності можна пояснити тим фактором, що в нашому випадку реакція непружного розсіяння є стартовим процесом, який ініціює процес розрядки ядерних довгоживучих ($\sim 1 \div 1000$ нс) станів ядер, які збуджуються як у непржному розсіянні, так і у резонансному захваті. Реєстрація гамма-квантів розрядки призводить до зростання лічильної ефективності детектора. Спостережуване зростання лічильної ефективності вторинних гамма-квантів реалізується при уповільненні нейтронів в оксидних детекторах товщиною 40–50 мм і більше. Похибка вимірювань ефективності реєстрації нейтронів складала 7 %.

КЛЮЧОВІ СЛОВА: детектор, швидкі нейтрони, збуджені стани, лічильна ефективність, щільність ядерних рівнів.

East Eur. J. Phys. **3**. 63-70 (2019) DOI:10.26565/2312-4334-2019-3-08

PACS: 87.14.C++c, 87.16.Dg

COMPETITIVE BINDING OF NOVEL CYANINE DYE AK3-5 AND EUROPIUM COORDINATION COMPLEXES TO DNA

Olga Zhytniakivska[1]*, Anna Zabrudska[1], Uliana Tarabara[1], Kateryna Vus[1], Valeriya Trusova[1], Galyna Gorbenko[1], Atanas Kurutos[2], Todor Deligeorgiev[3]

[1]Department of Nuclear and Medical Physics, V.N. Karazin Kharkiv National University
4, Svobody Sq., Kharkiv, 61022, Ukraine
[3]Institute of Organic Chemistry with Centre of Phytochemistry, Bulgarian Academy of Sciences,
9, blv. Acad. G. Bonchev, Sofia, 1113, Bulgaria
[3]Faculty of Chemistry and Pharmacy, Sofia University ''St. Kliment Ohridski''
1, blv. J. Bourchier, Sofia, 1164, Bulgaria
**E-mail: olya_zhitniakivska@yahoo.com*
Received 15 April 2019, revised May 5, 2019; accepted May 8, 2019

The present study was undertaken to assess the applicability of the novel trimethine cyanine dye AK3-5 as a competitive ligand for the antitumor agents, Eu(III) coordination complexes (EC), in the DNA-containing systems, using the displacement assay as an analytical instrument. The analysis of fluorescence spectra revealed a strong association of AK3-5 with nucleic acids, with the strength of interaction being higher for the double stranded DNA, compared to the single-stranded RNA. The binding parameters of the cyanine dye have been determined in terms of the McGhee & von Hippel neighbouring site-exclusion model and a classical Langmuir model. The AK3-5 association constant in the presence of DNA was found to be equal to 5.1×10^4 M^{-1}, which is consistent to those of the well-known DNA intercalators. In turn, the binding of the cyanine to the RNA was characterized by a significantly lower association constant (~ 3.4×10^3 M^{-1}) indicating either the external or "partially intercalated" binding mode. The addition of the europium complexes to the AK3-5-DNA system was followed by the fluorescence intensity decrease, with a magnitude of this effect being dependent on the EC structure. The observed fluorescence decrease of AK3-5 in the presence of europium complexes V7 and V9 points to the competition between the cyanine dye and antitumor drugs for the DNA binding sites. The dependencies of the AK3-5-DNA fluorescence intensity decrease *vs*. europium complex concentration were analyzed in terms of the Langmuir adsorption model, giving the values of the drug association constant equal to 5.4×10^4 $M^{-1}$and 3.9×10^5 M^{-1} for the europium complexes V7 and V9, respectively. A more pronounced decrease of the AK3-5 fluorescence in the presence of V5 and V10 was interpreted in terms of the drug-induced quenching of the dye fluorescence, accompanying the competition between AK3-5 and Eu(III) complexes for the DNA binding sites. Cumulatively, the results presented here strongly suggest that AK3-5 can be effectively used in the nucleic acid studies and in the dye-drug displacement assays.
KEYWORDS: trimethine cyanine dye, europium coordination complexes, antitumor drug, DNA, association constant

Over the past decade significant research efforts have been devoted to the investigation of the interaction between drugs and nucleic acids, since DNA was found to serve as a prime target for various anticancer drugs and antibiotics [1-3]. A variety of powerful techniques, including an agarose gel based assay, circular dichroism, mass spectrometry, differential scanning calorimetry, surface plasmon resonance, electrophoresis, high-performance or thin-layer chromatography, Raman, fluorescence and absorption spectroscopy, are currently used to monitor the drug-nucleic acid binding. Due to advantages of rapidity and sensitivity, the fluorescence drug displacement assay seems to be an especially promising for the investigation of mechanisms underlying the interaction between nucleic acids and drugs. This method is based on a strong enhancement in the dye emission upon its binding to DNA or RNA, followed by the fluorescence drop upon the dye displacement by the drug [4-7]. Among a variety of commercially available dyes, ethidium bromide is the most widely used in the displacement experiments [7,8]. However, the applicability of ethidium bromide, which is considered as mutagenic and carcinogenic, is complicated by some environmental concerns [9]. Recent studies revealed that cyanine dyes can be effectively used for the high throughput screening of the drug-DNA interactions [10,11]. The applicability of this class of fluorophores is based on the fact that they display a high affinity for nucleic acid double strands and a huge emission enhancement upon DNA binding. A sharp fluorescence increase is supposed to originate from the loss of mobility around the methane bridge between the two heterocyclic moieties as a result of the cyanine-nucleic acid interaction [12]. Due to their excellent staining properties, cyanine dyes are characterized by a wide scope of applications and have been extensively used for sizing and purification of DNA fragments [13,14], fluorescent microscopy [15], DNA damage detection [12], DNA sequencing [16], as well as for the DNA and RNA bioanalytical assays [17,18].

Our previous studies revealed that the novel mono- and pentamethine cyanine compounds can be effectively employed as non-covalent labels for nucleic acids [17, 19, 20]. As a next logical step, herein we directed our efforts towards evaluating the DNA- and RNA-binding ability of the novel trimethine cyanine dye with an emphasis on its use in the drug-displacement studies. More specifically, the aims of the present study were: i) to investigate the sensitivity of the novel trimethine cyanine, referred to here as AK3-5, to the double stranded DNA and single stranded RNA; ii) to estimate the parameters of the cyanine association with nucleic acids; iii) to analyze the binding mode of the novel dye;

iv) to assess the applicability of AK3-5 as a competitive ligand for pharmacological agents, represented here by the novel antitumor compounds, europium coordination complexes.

EXPERIMENTAL SECTION

Materials

Calf thymus DNA and yeast RNA were from Sigma (Sigma, St. Louis, MO, USA). Trimethine cyanine dye AK3-5 [21] and Eu(III) coordination complexes (Fig.1) referred to here as V7, V9 and V10 were synthesized in the University of Sofia, Bulgaria, as described previously [2]. All other materials and solvents were commercial products of analytical grade and were used without further purification.

Preparation of working solutions

The stock solutions of AK3-5 and Eu(III) coordination complexes were prepared in dimethyl sulfoxide. The concentrations of the compounds were determined spectrophotometrically using their molar extinction coefficients (ε) at absorption maxima (λ_{abs}), which are presented in Table 1. The solutions of calf thymus DNA and yeast RNA were prepared in 5 mM sodium phosphate buffer (pH 7.4) at room temperature with occasional stirring to ensure the formation of a homogenous solution. The concentrations of DNA and RNA solutions were determined using their molar absorptivities $\varepsilon_{260} = 6.6\times10^3\,\mathrm{M^{-1}cm^{-1}}$ and $\varepsilon_{260} = 6.9\times10^3\,\mathrm{M^{-1}cm^{-1}}$, respectively.

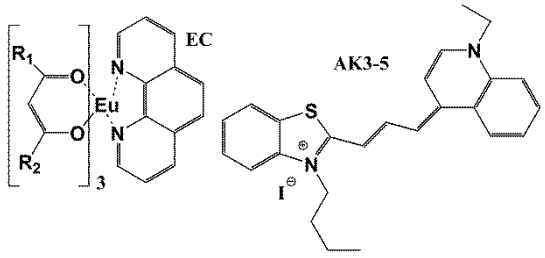

Fig.1. Structures of the AK3-5 and EC

Table 1

Chemical structures and photophysical properties of europium coordination complexes and AK3-5

compound	R_1	R_2	ε, $M^{-1}cm^{-1}$	λ_{abs}, nm
V5	C_6H_5	CH_3	2.6×10^4	266
V7	C_6H_5	CF_3	2.6×10^4	266
V9	C_6H_7O	CF_3	3.4×10^4	271
V10	C_6H_5	C_6H_5	3.4×10^4	167
AK3-5			1.5×10^5	631

Spectroscopic measurements

The steady-state fluorescence spectra were recorded with LS-55 spectrofluorimeter (Perkin-Elmer Ltd., Beaconsfield, UK) at 20°C using 10 mm path-length quartz cuvettes. To measure the fluorescence spectra of the AK3-5-DNA/RNA complexes, the appropriate amounts of the nucleic acid stock solution were added to the dye in 5 mM sodium phosphate buffer, pH 7.4. The fluorescence spectra of AK3-5 were recorded in the range 620 - 800 nm upon excitation at 600 nm. The fluorimetric titrations were carried out by keeping the dye concentration constant at varying the DNA and RNA concentrations. In the case of the dye displacement studies, a solution containing AK3-5 and DNA was titrated with the Eu(III) complexes.

Quantitative analysis of the dye-nucleic acid interactions

The thermodynamic analysis of the cyanine-nucleic acid interactions was performed in terms of the McGhee & von Hippel excluded site model allowing the calculation of the binding constant and stoichiometry [22]:

$$\frac{B}{F}=K_aP\left(1-\frac{nB}{P}\right)\left[\frac{1-(nB/P)}{1-(n-1)(nB/P)}\right]^{n-1}, \quad (1)$$

where B and F are the concentrations of the bound and free dye, respectively, P is the DNA (RNA) phosphate concentration, K_a denotes the association constant, and n represents the site exclusion parameter (i.e. the number of base pairs excluded by the binding of a single ligand molecule). The values of K_a and n were estimated using the nonlinear least-square fitting procedure.

Quantitative analysis of the AK3-5/ EC competitive binding

In order to analyse the competitive binding of AK3-5 and EC to the nucleic acids a simplified model based on the one-site Langmuir adsorption model was employed [23,24]. Assuming that the AK3-5 fluorescence response is proportional to the amount of the DNA-bound fluorophore, B, the DNA-induced change in the probe fluorescence intensity ΔF at the fluorescence maximum can be written as:

$$\Delta F = F - F_0 = \alpha_{bound}B + \alpha_{free}(Z - B) - \alpha_{free}Z = (\alpha_{bound} - \alpha_{free})B = F_{mol}B, \quad (2)$$

where F_0 and F are the fluorescence intensities of the dye in a buffer solution and in the presence of DNA, respectively; F_{mol} is a coefficient proportional to the difference of the dye quantum yields in buffer and when bound to a macromolecule; α_{bound} and α_{free} are the molar fluorescences of the bound and free dye, respectively.

Given that the number of phosphates bound to one dye molecule is n, the association constant (K_a) can be represented as:

$$K_a = \frac{B}{(Z-B)(P/n-B)} = \frac{B}{F(P/n-B)}, \tag{3}$$

where P and Z are total phosphate and total dye concentrations, respectively.

The F_{mol} parameter was calculated from the fluorimetric titration of the dye with the DNA or RNA. Specifically, at high DNA/RNA concentrations, when $P/n \gg B$, from the combination of eqns (2) and (3) one obtains:

$$\frac{1}{\Delta F} = \frac{1}{BF_{mol}} = \frac{1}{K_a PZF_{mol}/n} + \frac{1}{ZF_{mol}}, \tag{4}$$

$$F_{mol} = 1/aZ, \tag{5}$$

where a is the y-intercept of the linear fit of the plot $1/\Delta F(1/P)$ [23].

The parameters K_a and n were estimated from the fluorimetric titration of the DNA by the dye. In this case, when $Z \gg B$, a combination of the eqns (2) and (3) gives:

$$\frac{1}{\Delta F} = \frac{1}{BF_{mol}} = \frac{1}{K_a PZF_{mol}/n} + \frac{1}{PF_{mol}/n}, \tag{6}$$

$$n = bPF_{mol}, \tag{7}$$

$$K_a = -c, \tag{8}$$

where b and c are y- and x-intercepts of the linear fit of the plot $1/\Delta F(1/Z)$. When the drug binds to the AK3-5-DNA complexes, the dye fluorescence in the absence (F_0) and presence (F_i^{corr}) of the drug can be written as:

$$F_0 = B_0 a_{bound} + (Z_0 - B_0) a_{free}, \tag{9}$$

$$F_i^{corr} = B_i a_{bound} + (Z_0 - B_0) a_{free}, \tag{10}$$

where B_0 and B_i are the concentrations of the DNA-bound dye in the absence and presence of a drug, respectively. From the eqns. (9) and (10) one obtains:

$$\Delta F_{calc} = F_0 - F_i^{corr} = (B_0 - B_i)(a_{bound} - a_{free}). \tag{11}$$

The association constants of the dye (K_{dye}) and drug (K_{drug}) binding to the DNA were recovered from the numerical solution of the set of equations under the following conditions: $B_{dye} \le Z_{0\,dye}$; $B_{drug} \le Z_{0\,drug}$; $B_{dye} > 0$; $B_{drug} > 0$; $B_{dye} < N - B_{drug}$ (the total number of binding sites $N = P/n$ is greater than the sum of concentrations of bound dye and drug):

$$K_{dye} = \frac{B_{dye}}{(Z_{0\,dye} - B_{dye})(N - B_{dye} - B_{drug})}, \tag{12}$$

$$K_{drug} = \frac{B_{drug}}{(Z_{0\,drug} - B_{drug})(N - B_{dye} - B_{drug})}, \tag{13}$$

where B_{dye} and B_{drug} are the concentrations of the DNA-bound dye and drug, respectively.

Molecular docking

An interactive molecular graphics program, Hex 8.0.0 was used to study the interaction between the examined europium complexes and the double stranded DNA. The program performs docking using the spherical polar Fourier correlations with the inputs of ligand and receptor in PDB format. The structure of the B-DNA dodecamer d(CGCGAATTCGCG)$_2$ (PDB ID: 1BNA) was downloaded from the Protein Data Bank (http://www.rcsb.org./pdb). The parameters used for molecular docking include: FFT mode – 3D, correlation type – shape only, grid dimension – 0.6, ligand range – 180, receptor range – 180, distance range – 40, and twist range – 360. The docked complexes were visualized by the Visual Molecular Dynamics (VMD) software.

RESULTS AND DISCUSSION

At the first step of the study the AK3-5-nucleic acid binding was characterized using the fluorescence spectroscopy technique. The spectra of AK3-5 in the presence of the double stranded DNA or single stranded RNA are presented in Fig.2. The AK3-5 was found to have a negligible fluorescence in a buffer solution with the emission maximum at 640 nm. In turn, the fluorescence intensity drastically increased upon the dye transfer from the aqueous phase to the dsDNA or RNA environment, with the magnitude of this effect being more pronounced for the dye-DNA complex. Moreover, AK3-5 binding to the RNA caused a 10 nm bathochromic shift in the emission maxima position, whereas no significant change of this parameter was observed in the dye-DNA system. The comparison of the extents of fluorescence enhancement in the presence of the dsDNA (*ca.* ~42.3) and the RNA (*ca.* ~4.3) at the same experimental conditions indicates that the affinity of the AK3-5 to double stranded nucleic acids is higher than that of single stranded one. The difference in the position of the fluorescence maxima in the presence of nucleic acids, as well as different affinities for the RNA and DNA were also reported previously for other dyes of cyanine family [25], and can be used to distinguish between the double and single stranded nucleic acids in solution. Moreover, the 10 nm shift of the AK3-5 fluorescence maximum position in the presence of the RNA with respect to that in the DNA-containing system probably reflects a more polar environment of the dye in a single stranded nucleic acid. This finding is suggestive of the different binding modes of AK3-5 to the single and double stranded nucleic acids.

It is well-known that cyanine dyes can interact with the nucleic acids in the three basic modes: i) electrostatic attraction between the cationic dyes and the anionic phosphodiester groups of DNA/RNA backbone; ii) intercalation between adjacent base pairs, iii) minor groove binding. Intercalation is typically observed for the cationic molecules (with the positive charge preferably located on the ring system) possessing a planar aromatic structure, while the minor groove binders should have at least limited flexibility to be able to adjust to the groove [12]. The structural and physicochemical properties of a fluorophore, a nucleic acid sequence, as well as the phosphate to dye ratio (P/D) were found to determine the molecular mechanism of cyanine complexation with nucleic acid [26,27].

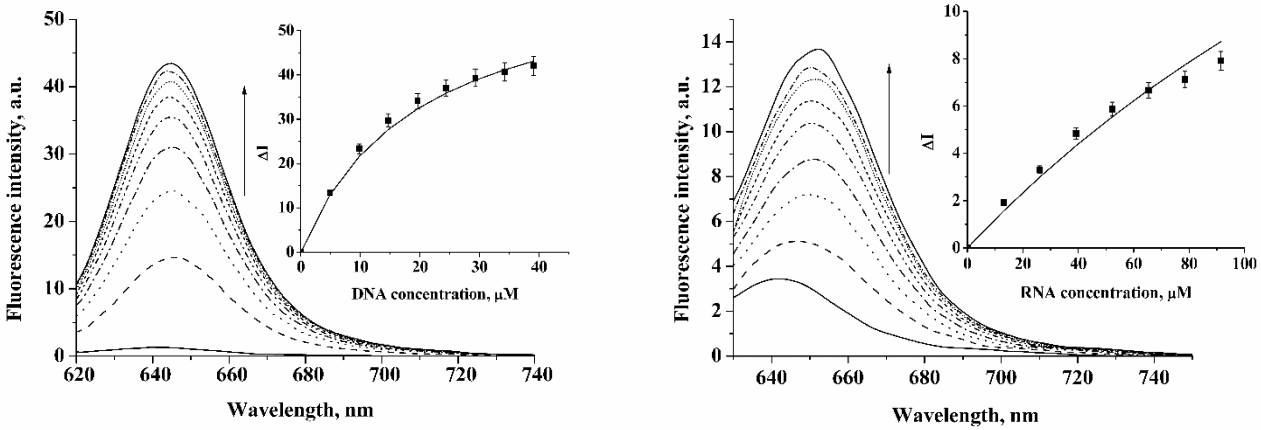

Fig. 2. Fluorescence spectra of the cyanine dye AK3-5 in the presence of increasing concentration of the double stranded DNA (left) and the single stranded RNA (right). Dye concentration was 0.25 μM. DNA concentrations from bottom to top were 0 μM, 4.9 μM, 9.8 μM, 14.7 μM, 19.6 μM, 24.4 μM, 29.3 μM, 34.2 μM, and 39.1 μM, respectively. RNA concentrations from bottom to top were 0 μM, 13.1 μM, 26.2 μM, 39.2 μM, 52.3 μM, 65.4 μM, 78.3 μM, 91.5 μM, and 104.6 μM, respectively. The insets show the isotherms of the dye binding to the DNA or RNA. The experimental data were fitted with the McGhee-von Hippel model.

In order to gain further insight into the binding mode between the AK3-5 and nucleic acids, as well as to calculate the parameters characterizing the stability of the cyanine-nucleic acid complexes, the experimental dependencies of the dye fluorescence increase (ΔI) on the DNA/RNA concentration (insets in Fig. 2) were analyzed in terms of the non-cooperative McGhee & von Hippel model (Eq. (1)) [22]. The results obtained are summarized in Table 2.

Table 2.

The thermodynamic parameters of the AK3-5 binding to nucleic acid

Nucleic acid	$K_a \times 10^4\ M^{-1}$	n	$F_{mol}, \mu M^{-1}$
DNA	5.1±0.9	2	264.3±52.8
RNA	0.34±0.06	2	142.6±29.6

The association constant for the AK3-5-DNA complex was found to be 5.1×10^4 M^{-1}. This value is identical to the association constant observed for the classical intercalating dye, acridine orange [28]. The association constants for other fluorophores possessing intercalating binding mode such as ethidium bromide (~ 1.5×10^5 M^{-1}) [29], EvaGreen

(~ 3.6×10^5 M^{-1}) [30], asymmetric thiazole orange derivatives (0.7 – 7.6×10^5 M^{-1}) [17] and monomethine cyanine dyes [19] do not exceed 10^5 M^{-1}. In view of this, we can suppose that AK3-5 also intercalates between the base pairs of the double stranded DNA. An additional argument in favor of the above assumption comes from the fact that the site exclusion parameter (number of DNA units excluded by the cyanine molecule, n) is equal to 2, that is in a good agreement with the principle of the nearest neighbor exclusion, indicating that the binding of one intercalating molecule between two base pairs hinders an access of the next binding site to another intercalator, so the highest possible dye-base pair ratio for intercalation is 1:2 [12]. As seen in Table 2, the value of association constant for the AK3-5/RNA complex was smaller by an order of magnitude, while the site exclusion parameter was also equal to two. These parameters allowed us to rule out the possibility of AK3-5 binding to the minor groove of RNA and, therefore, we supposed that the AK3-5 binding to the single stranded RNA is presumably driven by the electrostatic attraction between the positively charged group of the dye and negatively charged phosphate backbone. Nevertheless, the possibility of a "partial" intercalation of the AK3-5 between the RNA bases cannot be ruled out. Such a binding mode was previously observed for acridine orange in the presence of ss-nucleic acids [28]. Similarly, the alkaloids berberine and palmatine, which are capable of intercalating between the base pairs of dsDNA, changed their binding mode to the partially intercalating in the presence of tRNA [31].

At the next step of the study an attempt has been made to assess the applicability of the trimethine cyanine dye AK3-5 as a competitive ligand for the potential pharmacological agents Eu(III) tris-β-diketonato coordination complexes. Notably, due to a significantly smaller binding affinity of the AK3-5 to the single stranded RNA, the dye displacement data were quantitatively interpreted only for AK3-5-DNA systems. It is generally accepted that in the competitive displacement assays drug molecules that displace the DNA-bound dye, interact with the DNA in a fashion similar to that of the dye [32]. Such a competition between dye and drug usually manifests itself in a fluorescence intensity decrease of the dye-DNA complex. Recently it has been demonstrated that a series of europium coordination complexes are capable of exerting significant antineoplastic effect, with the abundance of DNA-intercalating motif being the major determinant of cytotoxicity [2]. To confirm that Eu(III) compounds under investigation are capable of intercalating within the DNA helix, the molecular docking studies were performed. A double-stranded DNA dodecamer [PDB ID 1BNA] and the examined drugs were taken as the input structures. The molecular docking indicates that a more energetically favorable binding mode for the EC is a "partial intercalation" (Fig. 3). The 1,10-phenanthroline or 2,2'bipyridine part of the Eu(III) molecule tends to reside between the DNA-bases, while the rest of the complex is placed in the minor groove of the DNA.

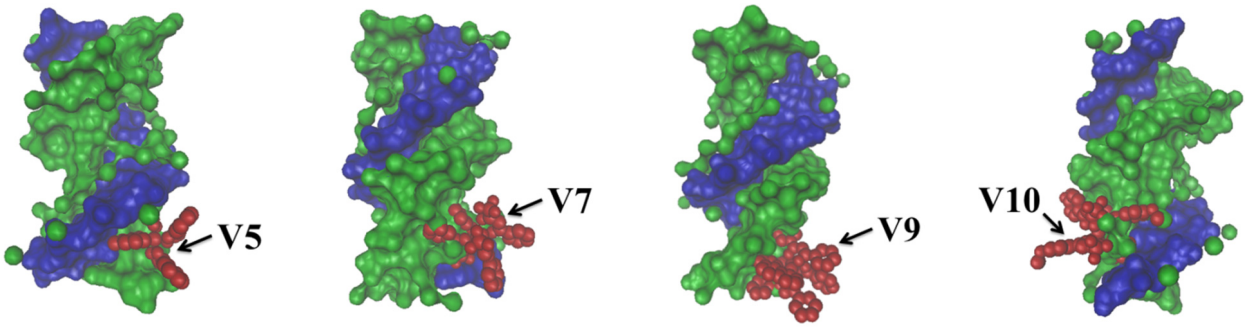

Fig. 3. Schematic representation of the energetically most favourable EC complexes with the double stranded DNA.

Thus, it might be expected that EC as intercalating molecules would replace the AK3-5 from the DNA helix. Fig. 4 shows the emission spectra of the DNA-bound AK3-5 in the absence and presence of europium coordination complexes. As can be seen, increase of the EC concentration was followed by a gradual reduction in the AK3-5 fluorescence intensity, indicating that europium compounds are capable of displacing the AK3-5 from the DNA helix. Notably, the magnitude of the fluorescence intensity decrease was more pronounced for V5 and V10 complexes in comparison to V7 and V9. The most probable explanation for this observation is the different binding affinities of the europium complexes. Similarly, the metal complexes of Cu, Zn and Ni have been reported to possess the distinct DNA binding affinities [5]. Interestingly, V5 and V10 are more bulky in comparison to V7 and V9. So we cannot exclude the possibility of the EC- induced conformational changes in the double stranded DNA. A good wealth of reports indicates that the drug binding to the right-handed B-DNA can produce its conversion to the left-handed Z-DNA [11].

Pursuing a comprehensive picture of the competition between AK3-5 and Eu(III) compounds for the DNA binding sites, our experimental strategy involved collecting the multiple data sets. More specifically, the AK3-5 fluorescence intensity decrease was measured as a function of EC concentration upon simultaneous varying the DNA concentrations. The plots of the fluorescence intensity decrease *vs* EC concentration are presented in Fig.5.

The above dependencies were analyzed in terms of the simplified competition model (Eqs. 2-13) to calculate the association constants of the drug (K_{drug}) binding to the DNA in the presence of AK3-5. The calculated K_{drug} values were equal to 5.4×10^4 $M^{-1}$and 3.9×10^5 M^{-1} for V7 and V9, respectively. Moreover, the association constants of the drug were found to be independent of the DNA concentration in the tested sample.

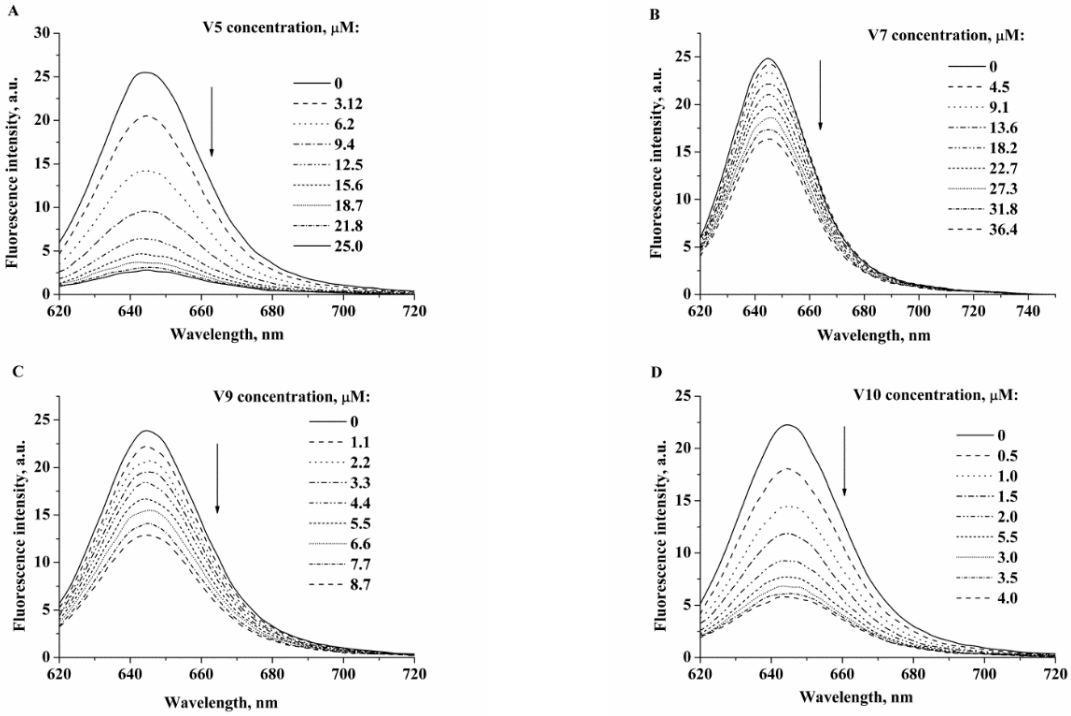

Fig. 4. Competitive displacement assays between the AK3-5 and V5(A), V7(B), V9(C) and V10 (D) in the presence of DNA. Dye concentration was 0.25 μM. DNA concentration was 9.3 μM.

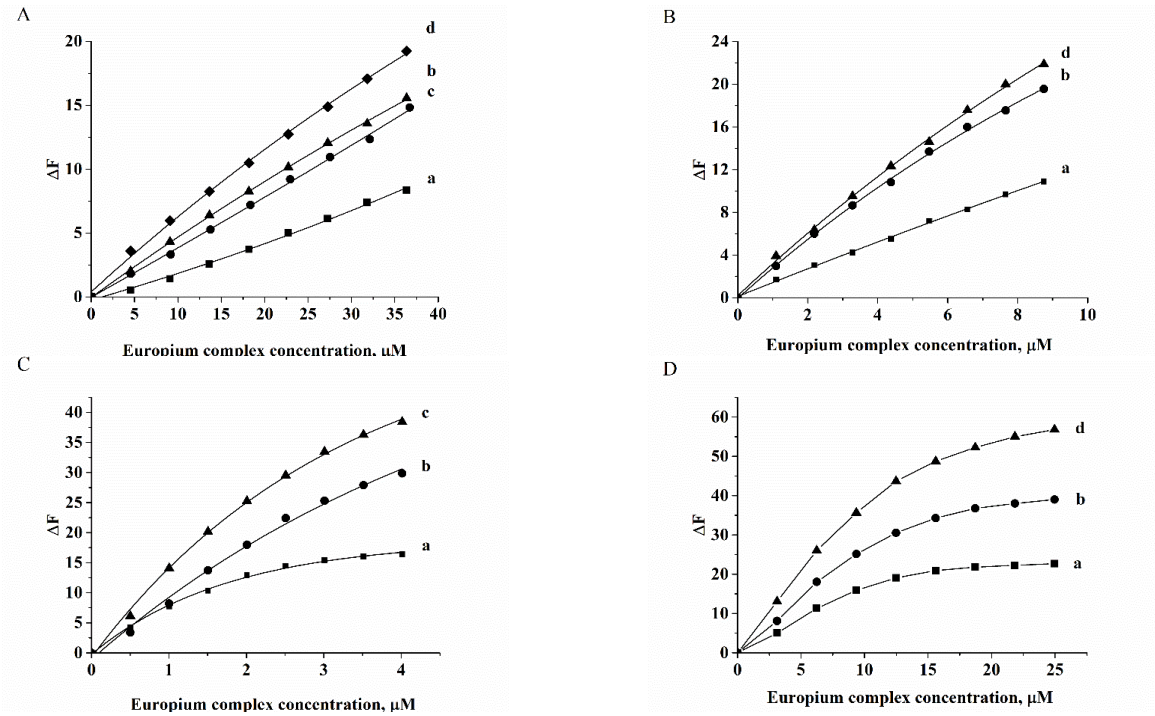

Fig.5. The fluorescence intensity decreases of AK3-5-DNA complexes in the presence of the increasing concentrations of V7 (A), V9 (B), V10 (C) and V5 (D). The concentrations of the DNA were (a) 9.3 μM, (b) 27.9 μM, (c) 37.6 μM, (d) 46.5 μM, respectively.

However, we failed to obtain the realistic value of the association constant K_{drug} for the europium complexes V5 and V10. Moreover, the theoretically calculated ΔF values (eq. 11) were significantly greater than those obtained from the experiment. Most likely, the competition between AK3/5 and Eu(III) complexes for the DNA binding sites is not the only reason for the observed fluorescence decrease in the presence of V5 and V10. In this respect, it seems of interest to draw attention to the shapes of the dependencies of ΔF on the EC concentration: being linear for the V7 and V9, it is almost hyperbolic for V5 and V10. The most probable reason for such a behavior is that besides the competition

between AK3/5 and EC for the DNA binding sites, V5 and V10 are capable of quenching the AK3-5 fluorescence. A more hydrophobic nature of V5 and V10 in comparison to V7 and V9 seems to account for a pronounced drop in the AK3-5 fluorescence intensity in the combined AK3-5/DNA/EC systems [33].

CONCLUSIONS

In conclusion, the present study was focused on the possible application of the novel trimethine cyanine dye AK3-5 in the displacement assay using the potential antitumor agents, europium coordination complexes as competitive ligands. The AK3-5-DNA/RNA binding studies provided evidence for the strong association of the fluorophore to nucleic acids, with the binding affinity being higher for the double-stranded DNA, in comparison with the single-stranded RNA. Upon addition of increasing concentrations of europium complexes, a gradual reduction in the fluorescence intensity of the dye was observed, indicating that EC are capable of displacing the AK3-5 from the DNA helix. The magnitude of the fluorescence intensity decrease was found to be more pronounced for V5 and V10 compared to V7 and V9. The observed effects were interpreted in terms of the different binding affinities of the europium complexes to the DNA. The assumption was made, that a more pronounced fluorescence intensity decrease of in the presence of V5 and V10 results from the EC ability to quench the AK3-5 fluorescence, along with the competition between AK3/5 and Eu(III) complexes for the DNA binding sites. Cumulatively, the results presented here strongly suggest that AK3-5 can be effectively used for the sensitive detection of the nucleic acids, as well as for the drug displacement assays.

ACKNOWLEDGEMENTS

This work was supported by the Ministry of Education and Science of Ukraine (the Young Scientist project № 0117U004966 “Nano- and microsized liophilic and liophilized self-associated systems: application in modern technologies and biomedicine”) and by the President’s of Ukraine grant No 0118U002284 from the State Fund for Fundamental Research of Ukraine “Development of novel anti-amyloid strategies by high-throughput screening of inhibitors of pathological protein aggregation”.

ORCID IDs

Olga Zhytniakivska https://orcid.org/0000-0001-9554-0090, **Anna Zabrudska** https://orcid.org/0000-0002-3611-8188,
Uliana Tarabara https://orcid.org/0000-0002-7677-0779, **Kateryna Vus** http://orcid.org/0000-0003-4738-4016,
Valeriya Trusova https://orcid.org/0000-0002-7087-071X, **Galyna Gorbenko** http://orcid.org/0000-0002-0954-5053,
Atanas Kurutos https://orcid.org/0000-0002-6847-198X

REFERENCES

[1] S.F. Cui, Y. Ren, S.L. Zhang, X.M. Peng, G.L. Damu, R.X. Geng and C.H. Zhou, Bioorg. Med. Chem. Lett. **23**, 3267–3272 (2013).
[2] G. Momekov, T. Deligeorgiev, A. Vasilev, K. Peneva, S. Konstantinov and M. Karaivanova, Med. Chem. **2**, 439–445 (2006).
[3] A. Opar, Nat. Rev. Drug Discov., **8**, 437–438 (2009).
[4] K. Qumaizi, R. Anwer, N. Ahmad and S. Alosaimi, J. Mol. Recognit. **31**, 2735–2745 (2018).
[5] M. Anjomshoa and M. Torkzadeh-Mahani, J. Fluoresc. **26**, 1505–1510 (2016).
[6] M. A. Husain, H. M. Ishqi, T. Sarwar, S.U. Rehman and M. Tabish, Med. Chem. Comm. **8**, 1283–1296 (2017).
[7] W.S. Tse and D. Boger, Acc. Chem. Res. **37**, 61–69 (2004).
[8] J. Szekely and K.S. Gates, Chem. Res. Toxicol. **19**, 117–121 (2006).
[9] P. Cerutti, Science. **227**, 375–381 (1985).
[10] K.E. Achyuthan and D.G. Whitten, Comb. Chem. High. Throughput Screen. **10**, 399–412 (2007).
[11] K.E. Achyuthan, D.G. Whitten and D.W. Branch, Anal. Sci. **26**, 55–61 (2010).
[12] B. Armitage, Topp. Curr. Chem. **253**, 55-76 (2005).
[13] H. Rye, S. Yue, D. Wemmer, M. Quesada, P. Haugland, R. Mathies and A. Glazer, Nucleic Acid Res. **20**, 2803-2812 (1992).
[14] X. Yan, W. Grace, T. Yoshida, R. Habbersett, N. Velappan, J. Jett, R. Keller and B. Marrone, Anal. Chem. **71**, 5470-5480 (1999).
[15] S. Gurrieri, K. Wells, I. Johnson and C. Bustamente, Anal. Biochem. **249**, 44-53 (1997).
[16] T. Biver, A. Boggioni, F, Secco, E. Turriani, S. Venturini and S. Yarmoluk, Arch. Biochem. Biophys. **465**, 90-100 (2007).
[17] S. Kaloyanova, V. Trusova, G. Gorbenko and T. Deligeorgiev, J. Photochem. Photobiol. A. **217**, 147-156 (2011).
[18] L. Glavas-Obrovac, I. Piantanida, S. Marczi, L. Masic, I. Timcheva and T. Deligeorgiev, Bioorg. Med. Chem. **17**, 4747-4755 (2009).
[19] A. Kurutos, O. Ryzhova, V. Trusova, U. Tarabara, G. Gorbenko, N. Gadjev and T. Deligeorgiev, Dyes and Pigments. **130**, 122-128 (2016).
[20] A. Kurutos, O. Ryzhova, V. Trusova, G. Gorbenko, N. Gadjev and T. Deligeorgiev. J. Fluoresc. **26**, 177-187 (2015).
[21] A. Kurutos, I. Crnolatac, I. Orehovec, N. Gadjev, I. Piantanida and T. Deligeorgiev, J. Liminescence. **174**, 70-76 (2016).
[22] J. Petty and M. Bordelon, J. Phys. Chem. B. **1041**, 7221-7227 (2000).
[23] H. LeVine, Protein Sci. **2**, 404-410 (1993).
[24] K.D. Volkova, V.B. Kovalska, A.O. Balanda, M.Y. Losytskyy, A.G. Golub, R.J. Vermeij, V. Subramaniam, O.I. Tolmachev and S.M. Yarmoluk, Bioorg. Med. Chem. **16**, 1452-1459 (2008).
[25] I.I. Timcheva, V.A. Maximova, T.G. Deligeorgiev, N.I. Gadjev, R.W. Sabnis and I.G. Ivanov, FEBS Lett. **405**, 141-141 (1997).
[26] J. Nygren, N. Svanvik and M. Kubista, Biopolymers. **46**, 39-51 (1998).

[27] K.M. Sovenyhazy, J.A. Bordelon and J.T. Petty, Nucleic Acids Res. **31**, 2561-2569 (2003).
[28] J. Kapuscinski, Z. Darzynkiewicz and M. Melamed, Biochem. Pharmacol. **32**, 3679-3694 (2008).
[29] H. Rye, M. Quesada, K. Peck, R. Mathies and A. Glazer, Nucleic Acid Res. **19**, 327-333 (1991).
[30] L.C.T. Shoute and G.R. Loppnow, Phys. Chem. Chem. Phys. **20**, 4772-4780 (2018).
[31] M.M. Islam, P. Pandya, S.R. Chowdhury, S. Kumar and G.S. Kumar, J. Mol. Struct. **891**, 498-507 (2008).
[32] H.K. Liu and P.J. Sadler, Acc. Chem. Res. **44**, 349-359 (2011).
[33] V. Trusova, A. Yudintsev, L. Limanskaya, G. Gorbenko and T. Deligeorgiev, J. Fluoresc. **23**, 193-202 (2013).

КОНКУРЕНТНЕ ЗВ'ЯЗУВАННЯ НОВОГО ЦІАНІНОВОГО БАРВНИКА АК3-5 ТА КООРДИНАЦІЙНИХ КОМПЛЕКСІВ ЄВРОПІЮ З ДНК

О. Житняківська[1], А. Забрудська[1], У. Тарабара[1], К. Вус[1], В. Трусова[1], Г. Горбенко[1], А. Курутос[2], Т. Делігеоргієв[3]
[1]Кафедра ядерної та медичної фізики, Харківський національний університет імені В.Н. Каразіна
м. Свободи 4, Харків, 61022, Україна
[2]Інститут органічної хімії та біохімії рослин, Болгарська академія наук
Софія, 1113, Болгарія
[3]Факультет хімії і фармації, Софійський університет «Святий Клімент Охридський»
Софія, 1164, Болгарія

У даній роботі проведено оцінку можливості використання нового триметинового барвника АК3-5 в якості конкурентного ліганду для протипухлинних препаратів, координаційних комплексів європію (ККЄ), у системах, що містили ДНК. Аналіз спектрів флуоресценції показав високу спорідненість АК3-5 до нуклеїнових кислот, причому ступінь взаємодії з подвійною спіраллю ДНК був вищий, ніж з одноланцюговою РНК. За допомогою моделі Мак-Гі і фон Хіппеля визначено термодинамічні параметри зв'язування ціанінового барвника з нуклеїновими кислотами. Константа асоціації АК3-5 з ДНК дорівнювала 5.1×10^4 M^{-1} , що відповідає значенню цього параметру для відомих ДНК інтеркаляторів. Зв'язування ціанінового зонда з РНК, у свою чергу, характеризувалось значно меншою константою асоціації ~ 3.4×10^3 M^{-1}, що вказує на електростатичне зв'язування або «часткову інтеркаляцію» як можливий механізм комплексоутворення. Додавання комплексів європію до системи АК3-5 – ДНК супроводжувалось падінням інтенсивності флуоресценції, причому величина цього ефекту залежала від структури ККЄ. Зменшення флуоресценції АК3-5, що спостерігалось у присутності комплексів європію V7 і V9, найімовірніше, вказує на конкуренцію між ціаніновим барвником і протипухлинними препаратами за сайти зв'язування з ДНК. Концентраційні залежності змін інтенсивності флуоресценції були проаналізовані в рамках моделі Ленгмюра, що дозволило отримати константи зв'язування 5.4×10^4 M^{-1} та 3.9×10^5 M^{-1} для комплексів європію V7 і V9, відповідно. Більш виражене падіння інтенсивності флуоресценції барвника у присутності V5 і V10, імовірно, свідчить про гасіння флуоресценції АК3-5 комплексами європію, окрім конкуренції між барвником та ККЄ за сайти зв'язування на ДНК, В цілому, отримані результати створюють передумови ефективного використання АК3-5 у дослідженнях нуклеїнових кислот та конкурентних взаємодій фармакологічних агентів і барвників з ДНК.

КЛЮЧОВІ СЛОВА: Триметиновий ціаніновий барвник, координаційні комплекси європію, протипухлинний препарат, ДНК, константа асоціації

КОНКУРЕНТНОЕ СВЯЗЫВАНИЕ НОВОГО ЦИАНИНОВОГО ЗОНДА АК3-5 И КООРДИНАЦИОННЫХ КОМПЛЕКСОВ ЕВРОПИЯ С ДНК

О. Житняковская[1], А. Забрудская[1], У. Тарабара[1], К. Вус[1], В. Трусова[1], Г. Горбенко[1], А. Курутос[2], Т. Делигеоргиев[3]
[1]Кафедра ядерной и медицинской физики, Харьковский национальный университет имени В.Н. Каразина
пл. Свободы 4, Харьков, 61022, Украина
[2]Институт органической химии и биохимии растений, Болгарская академия наук
София, 1113, Болгария
[3]Факультет химии и фармации, Софийский университет «Святой Климент Охридский»
София, 1164, Болгария

В данной работе проведена оценка возможности использования нового триметинового красителя АК3-5 в качестве конкурентного лиганда для противоопухолевых препаратов, координационных комплексов европия (ККЕ), в ДНК-содержащих системах. Анализ флуоресцентных спектров показал высокое сродство АК3-5 к нуклеиновым кислотам, причем степень взаимодействия с двухцепочечной ДНК была выше, чем с одноцепочечной РНК. С помощью модели Мак-Ги и фон Хиппеля определены термодинамические параметры связывания цианинового красителя с нуклеиновыми кислотами. Константа ассоциации АК3-5 с ДНК была равна 5.1×10^4 M^{-1}, что соответствует значению этого параметра для известных ДНК интеркаляторов. Связывание цианинового зонда с РНК, в свою очередь, характеризовалось значительно меньшей константой ассоциации (~ 3.4×10^3 M^{-1}), указывая на электростатическое связывание либо «частичную интеркаляцию» как возможный механизм комплексообразования. Добавление комплексов европия к системе АК3-5 – ДНК сопровождалось снижением интенсивности флуоресценции, причем величина этого эффекта зависела от структуры ККЕ. Наблюдаемое уменьшение флуоресценции АК3-5 в присутствии комплексов европия V7 и V9, наиболее вероятно, указывает на конкуренцию между красителем и противоопухолевыми препаратами за сайты связывания с ДНК. Концентрационные зависимости изменения интенсивности флуоресценции были проанализированы в рамках модели Ленгмюра, что позволило получить константы связывания 5.4×10^4 M^{-1} и 3.9×10^5 M^{-1} для комплексов европия V7 и V9, соответственно. Более выраженное падение интенсивности флуоресценции триметинового красителя в присутствии V5 и V10, предположительно, обусловлено тушением флуоресценции АК3-5 комплексами европия, наряду с конкуренцией между красителем и ККЕ за сайты связывания на ДНК. В целом, представленные результаты создают предпосылки для эффективного использования АК3-5 как для исследования нуклеиновых кислот и конкурентного связывания фармакологических агентов и красителей с ДНК.

КЛЮЧЕВЫЕ СЛОВА: Триметиновый цианиновый краситель, координационные комплексы европия, противоопухолевый препарат, ДНК, константа связывания

East Eur. J. Phys. **3**. 71-80 (2019) DOI:10.26565/2312-4334-2019-3-09

PACS: 61.05.cp, 61.43.Dq, 61.72.Yx, 61.72.Mm, 61.82.Fk, 68.37.Hk, 68.55._a, 85.30.Tv

ELECTRIC DOUBLE LAYER FIELD EFFECT TRANSISTOR USING SnS THIN FILM AS SEMICONDUCTOR CHANNEL LAYER AND HONEY GATE DIELETRIC

Thomas Daniel[1]*, Uno Uno[2], Kasim Isah[3], Umaru Ahmadu[4]
[1]*Department of Physics/Geology/Geophysics, Alex Ekwueme-Federal University Ndufu-Alike Ikwo, P.M.B 1010, Ebonyi state, Nigeria*
[1,2,3,4]*Department of Physics, Federal University of Technology Minna P.M.B 065, Minna, Niger state, Nigeria*
**E-mail: danielojonugwathomas@gmail.com & daniel.thomas@funai.edu.ng*
Received July 24, 2019; revised September 3, 2019; accepted September 26, 2019

The study aimed at the investigation and application of SnS thin film semiconductor as a channel layer semiconductor in the assembly of an electric double layer field effect transistor which is important for the achievement and development of novel device concepts, applications and tuning of physical properties of materials since the reported EDLFET and the modulation of electronic states have so far been realised on oxides, nitrides, carbon nanotubes and organic semiconductor but has been rarely reported for the chalcogenides. Honey was used as a gel like electrolytic gate dielectric to generate an enhanced electric field response over SnS semiconductor channel layer and due to its ability to produces high on-current and low voltage operation while forming an ionic gel-like solution similar to ionic gels which consist of ionic liguids. SnS gated honey Electric double layer field effect transistor was assembled using tin sulphide (SnS) thin film as semiconductor channel layer and honey as gate dielectric. The measured gate capacitance of honey using LCR meter was measured as 2.15 μF/ cm^2 while the dielectric constant is 20.50. The semiconductor layer was deposited using Aerosol assisted chemical vapour deposition and annealed in open air at 250℃ on an etched region about the middle of a 4×4 mm FTO glass substrate with the source and drain electrode region defined by the etching and masking at the two ends of the substrate. Iridium was used as the gate electrode while a copper wire was masked to the source and drain region to create electrode contact. The Profilometry, X-ray diffraction, Scanning electron microscope, Energy dispersive X-ray spectroscopy, Hall Effect measurement and digital multimeters were used to characterise the device. The SnS thin film was found to be polycrystalline consisting of Sn and S elements with define grains, an optical band of 1.42 eV and of 0.4 μm thickness. The transistor operated with a p type channel conductivity in a depletion mode with a field effect mobility of 16.67 cm^2/Vs, cut-off voltage of 1.6 V, Drain saturation current of1.35μA, a transconductance of -809.61 nA/V and a sub threshold slope of -1.6 $Vdec^{-1}$ which is comparable to standard specifications in Electronics Data sheets. Positive gate bias results in a shift in the cut off voltage due to charge trapping in the channel/dielectric interface.
KEY WORDS: SnS thin film; Field effect transistor; Honey; Electric double layer; semiconductor

A transistor is a three terminal semiconductor solid state device used for the amplification and switching of electronic signals. Transistors are classified into bipolar junction transistors (BJT) and the field effect transistors (FET) [1]. The field effect transistor utilises only the majority charge carriers for electrical conduction. The FET consist of a source electrode, drain electrode, gate electrodes and a semiconductor active channel region such that an applied electric field via the gate voltage is used in controlling the channel conductivity with a flow of charge carriers from the source electrode to the drain electrode [2].

An electric double layer may be defined as a nano gap capacitor with a large specific capacitance which on application of low gate voltage can electrostatically modulate the semiconductor channel layer of a field effect transistor by the accumulation of electric charge carriers at the interface between the semiconductor layer and the gate dielectric [3]. An electric double layer field effect transistor (EDLFET) with an advantage of reduce operational voltage due to such a large specific capacitance could be formed from the nano gap electric double layer capacitor by the replaced of one of the capacitor's electrode with a semiconductor material alongside the other electrodes in the capacitors configuration [4].

Electric double layer field effect transistors are of emerging interest in the mimicking of biological synaptic functions, electric control of ferromagnetism, signal processing and sensing in medical physics which requires a low operational voltage and high charge carrier concentrations [5]. The operation of a field effect transistor with a low operating voltage and higher carrier concentration is essentially dependent on the choice of semiconductor channel layer material and the gate dielectric among other parameters since the threshold voltage (V_{th}), which is the voltage required in switching a transistor is dependent on the semiconductor material [3] and also the minimum gate to source voltage differential that is needed to create a charge carrier conducting path between the source and drain is dependent on the semiconductor channel layer in an EDLFET.

However, the reported EDLFET and the modulation of electronic states have been so far realised only on oxides, nitrides, carbon nanotubes and organic semiconductor. Therefore, the application of the electric double layer field effect transistor technique to other semiconductor materials has become one of the emerging interests for novel electronic phenomena. This trend is increasingly important for the achievement and development of novel device concepts, applications and tuning of physical properties of materials [5].

Metal chalcogenides (MX-where M denote metal (usually transition metal) and X denote chalcogen) such as Tin(II) sulphide (SnS) and metal dichalcogenides (MX_2, where M and X denote metal and chalcogen respectively) such as

Tin(IV) sulphide (SnS_2) are of interest as potential candidates for the transport channel of EDLFET. Chalcogenides are materials containing a transition element and one or more chalcogen elements (Silicon, Selenium, Polonium and Tellunum). They found vital applications in solar cells, photoconductive
materials, thermoelectric materials, rewritable memory, studying of dopant induced superconductivity, charge density formation and transistors. SnS is abundance in the earth's crust, SnS is one of the Tin chalcogenides semiconductors, it possess the an orthorhombic crystal structure, it has good air stability, the constituent elements are abundant in nature and not expensive [6], it is not toxic; it is a mostly a p type semiconducting material with carrier concentration on the order of $10^{16}cm^{-3}$, hole mobility of 1.4 $cm^2V^{-1}s^{-1}$ and low resistivity [7]. The SnS is relatively unexplored for application in electric double layer thin film field effect transistor, as existing literatures on the application of SnS thin film as semiconductor channel of an electric double layer field effect transistor is relatively scanty or not available. Hence the SnS thin film is a potential semiconductor to test the feasibility of the chalcogenides as a semiconductor channel layer for application in an electric double layer field effect transistor.

Consequently, the article focuses on the use of SnS as a channel layer in an EDLFET and honey as the gate dielectric. Honey was reported to possess the ability to produces high on-current and low voltage operation while forming an ionic gel-like solution similar to ionic gels which consist of ionic liguids. It has recently shown ideal transistor performance as a electrolytic gate dielectrics in Graphene field effect transistors using liquid metal interconnects [8].

MATERIALS AND METHOD

For the assembling of SnS EDLFET, FTO glass substrate was cleaned using the cleaning methods described as follows: **a.** the substrates were washed in sodium lauryl sulphate (SLS) solution to remove oil and protein. **b.** To remove the organic contaminants, the substrates were immersed in piranha solution (H_2SO_4: H_2O_2 (3:1)) for 30 minutes. **c.** The substrates were then ultrasonically cleaned in distilled water using a sonicator and kept in methanol until it is ready to be used. **d.** Finally, to use the substrate for deposition process, the substrate were taken from the methanol and dried in air at 150℃ after which it was used for the assembling of the SnS EDLFET. A 4×4 mm FTO glass was masked (from both ends to create the drain and source contact respectively) and then etch about the middle using Zinc powder and Hydrochloric acid as the etchant in order to create the semiconductor channel region. A 0.40 μm SnS thin film was deposited on the etch region with a channel length of 70 μm and channel width of 4000 μm by AACVD to serve as the semiconductor channel layer. The SnS semiconductor channel layer was deposited using 0.1 M Tin chloride dehydrates (BDH) and 0.2 M of Thiourea (BDH) which was weighed in stoichiometric proportion and dissolve in ethanol solvent. The two solutions were mixed and stirred for 1 hour using a magnetic stirrer at room temperature, after which the resulting solution was filtered through a 0.22 μm syringe filter and then deposited on the substrate by aerosol assisted chemical vapour deposition (AACVD) at a constant substrate temperature of 258 ℃, nozzle distance of 6.8 mm, substrate to nozzle distance of 3 cm, spray volume of 0.2 mL and spray rate of 0.04 ml/min. With the Drain and Source region still masked, the deposited SnS thin film semiconductor channel layer was annealed in open air at annealing temperature of 250℃ for one hour after which it was allowed to cool to room temperature before undergoing characterisation.

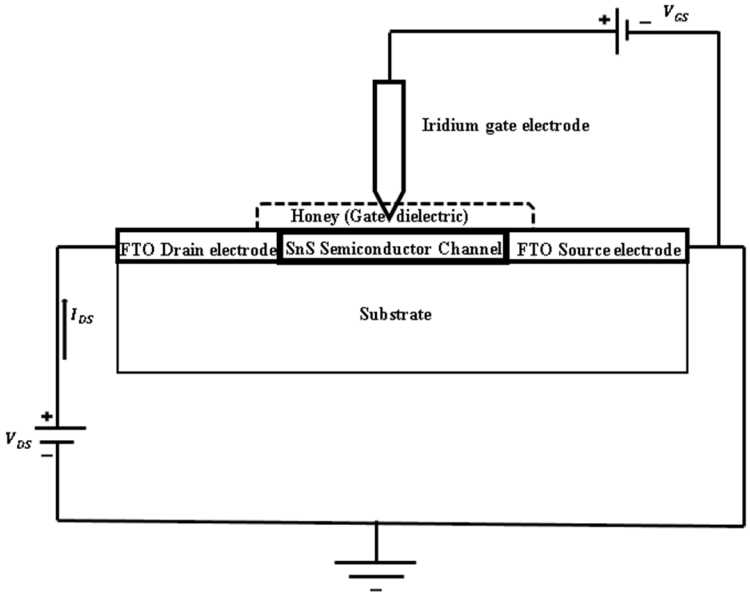

Fig. 1. A schematic diagram of the SnS EDLFET

The FTO drain and source contacts were bonded with a thin copper wire after which Honey which was commercially acquired was dispensed from a plastic dropper at a volume of 150.59 mm^3 and 136.90 mm^2 surface area of the SnS thin film semiconductor channel layer between the source and drain to act as the electrolytic gate dielectric after which an Iridium (Ir) electrode was suspended above the SnS channel layer, but inside the honey gate dielectric to act as the gate electrode. These were all placed in a transparent Glass container. The electric measurements was then carried out at room temperature using two variable power supplies (KOOCU DC Power supply 1502DD with voltage variation of 0-15 V and ATX-650W, hp invent with voltage variation of 0-12 V) and two digital multimeters (CHY VC $890C^+$ digital Multimeter and DT9205ACE digital Multimeter). The V_G applied to the Ir electrode was scanned from 0 to 1 V by 0.2 V step. The quality of the EDLFET was determined by measuring the gate current Ig for a gate voltage Vg. A schematic of the SnS EDLFET is shown in Fig. 1.

CHARACTERISATION TECHNIQUES FOR THE DEPOSITED SNS THIN FILM

The crystal phase analysis was carried out at room temperature using an X-ray diffractrometer (D8 Advance, Bruker AXS, 40Kv, 40 mA) with monochromatic CuKα (λ=1.540598 Å) over a scan mode of step size 0.034˚ and counts accumulated for 192.1 s at each step for 2θ ranging from 20˚ to 80˚. The XRD diffractogram was obtained using Origin Pro 2018 software with the FWHM for the peaks estimated using a Gaussian function. Results was analysed with the scientific graphing analysis software and phase identification was done using the inorganic crystal structure data (ICSD) pattern [9].

The lattice parameters a, b and c value for the orthorhombic crystallographic system of Tin (II) sulphide thin film was calculated from the observed values of 2θ using d values (interplaner spacing) for the orthorhombic structure [10]:

$$1/d^2_{hkl} = h^2/a^2 + k^2/b^2 + l^2/c^2. \quad (1)$$

XRD pattern of the film was first indexed after which three peaks whose (hkl) is known were selected and resolved for a, b and c lattice constants of the SnS thin film which is also equivalent to:
$a = \frac{1}{d_{101}} = \frac{bcsin\alpha}{V}$; $b = \frac{1}{d_{040}} = \frac{acsin\beta}{V}$; $c = \frac{1}{d_{002}} = \frac{absin\gamma}{V}$. Where V (unit cell volume)=abc (for orthorhombic), d is the space between lattice planes, h k l are the miller indices while α, β, γ are the diffraction angles.

The inter atomic spacing d was calculated from the Bragg's equation [11]:

$$2d\ sin\ \theta = n\lambda, \quad (2)$$

$$d = \frac{\lambda}{2sin\theta}. \quad (3)$$

Where n=1, λ=1.5406A^0

The average crystallite size of the film was calculated using Debye Scherer's formula [11] assuming spherical crystallite: Crystallite size =$\frac{K\lambda}{\beta Cos\theta}$, which can also be written as

$$D = \frac{0.9\lambda}{\beta cos\theta}. \quad (4)$$

Where β = full width at half maximum (FWHM), θ = diffraction angle, k = Shape factor and λ = wavelength of the X-rays (1.5406 Å) and D= grain size respectively.

Dislocation density δ was calculated using the equation [12]:

$$\delta = \frac{1}{D^2}. \quad (5)$$

Where D is the grain size of the film. The micro-strain ε was estimated using the equation [13]:

$$\varepsilon = \frac{\beta}{4tan\theta}. \quad (6)$$

Quantitative information about the preferential crystallite orientation of the SnS thin films was obtained from the texture coefficient (TC) which represents the preferential growth of certain planes compared to randomly oriented crystallites and was determined from the relation [14-15]:

$$TC = \frac{I/I_o}{(1/N)\Sigma_N(I/I_o)}. \quad (7)$$

Where: I is the measured intensity of the intense peak in the XRD spectrum, I_o is the intensity for completely random sample or the standard intensity of the hkl plane taken from the JCPDS 00-039-0354 card and N is the number of reflections considered in the analysis.

The morphology and the microstructure of the SnS thin film was characterized using High Resolution Scanning Electron Microscopy (HR-SEM, Zeiss) while the elemental composition of the films were determined by an Energy dispersive X-ray spectroscopy (EDS; Oxford instrument) attached to the SEM . The instrument was operated at a voltage of 20 kV while the images were captured at 5 kV. A Profilometry (VEECO DEKTAK 150) was used to carry out measurement of the thickness of the deposited films.

Electrical Characterisation

The carrier density, carrier mobility and carrier type were determined by an ECOPIA Hall Effect measurement system (HMS 3000 Hall measurement system) based on Van der pauw configuration. Two variable power supplies (KOOCU DC Power supply 1502DD with voltage variation of 0-15 V and ATX-650W, hp invent with voltage variation of 0-12 V) and two Multimeter (CHY VC 890C$^+$ digital Multimeter and DT9205ACE digital Multimeter) were also used to determine the electrical behaviour of the fabricated transistor. The temperature dependent resistance measurement of the deposited film was carried out in the temperature range of 283 to 523 K.

Evaluation of device performance of the fabricated EDL field effect thin film Transistor

The electrical behaviour of the SnS channel EDL field-effect transistors was evaluated by the plot of drain current (I_D) versus the drain-source bias which is called the output characteristics and the gate-source bias (V_{GS}) which is called transfer characteristics. To evaluate the device performances, electrical parameters such as field-effect mobility (μ_{FE}), cut off voltage, drain saturation current threshold voltage (V_{th}), transconductance and sub threshold swing (SS) were mainly considered as follows:

The x-axis value at the intercept of the transfer curve gives the value of Gate to source cut-off voltage ($V_{GS\ (OFF)}$) while the y-axis intercept gives the drain saturation current(I_{DSS}). The transconductance (g_m) which is simply the slope of the transfer characteristics was calculated using [1]:

$$g_m = \frac{\Delta I_D}{\Delta V_{GS}}. \tag{8}$$

The field effect mobility μ_{FE} was also obtained from the transconductance at low V_{DS} by:

$$\mu_{FE} = \frac{L g_m}{W C_i V_{DS}}. \tag{9}$$

Where C_i is the capacitance per unit area of the gate dielectric, w is the device width while L is the device length. The mobility is the average drift speed of carriers under the unit electric field.

The sub threshold swing (SS) which reflects the necessary V_G required to increase I_{DS} by an order of magnitude in the sub threshold region ($V_{GS} < V_{th}$) was determined as the inverse of maximum slope of the transfer curve given as:

$$SS = \left(\frac{d log(I_{DS})}{dV_{GS}}\right)^{-1} \tag{10}$$

RESULTS AND DISCUSSION

Compositional analysis of the annealed SnS thin film

The thickness of the SnS thin film was measured to be 0.40 μm thickness from the profilometry result. The main constituents' elements and their relative concentrations are given in table 1.The annealed SnS thin film was brown in colour, smooth, pin hole free and adheres firmly to the glass substrate surface. No significant colour change was noticed with annealing of the firm.

Table 1

SnS thin film elemental composition (atomic percent) at varied annealing Temperatures.

Annealing Temperature (℃)	Sn (at.%)	S (at.%)	Sn/S at %ratio	SnS (Total)
250	37.28	62.72	0.594	100

Fig. 2 gives the EDX spectrum of the SnS thin film deposited at annealing temperature of 250℃. From the figure, it is evident that the film contained Tin (Sn) and Sulpur (S) elements. However Na, Ca, Si, Cl and Ca elements were also observed which could be attributed to the glass substrates used. Similar observation was also made by [10,16]. The relative concentrations of Sn and S on the samples were evaluated as given in table 3.1 and by the EDS spectrum.

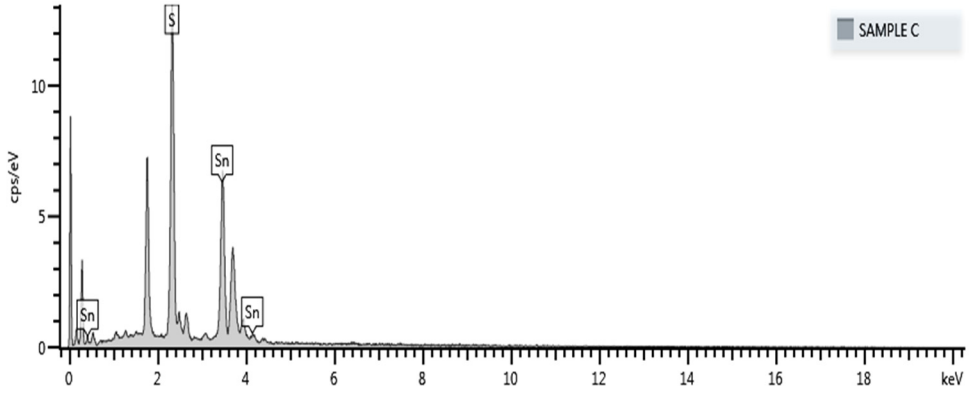

Fig. 2. EDS spectrum of the SnS thin film semiconductor channel layer

XRD Analysis

Fig. 3. shows the XRD pattern of SnS thin film annealed at 250 ℃ annealing temperature. The XRD spectra of SnS thin film annealed at annealing temperature of 250 ℃ is shown in fig 3 where the peaks which were identified using the JCPDS card number 39-0354 data are labelled with corresponding orientations using the miller indices. All reflections were indexed to orthorhombic SnS phase as compared with the standard JCPDS card. The X-ray diffractogram or

spectrum of the annealed film exhibited peaks of different orientations at 2Θ values of approximately 29.3°, 31.7°, 45.5° and 62.1° corresponding to (101), (040), (002) and (202) peaks. No impurities peaks of elemental sulphur, tin or other tin sulphide phases were identified in the XRD pattern of the annealed films which buttress the formation of pure SnS phase. The annealed SnS films were polycrystalline and showered an orthorhombic structure with calculated lattice parameters of a= 0.429 nm, b=1.123 nm and c=0.399 nm and an observed d spacing of 2.8194 (°A). The calculated texture coefficient values of the SnS semiconductor channel layer is given in Table 2.

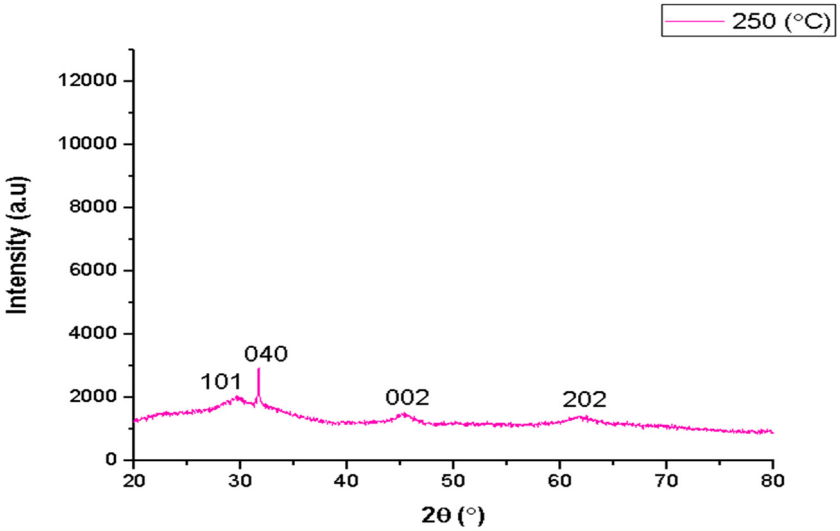

Fig. 3: XRD pattern of the SnS thin film semiconductor channel layer

Table 2.

Texture coefficient value for the SnS semiconductor channel laye

S/N	Annealing Temperature ℃	Texture coefficient (TC)				
		TC(101)	TC (040)	TC(002)	TC (202)	TC(080)
1	250	0.46	2.52	0.50	0.51	0

The value obtained shows that the TC value of (040) plane of annealed SnS semiconductor channel layer component are larger than 1 which reveals that the SnS thin film is polycrystalline with preferred orientation along the (040) plane denoting that the number of crystallite and grains along this plane is more than that on the other planes [14, 15, 17]. The peak associated with the (040) plane was used to calculate the crystallite size and other structural parameters been the preferred orientation of the annealed SnS thin film. The calculated average crystalline size, dislocation density and micro strain for the film is shown in Table 3.

Table 3.

Average crystalline size, dislocation density and micro strain for the SnS semiconductor channel layer

S/n	Annealing Temperature (℃)	Full width half maximum $\boldsymbol{\beta}$ (°)	2Θ (°)	Grain size D (nm)	Dislocation density $\boldsymbol{\delta \times 10^{14}}$ (Lines/$\boldsymbol{m^2}$)	Micro strain $\boldsymbol{\varepsilon \times 10^{-4}}$
1	250	0.12644	31.71153	65.30	2.35	5.31

The large average crystallite size obtained could also be attributed to the decrease in grain boundary and reduction in crystal system deformations which signifies increase in degree of perfection of grains with the removal of defects and healing of pores as a result of less number of grain boundaries, decrease in defects density and decrease in donor sites trapped at the dislocation and grain boundaries. Furthermore, crystallites ranges in size from small to large and crystallites as a result the smallest crystallite often possess the largest surface area to volume ratio such that given the higher surface area, they are more likely to be fragmented with annealing thereby enhancing crystal growth.

SEM analysis

The scanning electron microscopy results/micrograph at magnification of 20000 x for the semiconductor channel layer is shown in Fig. 4.

The average grain size of the SnS thin film semiconductor channel layer was calculated using imageJ software [18] and the histogram of the grain distribution is given in Figure 5. Otsu's thresholding method and particle analysis [19] was used after which statistical analysis of the data was made with histogram generated to study the grain distribution and

average grain size determined from the average particle size assuming round particles as confirmed by the analysis. The particle analyser was configured in a size range of 0 nm^2 to infinity in other to allow for coverage of smaller particles.

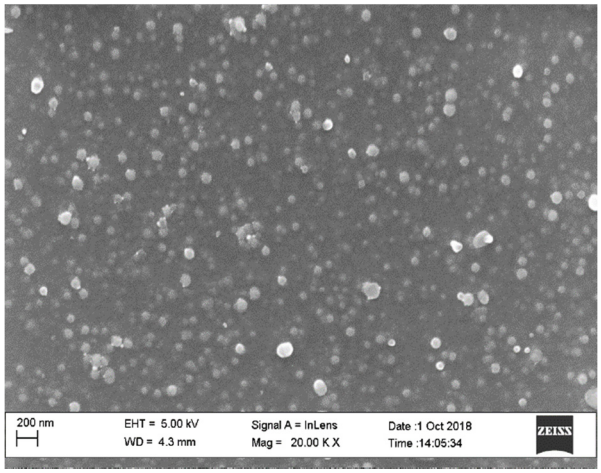

Fig. 4. SEM micrograph of the SnS semiconductor channel layer

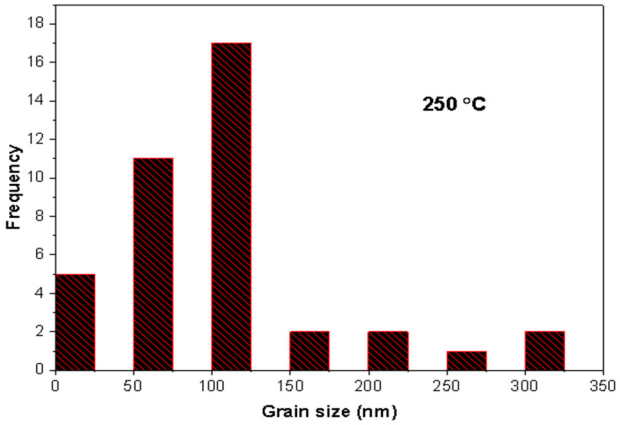

Fig. 5. Grain size histogram plot for SnS semiconductor channel layer annealed at 250 ℃ annealing temperature

The average grain size was found to be 137.53 nm. The histogram shows a non-uniform grain concentration and distribution at grain size range of 0.0 to 100 nm for the samples. The grain size distribution at 0.0 to 100 nm is larger than that of 100 to 350 nm range. There tends to be a preferred grain distribution and growth defining factor at 100 nm for all the samples which could be related to the preferred crystal orientation earlier defined by the XRD results. The increase in grain distribution from 0 to 100 nm range is followed by a decrease from 100 to 350 nm in all samples which could be attributed to initialisation of grain stability and uniformity at the range of 100 to 350 nm. The closely packed nature of the grains to each other reveals good adhesiveness of the deposited SnS thin film to the glass substrate. The larger grain sizes could enhance reduction in grain boundaries and potential barrier there by releasing charge carriers that were trap so as to further enhance carrier conductivity.

Temperature dependence of electrical conductivity

The temperature dependence of electrical conductivity of the deposited SnS thin film was studied by heating to a temperature of 300 ℃ after which the resistivity/conductivity was measured as the temperature reduced by 5 ℃ intervals. The obtained data was analysed using Arrhenius equation [20]. A plot of ln (σ/σ_0) versus (1/T) is given in Fig. 6.

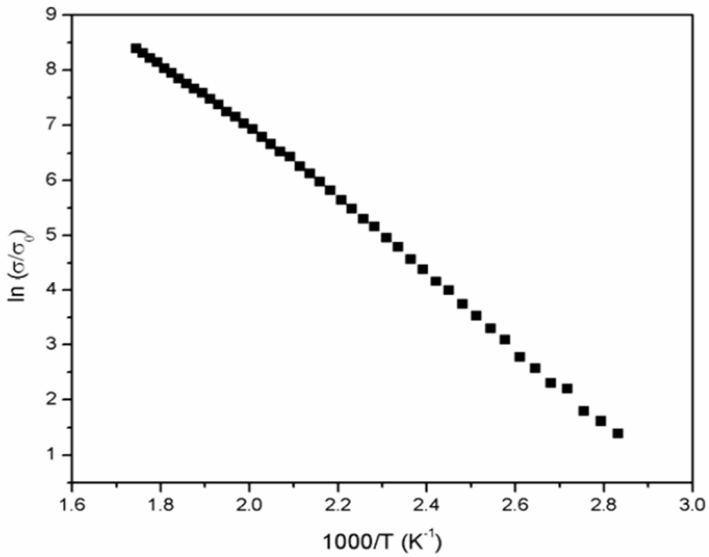

Fig. 6: The dependence of ln (σ/σ_0) versus (1000/T) for SnS thin film

The average activation energy of the charge carriers evaluated from the slope of the curve was obtained as 0.520 eV. The value of the activation energy could be attributed to the deep acceptor states stemming from the Sn Vacancy which plays significant role in p type carrier conductivity of the SnS semiconductor. The excess of Sulpur which is also evident in the elemental composition of the film, induces a proportionate Sn vacancy sites such that every anion would introduce

two positive type (p-type) conductor which is supported by the fact that the activation energy of the SnS thin film depends on elemental ratio, presence of crystal defect and the deposition method used. The SnS film conductance was observed to increase with temperature which indicates the semiconducting behaviour of the thin film. The excitation of charge carrier from valence band to conduction band could be responsible for the rise of conductivity [14].

Hall effect measurement for the SnS semiconductor channel layer

The measured electrical parameters of the SnS semiconductor channel layer from the Hall Effect measurement are given in Table 4.

Table 4.

Hall effect electrical parameters for the SnS semiconductor channel layer

Annealing Temperature (°C)	Bulk concentration N_b (cm^{-3})	Average Hall coefficient R_H (cm^3/c)	Carrier mobility μ (cm^2/Vs)	Resistivity $\boldsymbol{\rho}$ (Ωcm)	Conductivity $\boldsymbol{\sigma}$ $(\Omega cm)^{-1}$
250	3.167×10^{10}	1.971×10^{10}	1.619×10^{5}	1.025×10^{4}	9.756×10^{-5}

From Table 4, the average hall coefficient of the annealed SnS semiconductor channel layer is positive which indicates that the semiconductor channel layer is of p type carrier conduction with holes as majority carriers. Annealing increases carrier concentration, reduce resistivity due to improvement in crystallisation, greater grain size with annealing lead to decrease in defects density and crystal boundary which reduces resistivity hence increasing conductivity. This could be explained by the fact that annealing leads to improved crystallisation and increase in grain size in the films which could enhance the decrease of crystal defects and crystal bonding reduction, hence the release of trap electron and decrease resistivity [20].

The SnS EDLFET assembly

Fig. 7. shows a picture of the assembled SnS semiconductor channel layer Electric double layer field effect transistor with Honey gate dielectric. The measured gate capacitance of honey using LCR meter is 2.15 μF/ cm^2 while the dielectric constant is 20.50. Honey was used as a gel like electrolytic gate dielectric to generate an enhanced electric field response over SnS semiconductor channel layer. Due to the polarizability of honey, a diffusion of charge is formed at the thin layer between SnS semiconductor channel and honey. The thin layer forms an electric double layer which is a basic characteristics of ionic liguids contact with conductive materials and is as shown in Fig. 8.

A large charge gradient is formed on the surface of the SnS layer due to the nanoscale separation distance of the electric double layer. Application of positive gate voltage will cause the gate electrode to be positively charged such that when it is submerged in honey, anions accumulate at the gate/honey interface and cations at the honey/SnS interface. The electric double layer form at the honey/SnS interface alters the SnS semiconductor channel layer conductivity. Increase in positive V_{GS} will deplete the SnS channel of its free holes thereby turning it off.

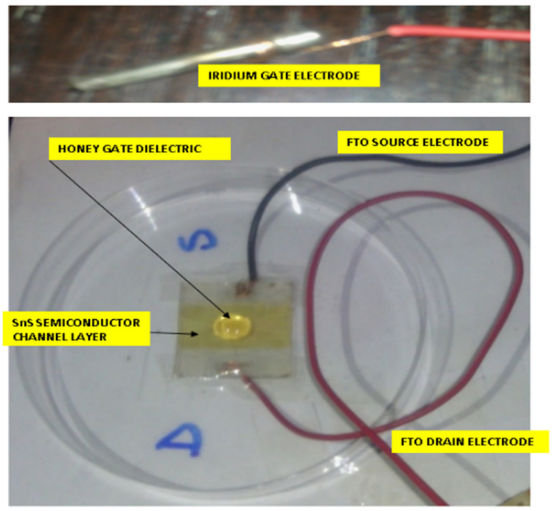

Fig. 7. SnS semiconductor channel layer Electric double layer field effect transistor with Honey gate dielectric

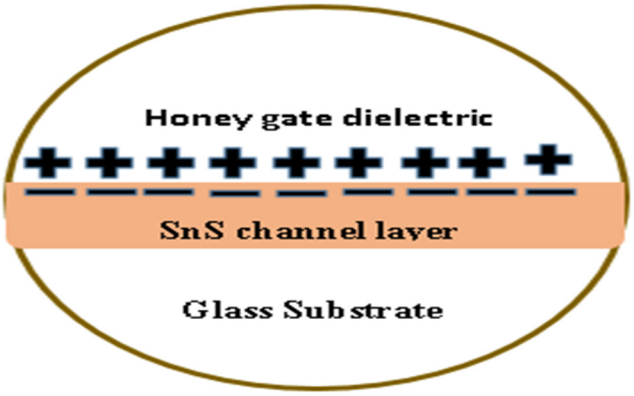

Fig. 8. Representation of charge distribution in honey/ SnS layer interface

Transfer and output characteristics of SnS EDLFET

Fig. 9. shows the transfer characteristics (Source drain current I_{DS} as a function of gate bias V_G) of the SnS EDLFET gated by honey dielectric at room temperature. While Fig. 10. Shows the output characteristics of the SnS honey gated EDLFET. The channel length for the device is 70 μm while the channel width is 4 mm.

At all values of the Vg used the gate current Ig≤ 10^{-3}Ids which signify that the fabricated device operates as a field effect transistor and specifically an electric double layer field effect transistor. From Figure 9, it is evident that the SnS EDLFET is a P channel device since the channel conductivity decreases with increasing positive gate bias. The I_{DS} increased with decreased in V_{GS} scanning which indicates a typical p-type transistor operation in the device. The device also operates in depletion mode, i.e. appreciable drain current flows at zero gate voltage as evident from the V_{GS}=0V drain current which is judged from the zero bias current in the transfer curve. The SnS EDLFET worked in a depletion mode with a normally "ON" state (i.e conducting without the application of gate bias voltage) which could be attributed to the maximum current flow from the source to drain when no difference in voltage exist between the gate and source electrodes.

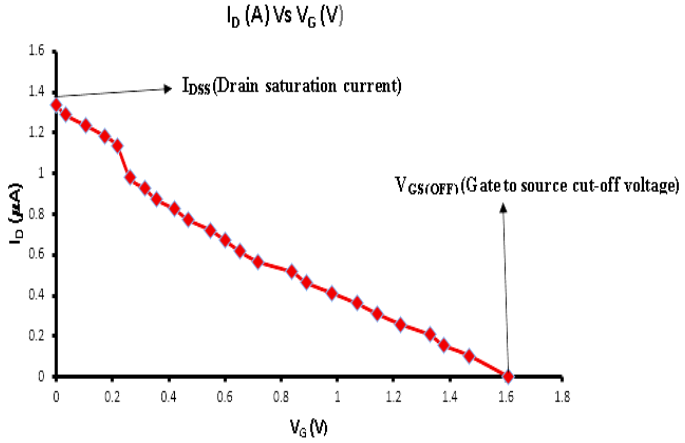

Fig. 9. Transfer curve of SnS honey gated EDLFET

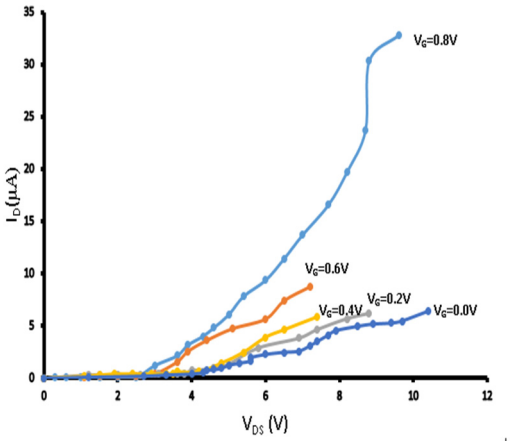

Fig. 10. Output curve of SnS honey gated EDLFET

The drain saturation current I_{DSS} as determined from the transfer curve at zero gate to source voltage (V_{GS}=0) and an applied drain to source constant voltage of 3V is 1.35 μA. This gives the maximum limiting current that can flow between the drain and source at V_{GS}=0. The drain current was observed to increase linearly then began to pinch off at the knee of the transfer curve at I_{DSS}. The I_{DSS} is temperature dependent with a negative temperature coefficient of approximately -0.5/°C. However with further application of gate voltage (positive V_{GS} than ($V_{GS\ (0ff)}$), the drain source channel could become more resistive by the changing size of the depletion region under the gate area such that the transistor is completely shuts off due to the depletion or shutting off of the majority charge carriers in the semiconductor channel.

From the transfer curve, the gate to source cut off voltage ($V_{GS\ (0ff)}$) was found to be 1.6 V which is the fundamental characteristics specifying the voltage necessary to turn the transistor device off. The gate to source voltage for a p channel device ranges from 0v for full conduction to several positive volts to turn it off. The 1.6V positive V_{GS} (less holes and less current) will deplete the SnS channel of its free holes thereby turning it "off". The low $V_{GS\ (0ff)}$ could enhance the choice off circuit design parameters. $V_{GS\ (0ff)}$ shifts with temperature and has a negative temperature coefficient of approximately -2mV/°C.

The transconductance which gives the amplifying factor of the transistor was obtained from the slope of the transfer characteristics as -809.61nA/V. The voltage required to increase the drain current by a factor of 10 which is also called sub-threshold slope (S) was estimated to be -1.6 $Vdec^{-1}$ from the curve of Log (I_D) versus V_{GS}. It could be attributed to the presence of small carrier traps in the SnS thin film which might not necessarily include the grain boundary and is suitable for the switching of devices in active matrix flat panel displays.

The field effect mobility obtained from the transconductance is 16.67 cm^2/v at low V_{DS}. The mobility value implies more carriers passing through the channel per unit time which is essential for a FET and has the advantage of enhancing higher screen luminance.

Fig. 10 shows the output characteristics (I_D-V_{DS}) of the SnS EDLFET transistor measured at gate voltage (V_G) of 0.2 to 0.8 V with a 0.2 v scan which also supports the field effect transistor operation. No appreciable hysteresis was observed in the output characteristics, indicating that the channel is stable once it is formed. The I_D curves are flat at low V_{DS} indicating that a condition of hard saturation is achieved due to complete pinch off of the channel. No clockwise hysteresis was observed which could be attributed to the non-availability or absence of continuous filling of traps by accumulated channel holes as V_{DS} is first increased from zero to a maximum of 0.8 V, then decrease back to 0 V. The fact that the I_D-V_{DS} characteristics curve do not show counter clockwise hysteresis indicates that ionic drift is not significant.

CONCLUSION

The Electric double layer field effect transistor was assembled using tin sulphide (SnS) thin film whose thickness and annealing temperature were earlier optimised as semiconductor channel layer and honey as gate dielectric. The semiconductor layer was deposited using Aerosol assisted chemical vapour deposition (AACV) and annealed in open air

at 250℃ on an etched region about the middle of a 4×4 mm FTO glass substrate with the source and drain electrode region defined by the etching and masking at the two ends of the substrate. Iridium was used the gate electrode while a copper wire was masked to the source and drain region to create contact. The thicknesses of the SnS layer was measured using profilometry, X-ray diffraction was used for phase and crystalline orientation, Scanning electron microscope was used to study the film morphology, the elemental composition of the film was determined by an Energy dispersive X-ray spectroscopy, Hall effect measurement and digital multimeters were a used to determine the SnS conductivity type, conductivity and the transistor characteristics. The SnS thin film was found to be polycrystalline consisting of Sn and S elements with define grains and of 0.4 μm thickness.

The SnS EDLT using honey as gate dielectric operated as p type channel in depletion mode with I_{DS} of 1.35 μA, $V_{GS\,(Off)}$ = 1.6 v, Trans conductance of -0.80961 μA/v, field effect mobility of 16.67 cm^2/v and sub-threshold slope of 1.6 $vdec^{-1}$ which are applicable as load resistors in synaptic transistor network, biosensor, logic gate circuits and in depletion load logic circuits. RF 9640, B15P are popular p channel depletion mode transistors in use.

Conclusively, very scanty reports have been made or exist on the study of SnS thin film applied to electronics as a semiconductor channel layer. SnS EDLFET using honey as gate dielectric offers an opportunity for further research and innovation into other materials that are unconventional in the expectation discovering new semiconductor and dielectric materials that are readily available and non-toxic. To the best of our knowledge and within the limit of available literature, no SnS based EDLFET has been reported hence making the results described here innovative to the scientific community.

Declaration of interest: none.

ACKNOWLEDGEMENTS

This research did not receive any specific grant from funding agencies in the public, commercial, or not-for-profit sectors, However, the authors acknowledged the Staff and management of Alex Ekwueme Federal University Ndufu Alike Ikwo, Ebonyi state, Federal University of Technology Minna, Sheda Science and Technology (SHESTCO), Namiroch research laboratory Abuja, iThemba Laboratory South Afica and the electron microscopy unit of the University of Western Cape, South Africa for their various contributions.

ORCID IDs

Thomas Daniel https://orcid.org/0000-0002-5176-9181, **Uno Uno** https://orcid.org/0000-0001-6693-5894,
Kasim Isah https://orcid.org/0000-0002-9670-7697, **Umaru Ahmadu** https://orcid.org/0000-0001-5966-0853

REFERENCES

[1] B.L. Theraja and A.K. Theraja, *A Textbook of Electrical Technology*. (S. Chand & company Limited, Ram Nagar New Delhi, 2007), pp.356-396.
[2] S.F. Akande and B.J. Kwaha, *Basic principles of Electronics*. (Jos University press, Plateau State, Nigeria, 2007), pp. 23-35.
[3] H. Du, Xi. Lin, Z. Xu and D. Chu, Springer. (2015), DOI: 10.1007/s10853-015-9121-y.
[4] K. Po-Jui, C. Sheng-Po and C. Shoou-Jinn, Electronic mater let. **10**, 89-94 (2014).
[5] H. Yuan, H. Liu and H. Shimotani, Nano let. **11**, 2601-2605 (2011).
[6] P. Thiruramanathan, G.S. Hikku, R. Krishna-Sharman and M. Siva Shakthi, J. ChemTech Res. **1**, 59-65(2015).
[7] S.S. Hedge, A.G. Kunjomana, K.A. Chandrasekharam, K. Ramesh and M. Prashantha, Physica B. **406**, 1143-1148 (2011).
[8] R.C. Ordonez, C.K. Hayashi, C.M. Torres, J.I. Melcher, K. Nackieb, G. Severa and D.Garmire, D, Scientific reports. **7**, 1-9 (2017).
[9] A. Sugaki, A. Kitakaze and H. Kitazawa, Sci. Rep. Tohoku Univ.16, 199(1985).
[10] T.H. Patel, TOSURSJ**. 4**, 6-13 (2012).
[11] B.J. Babu, A. Maldonado, S. Velumani and R. Asomoza, Mater.Sci. Eng B. **10**, 25-30(2010).
[12] I. Ilican, Y. Caglar and M. Caglar, J. Optoelectron. Adv. M. **10**, 2578-2583(2008).
[13] S.M. Ahmed, L.A. Latif and A.K. Salim, brsj. **37**, 1-6(2011).
[14] E. Guneri, F.Gode, C. Ulutas, F. Kirmizigul, G. Altindemir and C. Gumus, Chalcogenide Let. **7**, 685-694(2010).
[15] J. Lv, Z. Zhou, F. Wang, C. Liu, W. Gong, J. Dai, X. Chen, G. He, S. Shi, X. Song, Z. Sun and F. Liu, Superlattice Microst. **61**, 115-123 (2013).
[16] A. Gomez, H. Martinez, M. Calixto-Rodriguez, D. Avellaneda, P.G. Reyes and O. Flores, J.Mater.Sci. Eng. **33**(6), 352-358 (2013).
[17] M. Safonova, P.P.K. Nair, E. Mellikov, R. Aragon, K. Kerm, R. Naidu and O. Volobujeva, P. Est. Acad. Sci. **64**, 488-494 (2015).
[18] W.S. Rasband, (2014), in: http://imagej.nih.gov/ij/1997-2014.
[19] G. Julio, M.D. Merindano, M. Canals and M. Rallo, J. Anat. **212**, 879-886 (2008).
[20] T.S. Reddy and M.C. Kumar, RSC Adv. **6**, 95680-95692 (2016).

ЕЛЕКТРИЧНИЙ ДВОШАРОВИЙ ПОЛЬОВИЙ ТРАНЗИСТОР З ВИКОРИСТАННЯМ ТОНКОЇ SnS ПЛІВКИ В ЯКОСТІ НАПІВПРОВІДНИКОВОГО КАНАЛУ, А ТАКОЖ ДІЕЛЕКТРИЧНОГО ЗАТВОРУ З МЕДУ

Томас Даніель[1], Уно Уно[2], Касим Ісах[3], Умару Ахмаду[4]

[1]Кафедра Фізики/Геології/Геофізики, Alex Ekwueme федеральний університет Ndufu-Alike Ikwo, P.M.B 1010, штат Ebonyi, Нігерія

[1,2,3&4] Кафедра фізики федерального технологічного університету Мінна Мінна, P.M.B 065, штат Нігер, Нігерія

Дослідження було спрямоване на вивчення і застосування тонкої плівки SnS в якості напівпровідникового канального шару в збірці електричного двошарового польового транзистора, що має велике значення для успішної розробки нових концепцій

пристрою, застосувань і зміни фізичних властивостей матеріалів, оскільки описані на сьогодні EDLFET (електричний двошаровий польовий транзистор) і модуляція електронних станів були реалізовані на оксидах, нітриді, вуглецевих нанотрубках і органічних напівпровідниках, при цьому рідко згадувались халькогеніди. Мед використовувався в якості гелеподібного електролітичного діелектричного затвора для підвищення рівня генерування відгуку електричного поля через шар напівпровідникового каналу SnS завдяки його здатності забезпечувати роботу при високому струмі і низькій напрузі за рахунок формування іонного гелеподібного розчину, подібного іонним гелям, які містять іонні рідини. Електричний двошаровий польовий транзистор був зібраний з використанням тонкої плівки сульфіду олова (SnS) як шару напівпровідникового каналу, та меду як діелектрика. Виміряна за допомогою LCR-вимірювача ємність медового затвору склала 2,15 мкФ/см^2, тоді як діелектрична константа – 20,50. Напівпровідниковий шар наносили за допомогою хімічного осадження з парової фази за допомогою аерозолю і відпалювали на відкритому повітрі при 250° С у протравленій області приблизно на середині скляної підкладки 4×4 мм з FTO покриттям, при цьому область електрода на джерельному і стічному електроді обмежувалася травленням і маскуванням на обох кінцях підкладки. Іридій був використаний в якості електрода затвору, тоді як мідний дріт був замаскований у джерельній та стічній області для створення контакту з електродом. Для визначення характеристик пристрою були використані профілометри, рентгенівська дифракція, скануючий електронний мікроскоп, метод енергодисперсійної рентгенівської спектроскопії, вимір ефекту Холла та цифрові мультиметри. Було виявлено, що тонка плівка SnS є полікристалічною, такою, що складається з елементів Sn і S з дрібними зернами, з оптичним діапазоном 1,42 еВ і товщиною 0,4 мкм. Транзистор працював у режимі провідності каналу р-типу в режимі збіднення з мінливістю польового ефекту - 16,67 см^2/Vs, напругою відсікання - 1,6 V, струмом насичення стока - 1,35 μA, коефіцієнтом трансдуктівності – 809,61 nA/V та підпороговим значенням нахилу – 1,6 Vdec^{-1}, що можна порівняти зі стандартними технічними характеристиками в електроніці. Позитивне зміщення затвора призводить до зрушення напруги відключення через захоплення заряду на межі поділу канал/діелектрик.

КЛЮЧОВІ СЛОВА: тонка плівка SnS, польовий транзистор, мед, електричний подвійний шар, напівпровідник

ЭЛЕКТРИЧЕСКИЙ ДВУХСЛОЙНЫЙ ПОЛЕВОЙ ТРАНЗИСТОР С ИСПОЛЬЗОВАНИЕМ ТОНКОЙ SnS ПЛЕНКИ В КАЧЕСТВЕ ПОЛУПРОВОДНИКОВОГО КАНАЛА, А ТАКЖЕ ДИЭЛЕКТРИЧЕСКОГО ЗАТВОРА ИЗ МЕДА

1Кафедра Физики / Геологии / Геофизики, Alex Ekwuete федеральный университет Ndufu-Alike
Ikwo, P.M.B 1010, штат Ebonyi, Нигерия
[1,2,3 & 4] Кафедра физики федерального технологического университета Минна
Минна, P.M.B 065, штат Нигер, Нигерия

Исследование было направлено на изучение и применение тонкой пленки SnS в качестве полупроводникового канального слоя в сборке электрического двухслойного полевого транзистора, что имеет большое значение для успешной разработки новых концепций устройства, приложений и изменения физических свойств, поскольку описанные сегодня EDLFET (электрический двухслойный полевой транзистор) и модуляция электронных состояний были реализованы на оксидах, нитриде, углеродных нанотрубках и органических полупроводниках, при этом редко упоминались халькогениды. Мед использовался в качестве гелеобразного электролитического диэлектрического затвора для повышения уровня генерации отклика электрического поля через слой полупроводникового канала SnS благодаря его способности обеспечивать работу при высоком токе и низком напряжении за счет формирования ионного гелеобразного раствора, подобного ионным гелям, которые содержат ионные жидкости. Электрический двухслойный полевой транзистор был собран с использованием тонкой пленки сульфида олова (SnS) как слоя полупроводникового канала и меда как диэлектрика. Измеренная с помощью LCR-измерителя емкость медового затвора составила 2,15 мкФ/см^2, тогда как диэлектрическая постоянная – 20,50. Полупроводниковый слой наносили с помощью химического осаждения из паровой фазы с помощью аэрозоля и отжигали на открытом воздухе при 250 ° С в протравленой области примерно на середине стеклянной подложки 4 × 4 мм с FTO покрытием, при этом область электрода на исходном и стоковом электроде ограничивалась травлением и маскировкой на обоих концах подложки. Иридий был использован в качестве электрода затвора, тогда как медный провод был замаскирован в области стока и истока для создания контакта с электродом. Для определения характеристик устройства были использованы профилометры, рентгеновская дифракция, сканирующий электронный микроскоп, энергодисперсионная рентгеновская спектроскопия, измерение эффекта Холла и цифровые мультиметры. Было обнаружено, что тонкая пленка SnS является поликристаллической, состоящей из элементов Sn и S с мелкими зернами, с оптическим диапазоном 1,42 эВ и толщиной 0,4 мкм. Транзистор работал в режиме проводимости канала р-типа в режиме обеднения с изменчивостью полевого эффекта - 16,67 см^2/Vs, напряжением отсечения – 1,6 V, током насыщения стока – 1,35 μA, коэффициентом трансдуктивности – 809,61 nA/V и подпороговым значением наклона – 1,6 Vdec-1, что можно сравнить со стандартными техническими характеристиками в электронике. Положительное смещение затвора приводит к сдвигу напряжения отключения из-за захвата заряда на границе раздела канал/диэлектрик.

КЛЮЧЕВЫЕ СЛОВА: тонкая пленка SnS, полевой транзистор, мед, электрический двойной слой, полупроводник

East Eur. J. Phys. **3**. 81-82 (2019) DOI:10.26565/2312-4334-2019-3-10

PACS: 04.65.+e

SUPERGRAVITY WAS DISCOVERED BY D.V. VOLKOV AND V.A. SOROKA IN 1973, WASN'T IT?

Steven Duplij
Center for Information Technology (ZIV), Westfälische Wilhelms-Universität Münster, Münster, Germany
E-mail: douplii@uni-muenster.de

Supergravity is a remarkable theory combining supersymmetry and general relativity. While the theory has many developers from across the globe, we wish to address the question who were the real originators of this fantastic idea.
KEYWORDS: supergravity, supersymmetry, goldstonion, Higgs effect, Poincaré group, gauge field

The idea of supergravity (without mentioning this beautiful word) was given to the western public on December 5, 1972, in the last paragraph of the paper D.V. Volkov (47 y.o. that time, Dr. Habilitation, second degree after Ph.D. in European countries) and his PhD student V.P. Akulov (28 y.o. that time) "Possible universal neutrino interaction" ZhETF Pis. Red. (JETP Letters translated into English by AIP [1]) followed by the paper Physics Letters, September 3, 1973 "Is the neutrino a Goldstone particle?" [2]. It was clearly (for professionals) written: "...the gravitational interaction may be included by means of introduction the gauge fields for the Poincaré group. ...if the gauge field for the transformation (3) is also introduced, then as a result of the Higgs effect the massive gauge field with spin three-half appears and the considered Goldstone particle with spin one half disappears."

This program was realized as a concrete model in 1973 by D.V. Volkov and his PhD student V.A. Soroka (29 y.o. that time) in the paper "Higgs effect for Goldstone particles with spin 1/2" ZhETF Pis. Red. (JETP Letters translated into English by AIP [3]).

Therefore, October 20, 1973, is the day of true discovery of supergravity as a physical model (in a nonlinear realization). The later publications can be considered only as further development of the same idea, in either a different realization or in modern terminology, which is, in general, a matter of taste.

Indeed, such a model (among numerous ones suggested later on) appeared in 1976 and contained a new "magic" word "supergravity" which was absent in the above Volkov-Soroka paper: "Progress toward a theory of supergravity" Physical Review D [4] by D. Z. Freedman (33 y.o. in 1972, a postdoc working on Regge poles and scattering, that time), P. van Nieuwenhuizen (34 y.o. in 1972, a postdoc working on muon scattering, that time), and S. Ferrara (27 y.o. in 1972, PhD working on conformal invariance, that time). Because the F-N-F paper cites the Volkov-Soroka article [3], the F-N-F paper can be considered as "discovering" only a new word "supergravity". In the same month (June, 1976), it was published a paper "Consistent supergravity" Physics Letters B by S. Deser and B. Zumino [5], which cited the F-N-F article as a preprint and also V. Akulov, D.V. Volkov, and V.A. Soroka paper of 1975 "Gauge Fields on Superspaces with Different Holonomy Groups" [6] which contains the reference to Volkov-Soroka (1973) [3] as well.

The history of supergravity is given in the "SUSY story (narrated by its founders)" [7] and in the article "Supergravity" [8] in the "*Concise Encyclopedia of Supersymmetry*" by S. Duplij, J. Bagger, W. Siegel (Eds.) [9].

The connection between the V-S and F-N-F approaches was clearly explained several times, e.g.:

1) by D.V. Volkov in the above Encyclopedia "Supergravity before and after 1976. The story of goldstonions" or here [10] and in his talk "Supergravity before 1976" at the *International Conference on the History of Original Ideas and Basic Discoveries in Particle Physics,* Erice, 1994 [11];

2) by V.A. Soroka in "The Sources of Supergravity" in "*The Supersymmetric World. The Beginnings of the Theory*" G. Kane and M. Shifman (Eds.) [12] or [13] and "Starting-point of Supergravity" [14] presented at the Conference "Supergravity at 25", Stony Brook NY, 2001.

It is remarkable and a pity, that in the mass media articles about numerous prizes given for the "discovery of supergravity" contain not a single word about the true discoverers of supergravity in 1973: Dmitriy Vasilievich Volkov (1925-1996, Memorial page [15]) and Vyacheslav Alexandrovich Soroka (1944-2011, Memorial page [16]).

ORCID IDs

Steven Duplij https://orcid.org/0000-0003-1184-6952

REFERENCES

[1] D.V. Volkov, V.P. Akulov, Possible Universal Neutrino Interaction, JETP Letters, **16**(11), 621-624 (1972), in: http://www.jetpletters.ac.ru/ps/1766/article_26864.shtml.

[2] D.V. Volkov and V.P. Akulov, Is the neutrino a goldstone particle? Physics Letters B, **46**(1), 109-110 (1973), DOI: 10.1016/0370-2693(73)90490-5.

[3] D.V. Volkov, V.A. Soroka, Higgs effect for Goldstone particles with spin 1/2, ZhETF, **18**(8), 529-532 (1973), in: http://www.jetpletters.ac.ru/ps/1568/article_24038.shtml.

[4] D.Z. Freedman, P. van Nieuwenhuizen, and S. Ferrara, Progress toward a theory of supergravity, Phys. Rev. D, **13**, 3214-3218 (1976), DOI: 10.1103/PhysRevD.13.3214.

[5] S. Deser and B. Zumino, Consistent supergravity, Physics Letters B, **62**(3), 335-337 (1976).

[6] V. Akulov, D.V. Volkov, and V.A. Soroka, Gauge Fields on Superspaces with Different Holonomy Groups, JETP Letters, **22**(7), 187-188 (1975), DOI: 10.1007/BFb0105272, in: http://www.jetpletters.ac.ru/ps/1526/article_23351.shtml.

[7] E. Likhtman, D. Volkov, V. Akulov, H. Miyazawa, G. Stavraki, V. Kac, V. Pakhomov, J. Lopuszanski, R. Haag, D. Leites, SUSY Story (narrated by its founders), in: S. Duplij, W. Siegel, J. Bagger, editors, *Concise Encyclopedia Of Supersymmetry and Noncommutative Structures in Mathematics and Physics,* (Springer, Berlin, New York, 2005), in: https://ivv5hpp.uni-muenster.de/u/douplii/susy/SUSYEnc_Story.pdf.

[8] S. Duplij, W. Siegel, J. Bagger, editors, *Concise Encyclopedia of Supersymmetry and Noncommutative Structures in Mathematics and Physics* (Springer, Berlin, New York, 2005), in: https://www.springer.com/gp/book/9781402013386.

[9] S. Duplij, Supergravity, in: [6] https://www.researchgate.net/publication/304156971_Supergravity.

[10] D.V. Volkov, Supergravity Before and After 1976, (1994), in: https://arxiv.org/abs/hep-th/9404153.

[11] D.V. Volkov, Supergravity Before 1976, in: https://arxiv.org/abs/hep-th/9410024.

[12] V.A. Soroka, The Sources of Supergravity, in: G. Kane and M. Shifman, editors, *The Supersymmetric World. The Beginnings of the Theory*, (2000), pp.88-92, DOI: 10.1142/9789812385505_0011.

[13] V.A. Soroka, The Sources of Supergravity, (2002), in: https://arxiv.org/abs/hep-th/0203171.

[14] V.A. Soroka, Starting-point of Supergravity, (2001), presented at the Conference *Supergravity at 25*, (Stony Brook, NY, 2001), in: https://arxiv.org/abs/hep-th/0111271.

[15] D.V. Volkov, Memorial page, in: https://ivv5hpp.uni-muenster.de/u/douplii/volkov.

[16] V.A. Soroka, Memorial page, in: https://ivv5hpp.uni-muenster.de/u/douplii/soroka.

СУПЕРГРАВІТАЦІЯ БУЛА ВІДКРИТА Д.В. ВОЛКОВИМ ТА В.А. СОРОКОЮ У 1973 РОЦІ, ЧИ НЕ ТАК?

Степан Дуплій

Центр інформаційних технологій, Вестфальський університет Вільгельма, Мюнстер, Німеччина

Супергравітація – чудова теорія, яка об'єднує суперсиметрію і загальну теорію відносності. Хоча цією теорією займалося багато вчених у всьому світі, ми намагаємося з'ясувати, хто в реальності відкрив цю фантастичну ідею.

КЛЮЧОВІ СЛОВА: супергравітація, суперсиметрія, голдстоніан, ефект Хіггса, група Пуанкаре, калібрувальне поле

СУПЕРГРАВИТАЦИЯ БЫЛА ОТКРЫТА Д.В. ВОЛКОВЫМ И В.А. СОРОКОЙ В 1973 ГОДУ, НЕ ТАК ЛИ?

Степан Дуплий

Центр информационных технологий, Вестфальский университет Вильгельма, Мюнстер, Германия

Супергравитация – замечательная теория, объединяющая суперсимметрию и общую теорию относительности. Хотя этой теорией занимались многие ученые во всем мире, мы пытаемся выяснить, кто в реальности открыл эту фантастическую идею.

КЛЮЧЕВЫЕ СЛОВА: супергравитация, суперсимметрия, голдстониан, эффект Хиггса, группа Пуанкаре, калибровочное поле

PACS: here you must specify PACS codes

INSTRUCTIONS FOR PREPARING MANUSCRIPT IN EAST EUROPEAN JOURNAL OF PHYSICS

[1]N.N. Author, [2]N.N. Co-author(s)
[1] Affiliation of first author
[2] Affiliation of second author (if different from first Authors)
[1] E-mail: corresponding_authors@mail.com, [1]ORCID ID
[2]E-mail: next_authors@mail.com, [2]ORCID ID
Received January 4, 2019

Each paper must begin with an abstract. The abstract should be typed in the same manner as the body text (see below). Please note that these Instructions are typed just like the manuscripts should be. The abstract must have at least 1800 phonetic symbols, supplying general information about the achievements, and objectives of the paper, experimental technique, methods applied, significant results and conclusions. Page layout: the text should be printed on the paper A4 format, at least 5 pages, with margins of: Top - 3, Bottom, Left and Right - 2 cm. The abstract should be presented in English (only for foreign authors), Ukraine and Russian.
KEYWORDS: there, must, be, at least, 5 keywords

This is introduction section. This paper contains instructions for preparing the manuscripts. The text should be prepared in .doc format (using MS Word).

INSTRUCTIONS

The text should be typed as follows:
• title: Times New Roman, 12 pt, ALL CAPS, bold, 1 spacing, centred;
• authors: name, initials and family names; Times New Roman, 12 pt, bold, 1 spacing, centred;
• affiliation(s): Times New Roman, 9 pt, italic, 1 spacing, centred;
• abstract: Times New Roman, 9 pt, 1 spacing, justified;
• body text: Times New Roman, 10 pt, 1 spacing, justified; paragraphs in sections should be indented right (tabulated) for 0.75 cm;
• section titles: Times New Roman, 10 pt, bold, 1 spacing, centred, without numbering, one line should be left, blank above section title;
• subsection titles: Times New Roman, 10 pt, bold, 1 spacing, centred, without numbering in accordance to the section (see below), one line should be left blank above subsection title;
• figure captions: width of the figure should be 85 or 170 mm, figures should be numbered (Fig. 1) and titled below figures using sentence format, Times New Roman, 9 pt, 1 spacing, centred (if one line) or justified (if more than one line); one line should be left blank below figure captions;
• table captions: width of the table should be 85 or 170 mm, tables should be numbered (Table 1.) and titled above tables using sentence format, Times New Roman, 10 pt, 1 spacing, centred (if one line) or justified (if more than one line), tables should be formatted with a single-line box around the outside border and single ruling lines between rows and columns; one line should be left blank below tables;
• equations: place equations centred, numbered in Arabic (1), flush right, equations should be specially prepared in MathType; one line should be left blank below and above equation.

Additional instructions

Numerated figures and tables should be embedded in your text and placed after they are cited. Only black and white drawings and sharp photographs are acceptable. Letters in the figures should be 3 mm high. The figures should be presented in one of the following graphic formats: jpg, gif, pcx, bmp, tif.

REFERENCES

Cite references in AIP style (https://guides.lib.monash.edu/citing-referencing/aip). Numbering in the order of referring in the text, e.g. [1], [2-5], etc. References should be listed in numerical order of citation in the text at the end of the paper (justified), Times New Roman, 9 pt, 1 spacing.

Journal Articles
[1] T. Mikolajick, C. Dehm, W. Hartner, I. Kasko, M. J. Kastner, N. Nagel, M. Moert, and C. Mazure, Microelectron. Reliab. **41**, 947 (2001).
[2] S. Bushkova, B.K. Ostafiychuk and O.V. Copaiev, Physics and Chemistry of Solid State. **15**(1), 182-185 (2014). (in Ukrainian)
[3] M. Yoshimura, E. Nakai, K. Tomioka, and T. Fukui, Appl. Phys. Lett. **103**, 243111 (2013), doi: 10.7567/APEX.6.052301.

E-print resourses with collaboration research
[4] Aaboud et al. (ATLAS Collaboration), Eur. Phys. J. C, **77**, 531 (2017).
[5] OR: M. Aaboud et al. (ATLAS Collaboration), Eur. Phys. J. C, **77**, 531 (2017), doi: 10.1140/epjc/s10052-017-5061-9
[6] Sjöstrand et al., *Comput. Phys. Commun.* **191,** 159-177 (2015), e-print arXiv:1410.3012.
[7] Amin et al. e-print arXiv:1006.3075 (2010).
[8] Boudreau, C. Escobar, J. Mueller, K. Sapp, and J. Su, (2013), e-print arXiv:1304.5639.

Books
[9] S. Inoue and K.R. Spring, *Video Microscopy*: *The fundamentals*, 2nd ed. (Plenum, New York, 1997), pp. 19-24.
[10] I. Gonsky, T.P. Maksymchuk and M.I. Kalinsky, *Біохімія Людини [Biochemistry of Man],* (Ukrmedknyga, Ternopil, 2002), p. 16. (in Ukrainian)
[11] V.V. Mal'tsev, *Металлография промышленных цветных металлов и сплавов [Metallography of industrial nonferrous metals and alloys],* (Moscow, Metallurgiya, 1970), p. 364. (in Russian)
[12] M. Garkusha, *Основи Фізики Напівпровідників [Fundamentals of Semiconductor Physics]* (Vysshaja shkola, Moscow, 1982), in: http://gagago.ru/g20-osnovi-fiziki-napivprovidnikiv-pidruchnik-dlya-tehniku.html.

Book Chapters
[13] M. Gonzalez-Leal, P. Krecmer, J. Prokop and S.R. Elliot, in: *Photo-Induced Metastability in Amorphous Semiconductors*, edited by A.V. Kolobov (Wiley-VCH, Weinheim, 2003), pp. 338-340.
[14] A. Kochelap and S.I. Pekar, in: *Теория Спонтанной и Стимулированной Хемилюминесценции Газов [Theory of Spontaneous and Stimulated Gas Chemiluminescence]* (Naukova dumka, Kyiv, 1986), pp. 16-29. (in Russian)

Conference or symposium proceedings
[15] C. Yaakov and R.Huque, in: *Second International Telecommunications Energy Symposium Proceedings*, edited by E. Yow (IEEE, New York, 1996), pp. 17-27.
[16] V. Nikolsky, A.K. Sandler and M.S. Stetsenko, in: *Автоматика-2004: Матеріали 11 Міжнародної Конференції по Автоматичному Управлінню [Automation-2004: Materials of the 11th International Conference on Automated Management]* (NUHT, Kyiv, 2004), pp. 46-48. (in Ukrainian)

Patent
[17] I.M. Vikulin, V.I. Irha and M.I. Panfilov, Patent Ukraine No. 26020 (27 August 2007). (in Ukrainian)

Special Notes
1. Use International System of Units (SI system). 2. It is undesirable to use acronyms in the titles. Please define the acronym on its first use in the paper.
3. Refer to isotopes as ^{14}C, ^{3}H, ^{60}Co, etc.

Наукове видання

СХІДНО-ЄВРОПЕЙСЬКИЙ ФІЗИЧНИЙ ЖУРНАЛ

Номер 3, 2019

EAST EUROPEAN JOURNAL OF PHYSICS

No 3, 2019

Збірник наукових праць
англійською, українською, російською мовами

Коректор – Коваленко Т.О.
Технічний редактор – Гірник С.А.
Комп'ютерне верстання – Гірник С.А.

Підписано до друку 30.09.2019. Формат 60×84/8. Папір офсетний.
Друк ризографічний.
Ум. друк. арк. 12,6. Обл.-вид. арк. 12,9
Тираж 65 пр. Зам. № Ціна договірна

61022, Харків, майдан Свободи, 4
Харківський національний університет імені В.Н. Каразіна
Видавництво

Надруковано Харківський національний університет імені В.Н. Каразіна
61022, Харків, майдан Свободи, 4, тел. +380-057-705-24-32
Свідоцтво суб'єкта видавничої справи ДК № 3367 від 13.01.09